UNIVERSITY OF CALIFORNIA

Santa Barbara

Integrated Si_3N_4 Waveguide Circuits for Single- and Multi-Layer Applications

A dissertation submitted in partial satisfaction of the

requirements for the degree Doctor of Philosophy

in Electrical and Computer Engineering

by

Taran Arthur Huffman

Committee in charge:

Professor Daniel J. Blumenthal, Chair

Professor John E. Bowers

Professor Nadir Dagli

Dr. Douglas Baney

December 2018

The dissertation of Taran Arthur Huffman is approved.

_____

John E. Bowers

_____

Nadir Dagli

_____

Douglas Baney

_____

Daniel J. Blumenthal, Committee Chair

November 2018

Integrated SI_3N_4 Waveguide Circuits for Single- and Multi-Layer Applications

by

Taran Arthur Huffman

ACKNOWLEDGEMENTS

To my friends and family. To my love, Chelsea.

VITA OF TARAN ARTHUR HUFFMAN
November 2018

EDUCATION

Bachelor of Science in Physics, University of California, Santa Barbara, May 2012
Master of Science in Electrical and Computer Engineering, Photonics, University of California, Santa Barbara, May 2012
Doctor of Philosophy in Electrical and Computer Engineering, University of California, Santa Barbara, May 2018 (expected)

PROFESSIONAL ACTIVITIES

2012-2014: Founding Treasurer, IEEE Photonics Society, UCSB Student Branch Chapter, University of California, Santa Barbara
2014-2016: Vice-President, IEEE Photonics Society, UCSB Student Branch Chapter, University of California, Santa Barbara

PUBLICATIONS

Belt, Michael, Taran Huffman, Michael L. Davenport, Wenzao Li, Jonathon S. Barton, and Daniel J. Blumenthal. "Arrayed narrow linewidth erbium-doped waveguide-distributed feedback lasers on an ultra-low-loss silicon-nitride platform." *Optics letters* 38, no. 22 (2013): 4825-4828.

Moreira, Renan, Jonathon Barton, Michael Belt, Taran Huffman, and Daniel Blumenthal. "Optical interconnect for 3D integration of ultra-low loss planar lightwave circuits." In *Integrated Photonics Research, Silicon and Nanophotonics*, pp. IT2A-4. Optical Society of America, 2013.

Gundavarapu, Sarat, Taran Huffman, Michael Belt, Renan Moreira, John Bowers, and Daniel Blumenthal. "Integrated ultra-low-loss silicon nitride waveguide coil for optical gyroscopes." In *Optical Fiber Communication Conference*, pp. W4E-5. Optical Society of America, 2016.

Huffman, Taran, Michael Davenport, Michael Belt, John E. Bowers, and Daniel J. Blumenthal. "Ultra-low loss large area waveguide coils for integrated optical gyroscopes." *IEEE Photonics Technology Letters* 29, no. 2 (2016): 185-188.

Huffman, Taran, Michael Davenport, Michael Belt, John E. Bowers, and Daniel J. Blumenthal. "Ultra-low loss stitching for large-area waveguide based delay-line gyroscopes." In *Photonics Conference (IPC), 2016 IEEE*, pp. 478-479. IEEE, 2016.

Gundavarapu, Sarat, Michael Belt, Taran Huffman, Minh A. Tran, Tin Komljenovic, John E. Bowers, and Daniel J. Blumenthal. "Integrated Sagnac optical gyroscope sensor using ultra-low loss high aspect ratio silicon nitride waveguide coil." In *Optical Fiber Sensors Conference (OFS), 2017 25th*, pp. 1-4. IEEE, 2017.

Huffman, Taran Arthur, Grant M. Brodnik, Cátia Pinho, Sarat Gundavarapu, Douglas Baney, and Daniel J. Blumenthal. "Integrated Resonators in an Ultralow Loss Si 3 N 4/SiO 2 Platform for Multifunction Applications." *IEEE Journal of Selected Topics in Quantum Electronics* 24, no. 4 (2018): 1-9.

ABSTRACT

Integrated SI_3N_4 Waveguide Circuits for Single and Multi-Layer Applications

by

Taran Arthur Huffman

Photonic integrated circuits are key building blocks for an ever-increasing range of applications, including optical communications, sensing, and position and navigation. A key challenge to today's photonics integration is realizing circuits and functions that require low-loss waveguides on chip while balancing waveguide loss with device performance and footprint. The Si_3N_4 waveguide low-loss platform serves as a third platform that complements silicon photonics and III/V semiconductor-based photonics. Incorporating the low loss attributes of Si_3N_4 waveguides into a photonic circuit to realize varying functions requires tuning the properties of the waveguide through parameters like waveguide core geometry and upper cladding design. In this dissertation, the design, fabrication, and optimization of these waveguides and their applications are described, and several devices are demonstrated. The first device is a high-extinction tunable third-order resonator filter with record extinction ratio demonstrating an application that employs waveguide geometry for compact and higher FSR (free spectral range) devices. Next, delays and resonators for application to rotational sensing using low-loss, large-area designs are demonstrated. Lastly, a method for vertically

integrating multiple waveguide layers, capable of integrating devices with different loss and footprint requirements, is demonstrated in the form of a multi-layer delay spiral.

TABLE OF CONTENTS

LIST OF FIGURES

Chapter 1

Introduction

Optical fibers span the globe, creating a near-literal web that forms the infrastructure of the Internet. At either end of a fiber, the transmitter and receiver of a photonic link, one will find a microchip with numerous optical components, such as lasers, modulators, and photodetectors. Such a microchip is a photonic integrated circuit (PIC). Waveguides connecting these components are the planar on-chip analogue to fibers. Planar waveguides are used to direct and manipulate light on a PIC. Optical fibers have been an incredible success because of their impressively low losses, losing less than a dB of energy over a kilometer. The development of waveguides with similar loss characteristics enables the integration of chip-scale photonic devices that allows for new functionality.

The ever-increasing demand for communication bandwidth has led to continual investment and development in PICs [1]. Although communication has been one of the primary driving forces for PIC development, their application extends far beyond communications to many other fields, such as sensing [2] or medicine [3]. Photonics even stands to uproot electrical components within high-speed computers and datacenters [4].

Many applications benefit from the ability to create long optical path lengths, frequently called time-delays, and are critically dependent upon the waveguide propagation loss. These time-delays are an integral part of many PICs such as RF filters [5] and, to use an example salient to this dissertation, optical gyroscopes [6]. Optical resonators, in the form of a

waveguide ring coupled to a bus, have similarly numerous applications, such as microwave photonics [7] or non-linear optics [8].

1.1 Waveguides within Various Photonic Platforms

Table 1 provides a summary of widely used photonic integration platforms. It should be noted that this list is not exhaustive, and even within the platforms there are designs with performances that are not included. Indium phosphide (InP) is a mature integration platform based on a direct bandgap material to produce devices with very efficient detection, modulation, and emission of light. These qualities make InP ineffective for low-loss waveguide structures. In contrast to the InP platform are the silicon- and silica-based waveguide platforms, which have indirect bandgaps and can achieve impressive waveguide performance but cannot be used to effectively produce or detect light.

Table 1. Summary of widely used photonic platforms.

Platform	Advantages	Disadvantages
Si_3N_4 Waveguides [9][10]	-Low propagation (<1 to 10dB/m) and coupling loss -Highly birefringent -CMOS compatible	-Large bend radii of 10mm -No direct active components -Highly birefringent
Doped Silica Waveguides [11]	-Low propagation loss (3-7dB/m)	-Large bend radius >5mm -No active components
Silicon Waveguides [12]	-CMOS compatible -Low bend radius (5μm)	-High propagation losses, 10s of dB/m -No direct active components
InP Waveguides [13]	-Small footprint devices -Mature active components -Strong electro-optic effect	-High material cost -Very high propagation losses, greater than 50dB/m

The ultra-low-loss Si_3N_4 photonic integration platform, shown in Table 1, has been used to demonstrate record-low losses of less than 0.1dB/m [9] and is explored in this dissertation. These low-loss waveguides are based on high-aspect-ratio waveguides with cores that are very thin and wide and also have large bend radii of ~10mm. However, these waveguides can be flexible in their design. Thicker, lower aspect-ratio waveguides can have tighter bend radii in exchange for higher propagation losses. This variability allows the platform to address a very wide range of applications.

The Si_3N_4 waveguide platform has advantages beyond low-loss propagation. Active components are key to many of the examples given and many of the devices within this dissertation. Multiple methods of integrating active components have been demonstrated. Gain sections and lasers have been fabricated by including an erbium-doped layer [14]. In addition, transitions to a silicon waveguide layer and to InP actives with both optical sources and detectors have been achieved [15][16]. The Si_3N_4 waveguide process is compatible with CMOS processing (complementary metal–oxide–semiconductor), allowing for mass production using the same infrastructure as the expansive electronics industry. Finally, demonstrated within this dissertation, these waveguides can be vertically stacked atop one another without significant performance impact. This capability enables more complex routing, combinations of different waveguide properties, and higher-density structures.

1.2 This Work

This dissertation includes reports on the properties and design of waveguides on the Si_3N_4 waveguide platform. Later, specific devices fabricated within this platform are reported in detail. Finally, a method for vertically stacking these waveguide layers is presented.

Comparisons between different waveguide platforms are presented in Chapter 1. Although it is exceedingly difficult to make direct comparisons between the performances of many of these platforms due to the shifting needs of a given PIC, the Si_3N_4 ultra-low-loss waveguide system was established as having a uniquely large array of applications due to its impressively low loss, CMOS fabrication compatibility, and wide array of previously demonstrated active integration components.

In Chapter 2, the Si_3N_4 ULLW platform fabrication, design, and performance are discussed in detail. In particular, the various loss sources in this system and how they vary with the waveguide design are examined. Trends are outlined that will be utilized when designing the waveguides implemented in this dissertation for specific applications in many of the other chapters. A detailed fabrication section is included and will be referred to in each device chapter. Lastly, the primary method of measuring and evaluating low-loss waveguide performance, using optical backscatter reflectometry, is discussed.

In Chapter 3, ring resonator performance is mathematically described. Methods for controlling different resonator properties are discussed in relation to the waveguide design. Single-bus resonators designed to maximize the Q and power enhancement within the resonator are focused upon, as well as third-order ring resonators optimized as filters, as these are the devices demonstrated in the following chapters.

The various waveguide thicknesses used for the devices throughout this dissertation are illustrated in Fig. 1. At a given core thickness, the waveguide width is selected to be as large as possible while still maintaining single-mode operation. The loss, critical bend radius, Q_i, and finesse in this figure are based on these single-mode geometries. The meaning of these parameters and how they are derived is explained in detail in the second and third chapters.

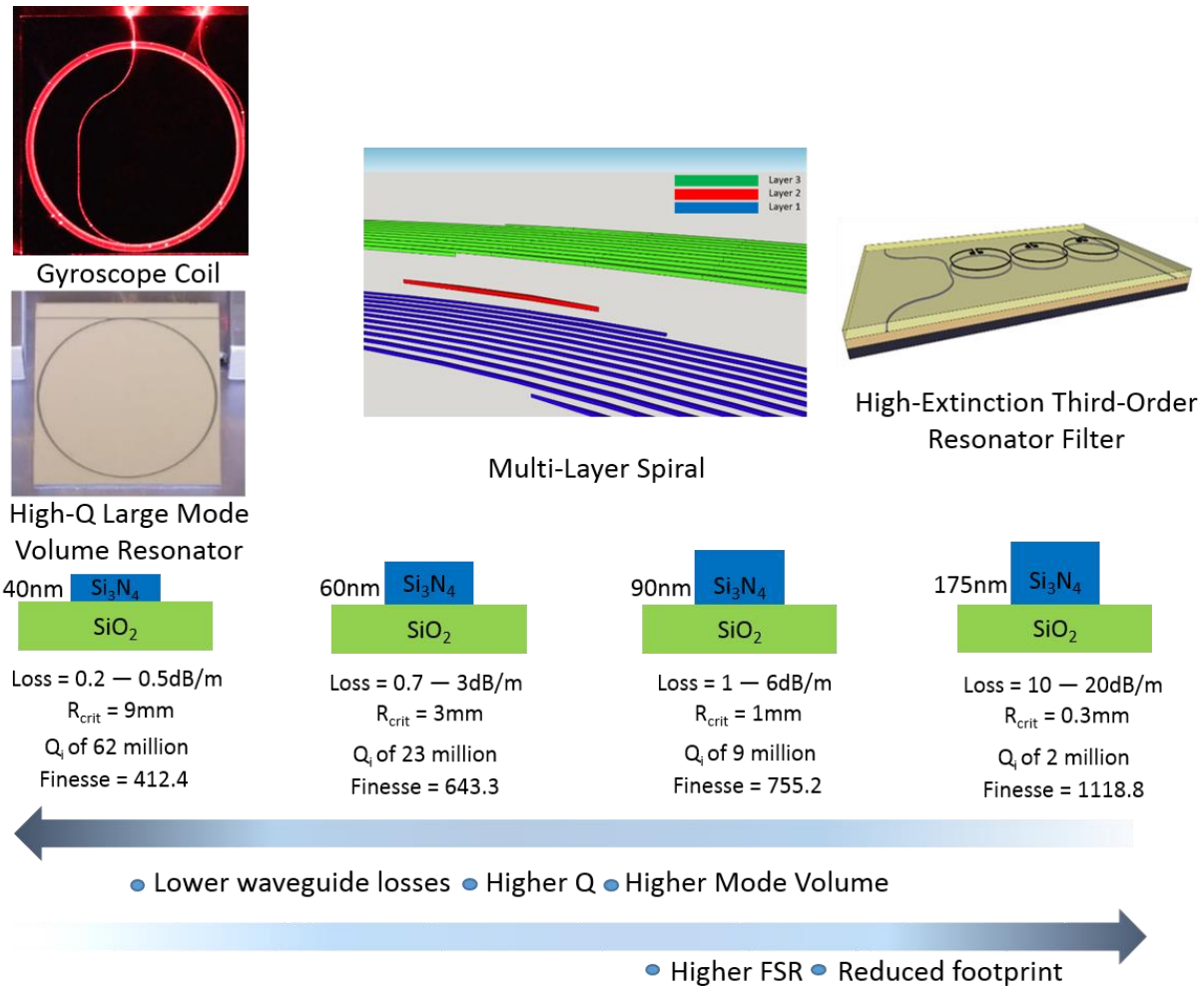

Fig. 1. Summary of waveguide properties based on core thickness and the corresponding devices based on those waveguides in this dissertation.

An ultra-high extinction ratio third-order resonator filter, shown at the far right of Fig. 1, is examined in Chapter 4. This record measured 80dB wavelength filter, fully tunable over its 50GHz free spectral range, utilizes a thick waveguide core to access tighter bend radii and attain a larger free spectral range. In Chapter 5, the design and fabrication of ultra-high-Q large mode volume resonators, with Q_is exceeding 60 million and that are optimized for Brillouin lasing—shown at the far left of Fig. 1—are discussed. The performance of these resonators as a Brillouin laser is beyond the scope of this dissertation and can be found in [17]. Although both designs utilize ring resonators, they emphasize very different aspects of their

design and the possible performance of the Si_3N_4 waveguide. In Chapter 6, the design of integrated delay-based gyroscopes is examined, demonstrated, for the first time, with a 10-meter waveguide coil and sensitivity classified as a tactical gyroscope, shown on the left side of Fig. 1. In Chapter 7, the techniques for vertically stacking multiple waveguides are explored, shown in the center of Fig. 1. These multiple layers maintain low-loss propagation, are optically isolated, and are able to couple efficiently to each other. The dissertation is summarized in Chapter 8, and future directions of research are explored.

1.3 References

[1] Cisco Visual Networking. “Forecast and Methodology, 2012-2017.” White Paper (2013).

[2] Pozo, J.; Harmsma, P.; Lo Cascio, D.M.R., “Application specific photonic integrated circuits and the sensing industry,” in Transparent Optical Networks (ICTON), 2013 15th International Conference on, vol., no., pp.1-1, 23-27 June 2013.

[3] Günay Yurtsever, Boris Považay, Aneesh Alex, Behrooz Zabihian, Wolfgang Drexler, and Roel Baets, “Photonic integrated Mach-Zehnder interferometer with an on-chip reference arm for optical coherence tomography,” Biomed. Opt. Express 5, 1050-1061 (2014).

[4] D. Vantrease, R. Schreiber, M. Monchiero, M. McLaren, N. Jouppi, M. Fiorentino, A. Davis, N. Binkert, R. Beausoleil, and J. Ahn, “Corona: System Implications of Emerging Nanophotonic Technology,” in *35th International Symposium on Computer Architecture*, Beijing, China, pp. 153164, June 2008.

[5] Xie, Yiwei, Zihan Geng, Leimeng Zhuang, Maurizio Burla, Caterina Taddei, Marcel Hoekman, Arne Leinse, Chris GH Roeloffzen, Klaus-J. Boller, and Arthur J. Lowery. “Programmable optical processor chips: toward photonic RF filters with DSP-level flexibility and MHz-band selectivity.” *Nanophotonics* 7, no. 2 (2017): 421-454.

[6] Lefevre, Herve C. *The fiber-optic gyroscope*. Artech house, 2014.

[7] Ilchenko, Vladimir S., and Andrey B. Matsko. “Optical resonators with whispering-gallery modes-part II: applications.” *IEEE Journal of selected topics in quantum electronics* 12.1 (2006): 15-32.

[8] Xuan, Yi, Yang Liu, Leo T. Varghese, Andrew J. Metcalf, Xiaoxiao Xue, Pei-Hsun Wang, Kyunghun Han et al. “High-Q silicon nitride microresonators exhibiting low-power frequency comb initiation.” *Optica* 3, no. 11 (2016): 1171-1180.

[9] Bauters, Jared F., Martijn JR Heck, Demis D. John, Jonathon S. Barton, Christiaan M. Bruinink, Arne Leinse, René G. Heideman, Daniel J. Blumenthal, and John E. Bowers. “Planar waveguides with less than 0.1 dB/m propagation loss fabricated with wafer bonding.” Optics Express 19, no. 24 (2011): 24090-24101.

[10] Bauters, Jared F., Martijn JR Heck, Demis John, Daoxin Dai, Ming-Chun Tien, Jonathon S. Barton, Arne Leinse, René G. Heideman, Daniel J. Blumenthal, and John E. Bowers. “Ultra-low-loss high-aspect-ratio Si_3N_4 waveguides. Optics express 19, no. 4 (2011): 3163-3174.

[11] Takafumi Chiba, Hideaki Arai, Hideki Nounen, Katsumi Ohira, “Waveguide interleaving filters,” Proc. SPIE 5246, Active and Passive Optical Components for WDM Communications III, 532 (August 19, 2003).

[12] Cardenas, Jaime, Carl B. Poitras, Jacob T. Robinson, Kyle Preston, Long Chen, and Michal Lipson. “Low loss etchless silicon photonic waveguides.” *Optics express* 17, no. 6 (2009): 4752-4757.

[13] Akulova, Yuliya A., Gregory A. Fish, Ping-Chiek Koh, Clint L. Schow, Peter Kozodoy, Anders P. Dahl, Shigeru Nakagawa et al. “Widely tunable electroabsorption-modulated sampled-grating DBR laser transmitter.” *IEEE Journal of Selected Topics in Quantum Electronics* 8, no. 6 (2002): 1349-1357.

[14] Michael Belt, and Daniel J. Blumenthal. “Erbium-doped waveguide DBR and DFB laser arrays integrated within an ultra-low-loss Si_3N_4 platform.” Optics express 22.9 (2014): 10655-10660.

[15] Davenport, Michael L., and John E. Bowers. “Efficient and broad band coupling between silicon and ultra-low-loss silicon nitride waveguides.” *Photonics Conference (IPC), 2016 IEEE*. IEEE, 2016.

[16] Piels, Molly, et al. “Low-loss silicon nitride AWG demultiplexer heterogeneously integrated with hybrid III–V/silicon photodetectors.” *Journal of Lightwave Technology* 32.4 (2014): 817-823.

[17] S. Gundavarapu, M. Puckett, T. Huffman, R. Behounin, J. Wu, T. Qiu, G. Brodnik, C. Pinho, D. Bose, P. Rakich, J. Nohava, K. Nelson, M. Salit, D. Blumenthal, “Integrated Waveguide Brillouin Laser”, arXiv:1709.04512 [physics.optics].

Chapter 2

Si_3N_4 Ultra-Low-Loss Waveguide (ULLW) Platform

The ultra-low-loss waveguide (ULLW) platform used in this work was first reported by Jared Bauters et al. [1] with waveguide losses less than 0.1dB/m. This ultra-low waveguide loss enables complex photonic circuits to be integrated on chip. Previous waveguides in this platform utilized wafer bonding to create the upper cladding, enabling high quality thermal oxide to be used as the upper cladding and generating and nearly symmetric layer stack. The devices in this dissertation are designed to be further integrated with additional components that a bonded cladding would prohibit. In this chapter, the loss sources within these waveguides, their fabrication, and their properties are discussed.

The performance of planar waveguides can vary greatly depending on the materials and techniques used in fabrication. For example, etches and depositions must be designed to minimize roughness between interfaces and reduce material absorption. In addition, the waveguide geometry, film indices, and thickness must be accurately controlled, or the functionality of many critical components such as directional couplers can vary and change the performance of an entire photonic circuit. This chapter will focus on the design, fabrication, and optimization of the Si_3N_4 ULLW platform.

2.1 Waveguide Overview

Dielectric waveguides require a high index core surrounded by a low index cladding to confine and guide light. In the case of our Si_3N_4 ULLW platform, a LPCVD Si_3N_4 core is utilized, with an index of n=1.93-1.98, clad by SiO_2, with an index of n=1.45, schematically shown in

Fig. 2(a). The index variation of the core is given to reflect a variety of deposition conditions for Si_3N_4 for different stresses. The confinement of the core is determined by the index contrast between the core and cladding, with a larger contrast creating a more confined mode, and by the waveguide geometry itself, with thicker and wider cores creating higher confinement. The core thicknesses used in this work range from 40nm to 175nm. As an example, the mode intensity profile for the TE mode is shown in Fig. 2(b) for a 175nm-thick core. At a given thickness of the high aspect-ratio waveguide, there is a corresponding waveguide width at which multiple waveguide modes are supported. Additional modes have different effective indices, core confinements, and critical bend radii.

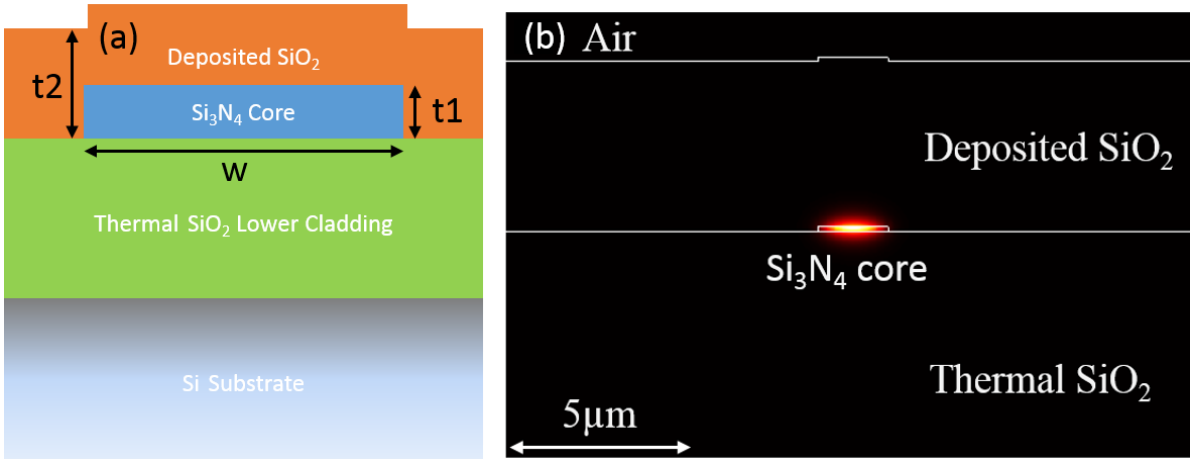

Fig. 2. (a) Waveguide schematic, t1 is the thickness of the core, varying from 40nm to 175nm, w is the width of the core, varying from 7µm to 2.2µm, and t2 is the upper cladding thickness, varying from 6µm to 1µm. (b) The simulated TE mode intensity, for a 175nm-thick, 2.2µm-wide waveguide.

The confinement of the mode and its intensity profile around the core determine some of the most important characteristics of the waveguide: its propagation loss and bending limit. The ULLW platform achieves low losses by controlling the core geometry to reduce scattering loss from the core and cladding interfaces. Techniques that lead to reduced scattering losses (thinner cores) also increase the critical bend radius, where the bend loss dominates the propagation loss, creating a trade-off in waveguide performance.

Low scattering losses alone are not sufficient to produce low propagation loss waveguides, if the material absorption is significant. Deposition and anneal techniques are used to minimize material impurities, particularly hydrogen, to reduce absorption losses. Additionally, very high thickness accuracy is required on the thin cores to maintain consistent photonic circuit properties, like directional couplers, between multiple depositions.

2.2 Fabrication Process

The fabrication steps for the ULLWs are depicted in Fig. 3. Fabrication begins with a Si wafer 100mm in diameter. The lower cladding is formed by thermally growing 15µm of oxide on the wafer. The lower cladding must be very thick to isolate the waveguide mode from the high index Si substrate [2], particularly for the low-confinement waveguide designs. Thermal SiO_2 is chosen as the highest-quality film, especially given how thick the layer is.

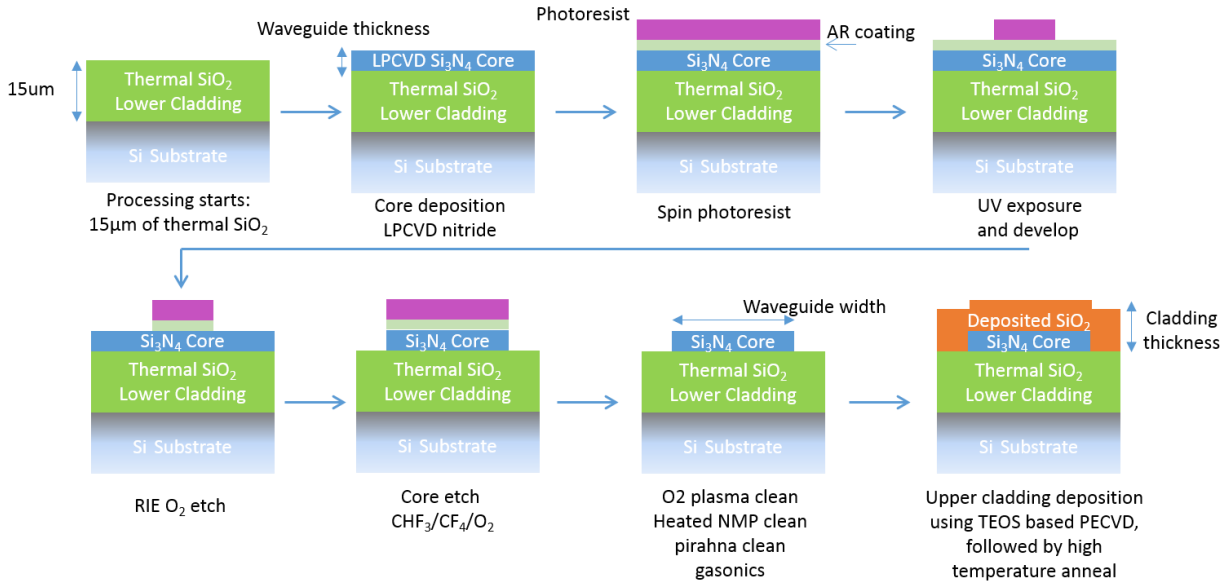

Fig. 3. ULLW process flow.

The Si_3N_4 core is deposited using low pressure chemical vapor deposition (LPCVD). LPCVD can produce stoichiometric films with very high thickness accuracy and uniformity

over the wafer. Given that the core thickness can be as small as 40nm, small thickness variations, on the order of a few nanometers, can cause substantial change in waveguide characteristics. The core is patterned using DUV lithography (λ=248nm) and a CHF3/CF4/O2 etch in an inductively coupled plasma (ICP) etcher.

After the Si_3N_4 core is etched, the wafer must be thoroughly cleaned before upper cladding deposition. The cleaning process starts with an O_2 plasma (in an ICP) to remove any by-products from the etching. This process is followed by 80°C NMP (N methyl pyrrolidone) stripper bath for several minutes, repeated twice. The wafer is then cleaned in a 110°C piranha solution. An additional O_2 plasma clean completes the cleaning process. Although other cleaning variations may be used, having a clean wafer before proceeding to upper cladding deposition is critically important. If residue or contaminants are present during upper cladding deposition, scatter centers can be formed and can be sources of loss and reflections.

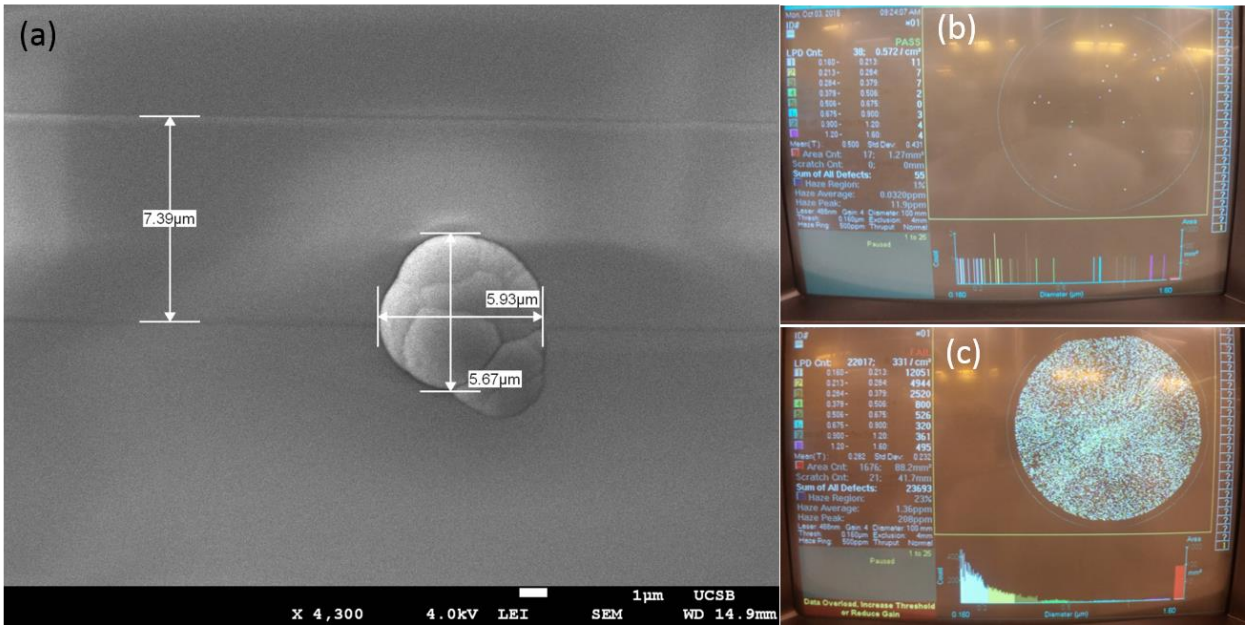

Fig. 4. (a) Scanning electron micrograph of scattering center in sputtered cladding. This causes significant loss in waveguide propagation (>3dB). (b) and (c) are scatter counts using Tencor Surfscan before and after sputter deposition on the same wafer. Prior to deposition, a total of 38 scatterers were counted, while after deposition, scatterers in excess of 22,000 were counted.

The preferred method for depositing the upper cladding in this work is plasma-enhanced chemical vapor deposition (PECVD), using tetraethoxysilane (TEOS) as a Si precursor for its reduced hydrogen content compared to silane (see Section 2.3.3). Sputtered claddings are also used, particularly for thin claddings, or in devices that cannot be annealed (see Section 2.3.3). However, many devices in this work require 6μm-thick claddings, and it was found that thick sputtered claddings had large, isolated scatterers, such as the one shown in Fig. 4, that reduced the yield of large area devices. Regardless of the upper cladding deposition method used, the upper cladding is annealed to drive out impurities, most notably, any hydrogen present.

At this stage in processing, the waveguides are capable of low-loss propagation; however, additional functionality can be added with continued processing. Previous waveguides on this platform utilized wafer bonding to create the upper cladding [1]-[3], whereas the devices in this dissertation are designed to be further integrated with other components that a bonded cladding would prohibit. This could include further processing for heaters [4] or integration with active elements through a doped erbium layer [5] or a transition to a bonded III/V material [6][7]. The process presented here is fully integrable with these components and is also CMOS compatible.

2.3 Waveguide Losses

There are a number of ways light can be lost as it travels through the waveguide. The sum of these effects determines the propagation loss expressed in dB/m. Three primary sources of loss will be considered here. These loss sources are scattering loss, material absorption, and waveguide bend loss.

2.3.1 Scattering Loss

Scattering loss results from roughness between the core and cladding interfaces. The scattering loss is proportional to the magnitude of the electric field at the interface, the difference of the indices of the materials ($n_{core}^2 - n_{clad}^2$), and the square of the root-mean square (RMS) roughness of the interface [8], represented as σ. The top and bottom surfaces of the waveguides typically have an RMS roughness of less than 0.2nm, a result of the deposition techniques. The sidewalls of the waveguide, created by the lithography and dry etch, can have RMS roughnesses (σ) on the order of a few nanometers. The sidewall roughness is defined as the deviation from the ideal straight waveguide edge, depicted top down in Fig. 5(a). This deviation can be plotted as a function of length along the waveguide to quantify the roughness, shown in Fig. 5(b).

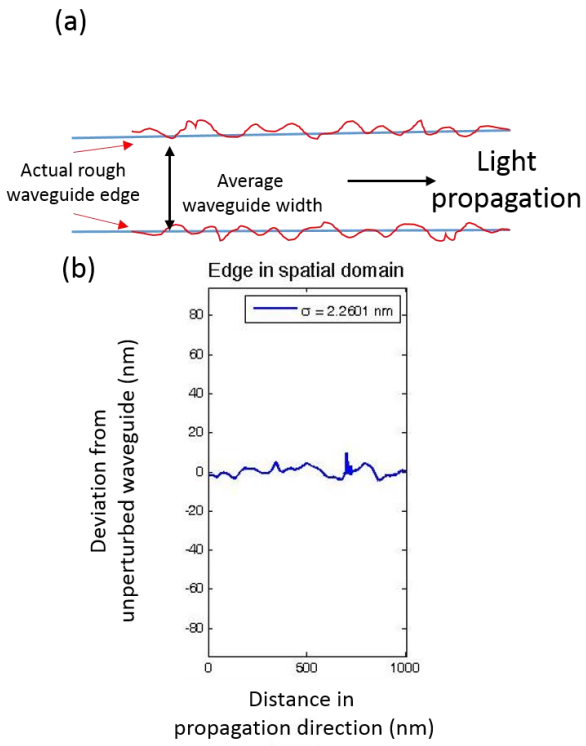

Fig. 5. (a) Depiction of line edge roughness. (b) Measured line edge roughness by plotting the deviation of the waveguide edge from the unperturbed edge vs propagation distance.

The impact of the rough surfaces on the propagation loss was simulated following [2] and [8] and uses the indices of the materials measured by ellipsometry. The present simulation was defined to output the loss parameter Π, which is the propagation loss normalized to an RMS roughness σ^2=1nm^2. The waveguide propagation loss for any roughness can be deduced from Π by the equation below, where α is the waveguide propagation loss in dB/m:

$$\alpha = \sigma^2_{sidewall} * \Pi_{\text{sidewall}} + \sigma^2_{top/bottom} * \Pi_{\text{top/bottom}}$$

The mode in the program FIMMWAVE was simulated using film mode matching [9] to find the electric field intensity at the interfaces. The mode intensity profiles for both a thick 175nm core and a thin 40nm core are shown in Fig. 6 (a) and (b), respectively. The thicker waveguide core confines the light to the core, creating higher intensities at the core/cladding interface than the dilute thin core mode, resulting in higher scattering loss for the thicker waveguides.

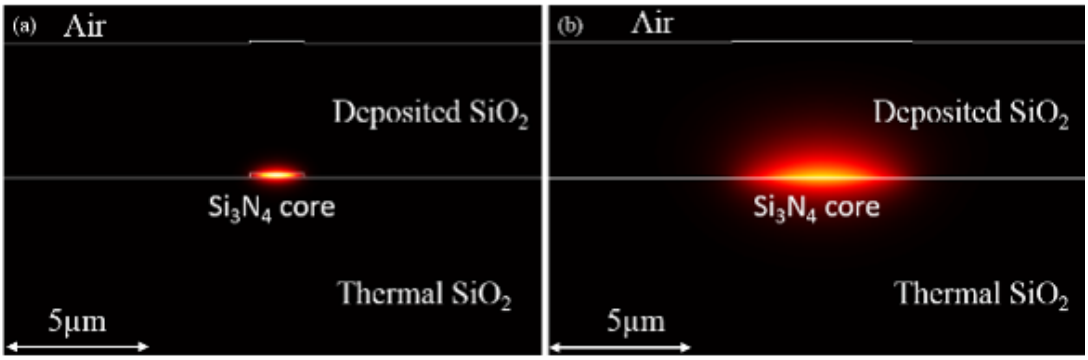

Fig. 6. Simulated TE mode intensity profile for (a) 175nm x 2.2µm waveguide and 40nm x 7µm waveguide. Both have an upper cladding thickness of 6µm. (a) has 33.8% of the power confined to the core, while (b) has 2.5% of the power confined to the core.

The resulting loss parameter Π is plotted for both the top/bottom surfaces and the sidewalls of the waveguide in Fig. 7(a) and 7(b), respectively. The coupling length measurement and fit in [2] were used. Variations in the coupling length impact the values of loss generated but do not affect the trends of loss and waveguide core design.

The loss parameter Π is shown for three different core thicknesses with varying widths in Fig. 7, with $\Pi_{top/bottom}$ plotted in (a) and $\Pi_{sidewalls}$ plotted in (b). Because $\Pi_{top/bottom}$ ranges from 1 to 10, and the surface roughness of the interfaces is on the order of 0.02nm, negligible scattering loss was expected to be contributed from these interfaces, less than 0.004dB/m for any thickness or width.

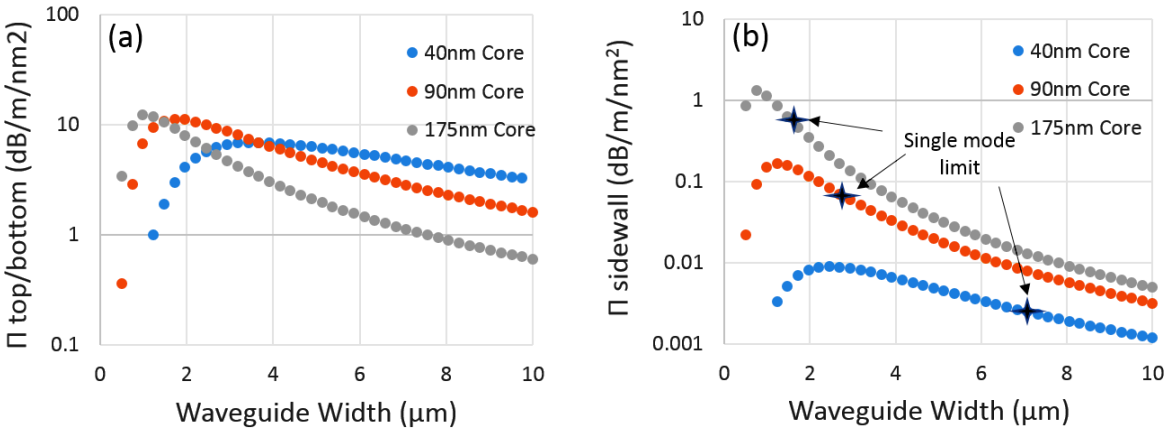

Fig. 7. Simulated (λ=1550nm) scattering losses for (a) top and bottom surfaces and (b) sidewalls for the TE mode. The loss in dB/m is obtained by multiplying the plotted Π value by the mean square deviation, σ^2.

The $\Pi_{sidewalls}$ parameter varies from 1 to below 0.01, depending on the thickness and width of the waveguide. This range corresponds to a range of 16dB/m to 0.16dB/m for a typical RMS roughness of σ 4nm, with thinner and wider cores having substantially lower loss values. Many device functionalities, such as rotational sensing, require that the waveguide support only a single TE (transverse electric) mode. The single-mode limit width of each core thickness is marked in Fig. 7(b). This factor further increases the scattering performance for smaller thicknesses, as they can also be much wider before becoming multi-mode.

There are two primary factors driving the reduced scattering loss of thinner cores. The first is that the thinner cores have physically smaller sidewalls, which means a smaller surface from which to scatter. The second is that they also have much larger modes, as shown in Fig. 6, resulting in a lower electric field intensity and, thus, lower scattering loss.

2.3.2 Bend Loss

Bend loss occurs as light radiates from the guided mode as the mode moves through curved waveguide structures, with higher losses occurring at tighter bending radii. This element is relevant for device performance, not only for the losses incurred but also because the footprint of the device is, in a large part, determined by the bending radii used.

Fig. 8 depicts a constant phase plane of light propagating around a curved waveguide. The tangential speed of the phase velocity increases with increasing radius to maintain this plane. The outer edge of the waveguide mode would need a speed greater than that of the speed of light to remain within this plane and is radiated away from the waveguide mode.

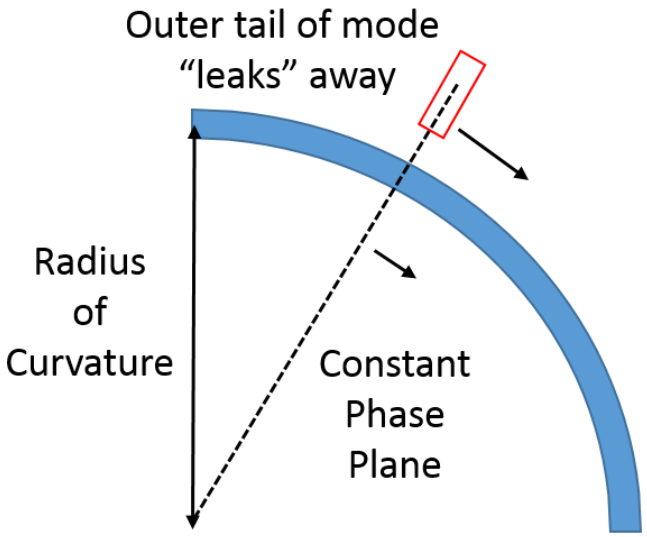

Fig. 8. Schematic of bend loss in a curved waveguide.

Intuitively, the amount of light lost in a bend can be expected to increase with larger mode sizes, as a larger portion of the propagating light cannot meet the phase condition. This bend loss can be simulated using perfectly matched layers [10]. Fig. 9 shows the results of bend loss simulations for the 90nm and 175nm core, also used in the scattering loss simulations, over varying radii.

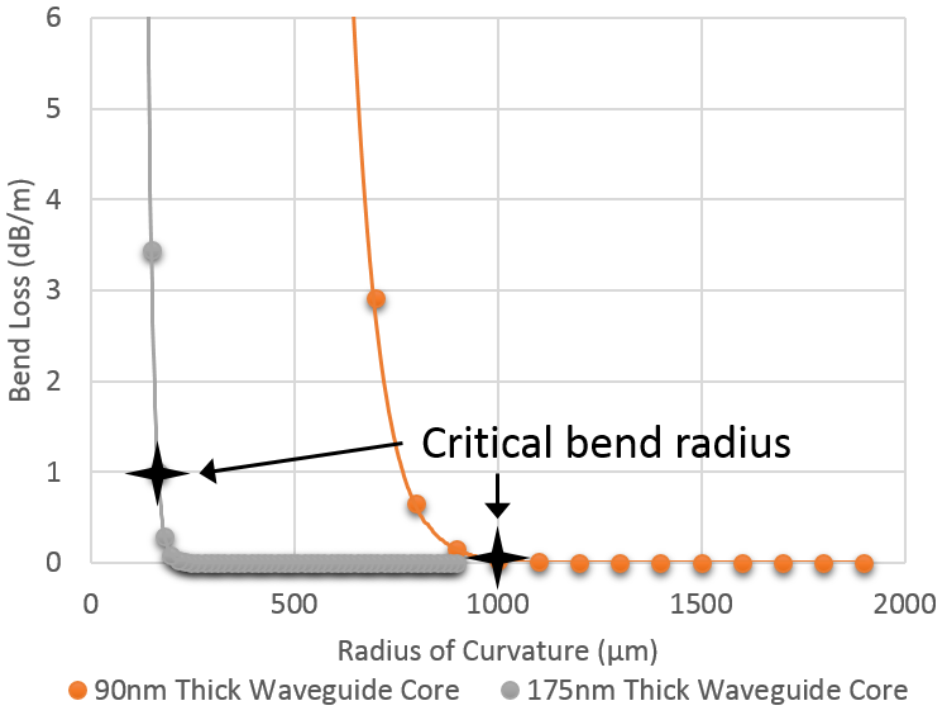

Fig. 9. Bend loss (λ=1550nm) simulation for various core thicknesses. This is simulated for the fundamental TE mode at the single-mode waveguide width for each thickness. The loss increases exponentially with decreasing radius. The critical bend radius is identified, which is dependent on the scattering loss of the respective waveguides.

The plot above shows that the waveguide thickness has a large impact on the bend loss of the waveguide. The data points are fitted with an exponential trend line, and the loss increases exponentially with decreasing radius for any waveguide thickness. Because small process variations, such as a thinner core deposition or smaller waveguide width, can produce large increases in the bend loss, the bending radius is chosen such that the loss is negligible in comparison to the typical scattering loss of the waveguide core, identified as the critical bend radius. In the case of a 90nm waveguide, 1-3dB/m of scattering loss is typically observed, and thus, bend losses are designed to be less than 0.2dB/m, requiring a bend radius on the order of 1mm. The 175nm core, on the other hand, has scattering losses of approximately 15dB/m, meaning that a bend radius of less than 300µm can be utilized.

The difference in scattering loss and bend radius of the different core thickness constitutes one of the most fundamental design parameters of low-loss photonic circuits. The waveguide losses and bend radii of the 40nm and 175nm core differ by two orders of magnitude. When considering the footprint of a device in area, their difference increases to approximately four orders of magnitude. This great variance in performance enables varying applications. Designing the waveguide geometry, and therefore bend loss and scattering loss characteristics, is addressed in each device chapter separately.

2.3.2.1 Bend Loss and Polarization

The high aspect ratio of the waveguides causes the TE and TM (transverse magnetic) modes to experience significantly different confinement and bend loss characteristics. In the case of a 40nm waveguide, the TE mode has a simulated effective area of 29μm^2, while the TM mode has an effective area of 61.4μm^2. As a result, the TM mode requires a much larger bend radius to avoid extremely high losses. The radius of the waveguide can be chosen such that the TE mode experiences negligible loss, while the TM mode is radiated away.

A 40nm core waveguide bending at a radius of 9mm has a simulated TE bend loss of 0.001dB/m, whereas the simulated TM bend loss is greater than 1000dB/m. These waveguides can therefore be used as polarizers and have been demonstrated to have a (measurement-limited) polarization extinction ratio as high as 75dB [11], an advantage for many applications, such as rotational sensing (see Chapter 6).

2.3.2.2 Bend Loss and Upper Cladding Thickness Loss

The confinement of the waveguide mode is affected by the thickness of the deposited upper cladding. Therefore, the bend loss is also impacted by the upper cladding design. The plots

shown thus far have used typical cladding thicknesses. Fig. 10 shows the simulated bend loss as a function of upper cladding thickness for a 40nm core.

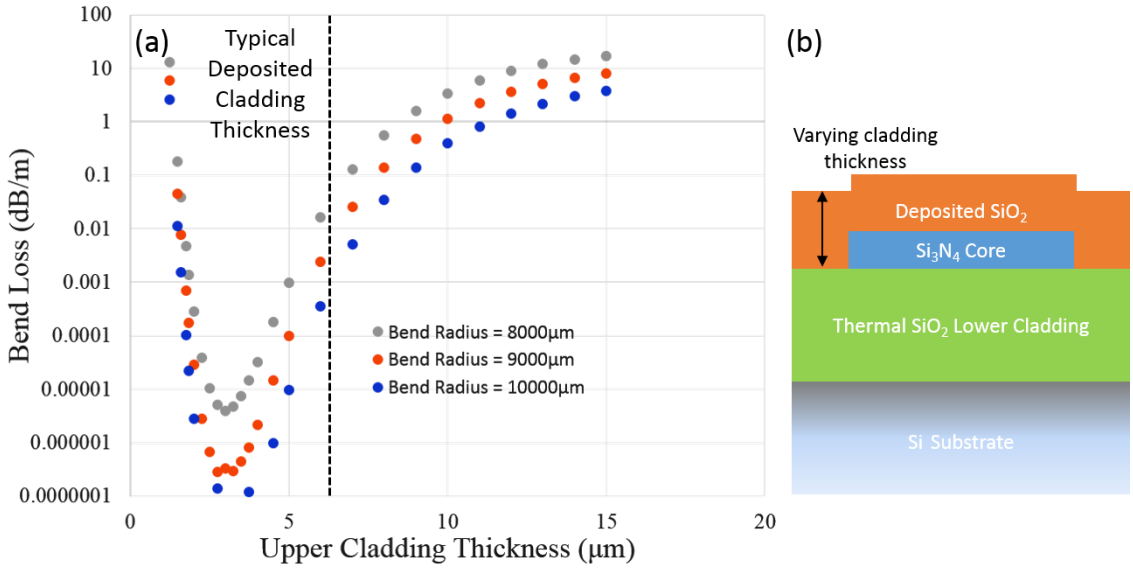

Fig. 10. (a) Simulated (λ=1550nm) bend loss as a function of upper cladding thickness for a 40nm x 7µm waveguide for the TE mode. (b) Schematic of waveguide with cladding thickness variable identified.

As seen in the plot, there is an upper cladding thickness that yields the best bend characteristics, approximately 3.5µm in this case. At lower thicknesses, the mode is compressed horizontally, increasing the bend loss. As the upper cladding thickness increases, the mode takes its more usual elliptical shape. Once the mode is no longer compressed, increasing the upper cladding allows the mode size to increase, once again increasing the bend loss. The minimum bend loss point is determined by these two competing effects.

The scattering loss produced by the upper cladding and air interface is negligible because of the low surface roughness and electric field magnitude. However, if the surface is contaminated with dust, the mode can experience additional loss at very thin upper claddings. For a 40nm core, thicknesses greater than 6µm are used to ensure that the device functions well outside of the clean room.

2.3.3 Absorption Loss

The final loss mechanism that is considered is the material absorption loss. This loss is due to impurities within the core and cladding materials. When excited by light propagating in the waveguide, these impurities allow molecular vibrations and dissipate energy from the waveguide mode. The resultant absorption losses are described macroscopically as part of the complex index of the material, $\tilde{n}(\lambda) = n(\lambda) + jk(\lambda)$ where the imaginary component, k, accounts for affects that cause attenuation of the propagating wave [12]. Deposited claddings can contain impurities that impact waveguide performance. Hydrogen impurities have absorption lines centered on 1480nm and 1510nm, for Si-H and N-H, respectively. PECVD deposition techniques that have silane as a Si precursor can produce high hydrogen content [13]. Regardless of the deposition technique, high-temperature anneals of the deposited cladding can reduce material absorption as well as scattering loss by inter-diffusion of the core/cladding interface [14]. Fig. 11 shows the measured waveguide loss for a 90nm core with sputter- and PECVD-based claddings before and after a 7hr 1050°C anneal.

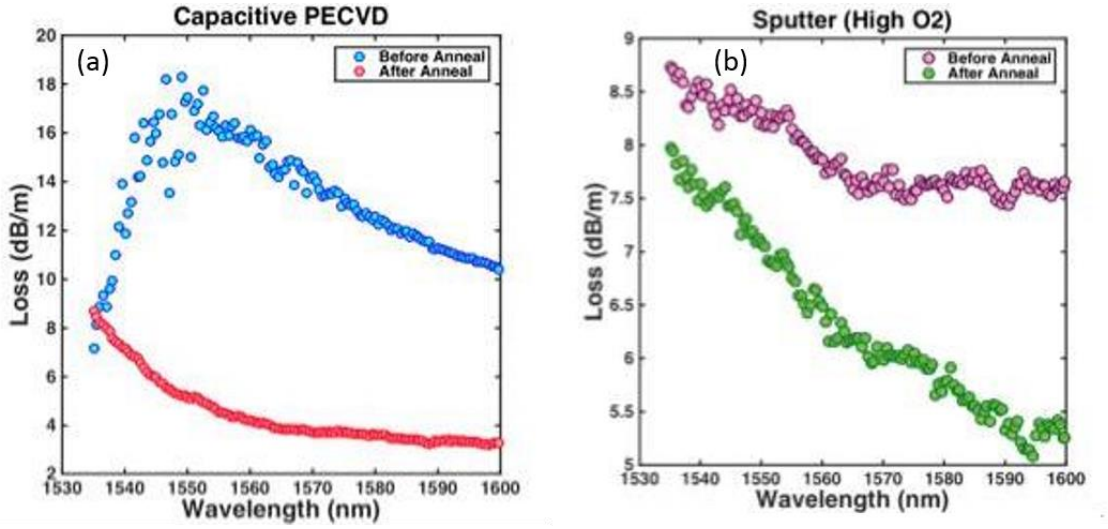

Fig. 11. Measured loss vs wavelength for (a) PECVD and (b) sputter-deposited claddings, before and after a 1050°C anneal. Both are for a 90nm x 2.8µm waveguide.

Comparing the above losses before annealing, it is clear that the PECVD oxide has substantially higher loss, particularly around 1550nm. Post anneal, both samples have improved loss performance, with the PECVD loss rate decreasing dramatically, lower than that of the sputtered cladding. This a result of driving hydrogen impurities out of the PECVD film. Higher-temperature anneals can further improve the loss performance, primarily by decreasing the scattering loss. Fig. 12 shows the measured waveguide loss for a single device that was annealed at 1050°C for 7hr, then at 1150°C for 2hr. The loss decreases essentially agnostic to the wavelength, which indicates that the loss reduction is not a result of driving impurities out of the film, as that would change the shape of the plot, as in Fig. 11. This experiment was limited by the annealing furnace available, and even higher-temperature anneals could possibly show even greater improvement [15].

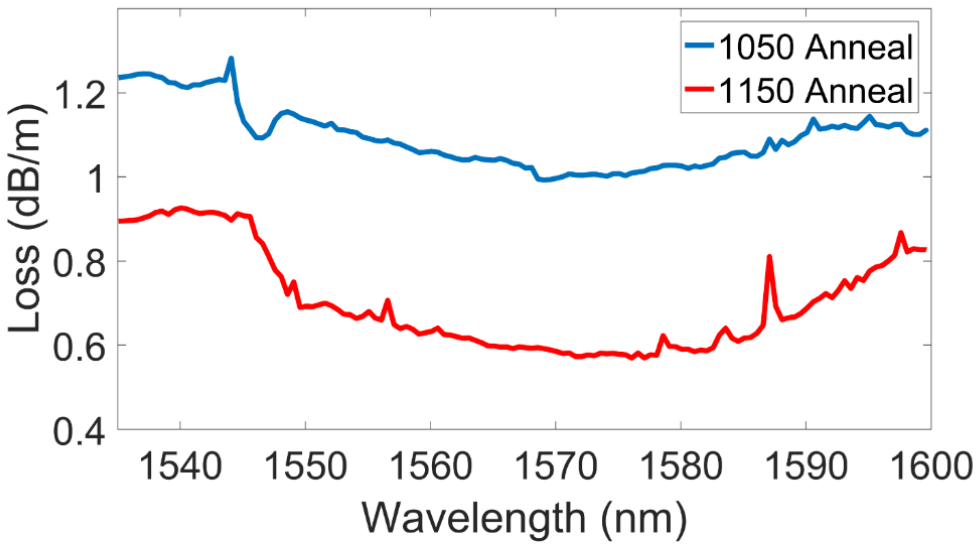

Fig. 12. Measured loss vs wavelength for the same device annealed initially at 1050°C and then 1150°C. The sample is a 40nm x 7µm waveguide.

2.4 Measuring Ultra-Low-Loss Waveguides

Waveguides with higher losses can be measured by inputting light into waveguides of various lengths and measuring the output intensity. The intensity should decrease with the length of the waveguide, from which the waveguide loss can be determined. However, performing such a measurement is impractical with waveguide losses that require lengths far greater than the dimensions of the chip. The entire area of the chip would need to be dedicated to spirals of various lengths to measure an appreciable change in output intensity.

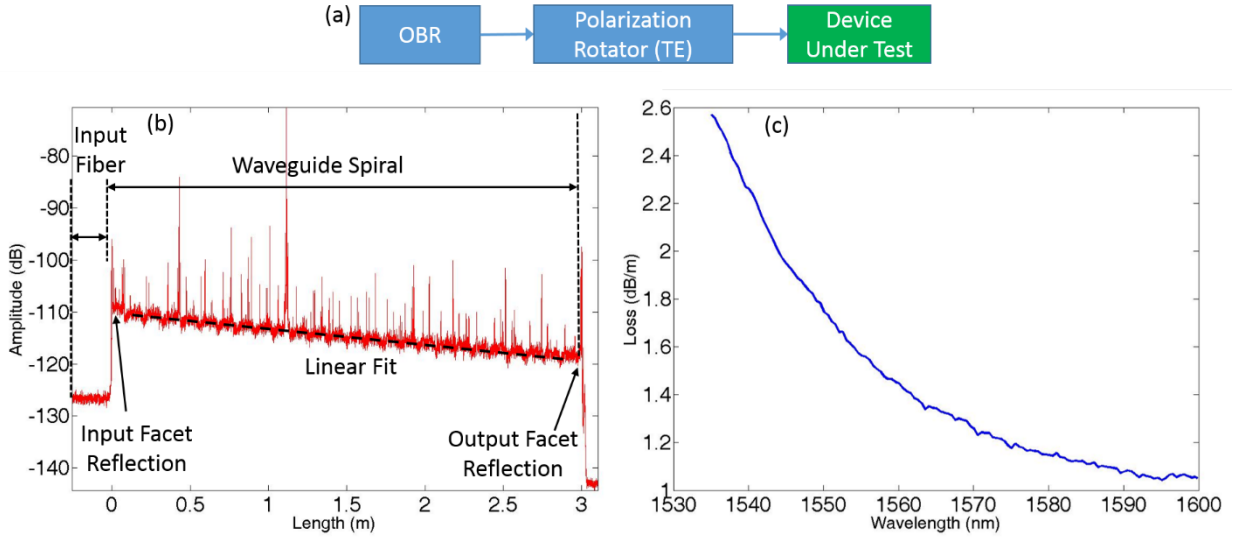

Fig. 13. (a) Loss measurement setup. (b) OBR trace of a 3-meter coil with periodic crossings. (c) The resulting loss fit.

Instead, the waveguide can be evaluated using an optical backscatter reflectometer (OBR). There are other methods, such as using a resonant cavity and fitting the wavelength dependence [16], but the OBR method also grants further insight into the waveguides' functionality. A reflectometer is capable of measuring the magnitude of optical power that is backscattered after a certain time t_0. However, if waveguides with features of a known length are measured, the group index can be fitted [2] and the reflection time can be translated to a propagation distance L_0. The amount of power that is backscattered is directly proportional to the amount

of power present at L_0. A typical OBR measurement setup is shown schematically in Fig. 13(a), and a resulting OBR trace for a 3-meter spiral is shown in Fig. 13(b).

As the average backscatter level in the trace is proportional to the intensity of light at that point in the waveguide, the slope of the trace is the loss of the waveguide (with an additional factor of 2, as power needs to traverse down the waveguide and return, covering L_0 twice). A line can be fitted to this slope to measure the waveguide loss, shown in Fig. 13(c). Waveguides (or fibers) with a higher loss level will have a higher slope, but also a higher magnitude of reflection, due to a larger portion of the light scattering to the detector. This difference is visible at the transition between the fiber and the chip. The fiber, which has very low losses, is essentially flat at this length scale and has a lower-magnitude reflection than the higher scattering loss waveguide. These types of observations are very useful for understanding waveguides that might have unexpected results. Details for the OBR loss fitting method can be found in [2].

2.5 Conclusion

In this chapter, the design, fabrication, and measurement of ULL waveguides was discussed. All of the fabrication techniques used are compatible with those of a CMOS foundry. Three primary sources of loss were introduced, and techniques to optimize the waveguides around these losses were discussed. The scattering losses of the waveguide depends strongly on the geometry chosen, with scattering losses increasing with increasing core thickness. The bend loss exhibits the opposite trend and is also impacted by the upper cladding thickness chosen. Lastly, the material absorption depends on the deposition method chosen and can be greatly mitigated by high-temperature annealing.

Table 2. Typical propagation loss and bend limits of varying core thicknesses for the TE mode.

Core Thickness (nm)	Scattering Loss	Critical Bend Radius (mm)
40	0.2 — 0.5	11
60	0.8 — 3	3
90	1 — 6	1
175	10 — 20	0.3

The trade-off between the waveguide bend limit and propagation loss represents an extremely important design parameter for a photonic circuit. Depending on the application of the device, the footprint, and therefore the bend radius, for the waveguide propagation loss can be the limiting factor that determines what waveguide geometry is appropriate. Table 2 summarizes typical values for propagation losses and bend limitations for different core thicknesses. These values are "typical," in that assumptions regarding single-mode design and upper cladding thickness can significantly change these numbers. This table will be referenced when selecting the waveguide geometry for the various devices in this dissertation.

2.6 References

[1] Bauters, Jared F., Martijn JR Heck, Demis D. John, Jonathon S. Barton, Christiaan M. Bruinink, Arne Leinse, René G. Heideman, Daniel J. Blumenthal, and John E. Bowers. "Planar waveguides with less than 0.1 dB/m propagation loss fabricated with wafer bonding." Optics Express 19, no. 24 (2011): 24090-24101.

[2] Bauters, Jared F., Martijn JR Heck, Demis John, Daoxin Dai, Ming-Chun Tien, Jonathon S. Barton, Arne Leinse, René G. Heideman, Daniel J. Blumenthal, and John E. Bowers. "Ultra-low-loss high-aspect-ratio Si 3 N 4 waveguides." Optics express 19, no. 4 (2011): 3163-3174.

[3] Spencer, Daryl T., Jared F. Bauters, Martijn JR Heck, and John E. Bowers. "Integrated waveguide coupled Si 3 N 4 resonators in the ultrahigh-Q regime." Optica 1, no. 3 (2014): 153-157.

[4] Moreira, Renan L., John Garcia, Wenzao Li, Jared Bauters, Jonathon S. Barton, Martijn JR Heck, John E. Bowers, and Daniel J. Blumenthal. "Integrated ultra-low-loss 4-bit tunable delay for broadband phased array antenna applications." IEEE Photon. Technol. Lett 25.12 (2013): 1165-1168.

[5] Belt, Michael, and Daniel J. Blumenthal. "Erbium-doped waveguide DBR and DFB laser arrays integrated within an ultra-low-loss Si 3 N 4 platform." Optics express 22.9 (2014): 10655-10660.

[6] Davenport, Michael L., and John E. Bowers. "Efficient and broad band coupling between silicon and ultra-low-loss silicon nitride waveguides." Photonics Conference (IPC), 2016 IEEE. IEEE, 2016.

[7] Piels, Molly, et al. "Low-loss silicon nitride AWG demultiplexer heterogeneously integrated with hybrid III–V/silicon photodetectors." Journal of Lightwave Technology 32.4 (2014): 817-823.

[8] T. Barwicz and H. Haus, "Three-dimensional analysis of scattering losses due to sidewall roughness in microphotonic waveguides." J. Lightwave Technol. 23.9 (2005): 2719-2732.

[9] Sudbo, A. Sv. "Film mode matching: a versatile numerical method for vector mode field calculations in dielectric waveguides." Pure and Applied Optics: Journal of the European Optical Society Part A 2.3 (1993): 211.

[10] Bienstman, P., Six, E., Roelens, A., Vanwolleghem, M., & Baets, R. (2002). "Calculation of bending losses in dielectric waveguides using eigenmode expansion and perfectly matched layers." IEEE Photonics technology letters, 14(2), 164-166.

[11] Bauters, J. F., Heck, M. J. R., Dai, D., Barton, J. S., Blumenthal, D. J., & Bowers, J. E. (2013). "Ultralow-Loss Planar Si_3N_4 Waveguide Polarizers." IEEE Photonics Journal, 5(1), 6600207-6600207.

[12] von Hippel, A. R., & Morgan, S. O. (1955). "Dielectric materials and applications." *Journal of The Electrochemical Society*, *102*(3), 68C-68C.

[13] Lanford, W. A., & Rand, M. J. (1978). "The hydrogen content of plasma-deposited silicon nitride." Journal of Applied Physics, 49(4), 2473-2477.

[14] Germann, R., Salemink, H. W. M., Beyeler, R., Bona, G. L., Horst, F., Massarek, I., & Offrein, B. J. (2000). "Silicon oxynitride layers for optical waveguide applications." Journal of the Electrochemical Society, 147(6), 2237-2241.

[15] Shaw, Michael J., Junpeng Guo, Gregory A. Vawter, Scott Habermehl, and Charles T. Sullivan. "Fabrication techniques for low-loss silicon nitride waveguides." In Proc. SPIE, vol. 5720, pp. 109-118. 2005.

[16] Adar, R., Y. Shani, C. H. Henry, R. C. Kistler, G. E. Blonder, and N. A. Olsson. "Measurement of very low-loss silica on silicon waveguides with a ring resonator." *Applied physics letters* 58, no. 5 (1991): 444-445.

Chapter 3

Ring Resonator Theory

Multiple devices within this dissertation are formed by circular waveguide paths called ring resonators. In this chapter, the theory of ring resonators and how to control their functionality with waveguide properties is discussed. A resonant device, at its most basic, is a structure that couples the mode of propagating light back into itself. This coupling is accomplished within a ring resonator by physically looping a waveguide back upon itself to form a ring. As light travels around the ring and interferes with itself, it will either constructively or destructively interfere, determined by the wavelength of light and the effective length of the cavity, expressed as $n_{eff} * L = N * \lambda$, where n_{eff} is the effective index of the mode, L is the length of the ring, N is the mode number, and λ is the wavelength. Light that constructively interferes resonates within the cavity and builds up to a higher intensity than the original input light. This wavelength is said to be "on resonance." Light that that destructively interferes is rejected from the ring and is described as "off resonance."

3.1 Transfer Functions of Single-Ring Resonators

In order to design ring resonator structures with the correct properties, the transfer function of light traveling between various ports must be derived. Mason's Rule, a feedback theory method, is extremely useful in this circumstance. Fig. 14 shows the schematic of a dual-bus ring resonator.

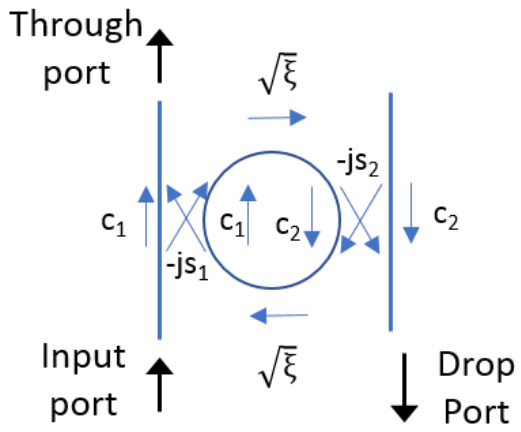

Fig. 14. Schematic of a dual-bus ring resonator.

Light passing through couplers without coupling is represented by the parameter C_i, while light coupling between waveguides is represented by the parameter S_i, and the attenuation and phase of light traveling around a ring is represented by the parameter ξ. These parameters are defined in the equations below. Here, L is the round-trip length of the ring, α is the propagation loss of the waveguide, κ is the power coupled across the coupler, γ is the power lost in the coupler, and β is the waveguide propagation constant.

$$C_i = \left((1-\kappa_i)(1-\gamma)\right)^{1/2}$$

$$-jS_i = -\left((1-j\gamma)\kappa_i\right)^{1/2}$$

$$\xi = e^{\alpha L/2} e^{-j\beta L}$$

The derivation of the transfer function from [1] is followed. First, the transfer function between the input and the drop port is calculated. To use Mason's rule, a series of parameters involving forward paths and loops must be defined. A forward path is a linked series of nodes encountering no node more than once. A loop is a path that begins and ends on the same node. The loop or path gain is the product of all the links within the loop. If two loops have no nodes

in common, they are said to be non-touching. The transfer function, or input–output transmittance relationship, between two nodes is given by the equation below:

$$Transfer\ function = \frac{1}{\Delta}\sum_{i=1}^{n} T_i \Delta_i$$

T_i is the gain of the i_{th} forward path between the input and output, and n is the total number of forward paths. The signal flow graph determinant, Δ, is given as:

$$\Delta = 1 - \sum_{i} T_I + \sum_{i,j} T_i T_j - \sum_{i,j,k} T_i T_i T_k + \cdots$$

In each product summation, only products of non-touching loops are included. The sign of the summation is determined by the number of products within the summation: an odd number of product is negative and an even number of products is positive. Δi in the transfer function equation is the determinant Δ of all loops that do not have a node in common with the T_i path.

Following Mason's Rule, the transfer function for the drop port and through port of the dual-bus ring resonator in Fig. 14 can be deduced:

$$\frac{Drop\ Port}{Input\ Port} = \frac{s_1 s_2 \sqrt{\xi}}{1 - c_1 c_2 \xi}$$

$$\frac{Through\ Port}{Input\ Port} = \frac{c_1 - c_2 \xi}{1 - c_1 c_2 \xi}$$

This result can be adjusted for a single-bus resonator by simply changing κ_2 to 0 and adjusting c_2 and s_2 accordingly.

$$\frac{Through\ Port}{Input\ Port} = \frac{c_1}{1 - c_1 c_2 \xi}$$

The resulting spectra for both a single-bus and dual-bus resonator are plotted in Fig. 15 for a variety of coupling values.

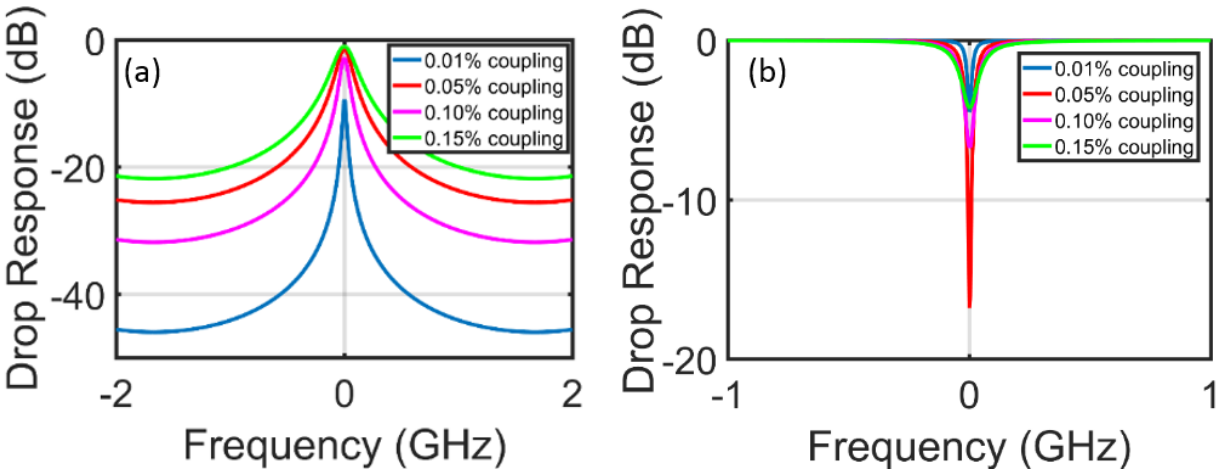

Fig. 15. Example spectra of (a) a dual-bus ring resonator and (b) a single-bus ring resonator. In both of these simulations R= 9mm and α = 3dB/m.

3.2 Figures of Merit

There are multiple ways to evaluate a resonator, depending on the application, one of the most fundamental of which is the Q of the resonator. The Q factor is the amount of energy stored within the resonator divided by the power lost per optical cycle (round trip time of resonating light):

$$Q = \omega \frac{T_{rt}}{L}$$

Here, ω is the angular frequency of the resonating light, T_{rt} is the round-trip time of the resonator, and L is the fractional power loss of the resonator per round trip. The Q can be further defined into intrinsic Q, Q_i, or loaded Q, Q_l. The loaded Q, Q_l, is the Q of the resonator including the loss of the couplers. It is also called the external Q. Q_i is the Q of the isolated resonator, if it has no couplers. The same ring resonator with varying couplers would have varying Q_l but the same Q_i.

The Q of the resonator can be expressed in many ways [2][3]. In the frequency domain, Q_l is represented by operational wavelength divided by the full width half maximum (FWHM) of

the resonator. In the time domain, it is linked to the photon lifetime, as it relates to the decay of optical intensity in the cavity, and can be measured via the cavity ring down time [4]. The resonator Q is a measure of the resonance's sharpness and is relevant for reference cavities, rapid switching, and non-linear ring resonators. Referring to Fig. 15, the FWHM of each resonator increases as the coupling parameter decreases, and therefore the Q_l increases. In addition, the Q_l of a single-bus resonator will, all things being equal, always be larger than the Q_l of a dual-bus resonator, as the dual-bus resonator has twice the coupling loss.

The extinction ratio (ER) of a resonator is the ratio of the highest and lowest detected power at the through or drop port. In a dual-bus resonator, the ER increases as the coupling parameter decreases. For a single-bus resonator, there is, notably, a critical coupling point at which the extinction ratio is maximum, which occurs when the propagation loss within the resonator matches the coupling loss of the resonator, and the output of the resonator destructively interferes with light in the bus waveguide. This critical coupling point also corresponds to the highest buildup of energy within the resonator, as can be shown from an energy conservation argument [2]. Energy must either exit the ring resonator through the bus or be lost within the resonator to scattering or bend losses. Since critical coupling is defined as a condition in which no power exits the ring via the bus, that means it is entirely lost within the ring. Because radiation and scattering losses are proportional to the intensity of light in the mode, it can be deduced that the intensity of light in the ring must be at its maximum for the power dissipated within the ring to be at a maximum. Thus, designing rings to access non-linearities at a lower on-chip power threshold should operate near this critical coupling point, which is relevant for Chapter 5.

The insertion loss (IL) of the resonator is the ratio of the input power over the output power, at the wavelength of highest transmission. This ratio is independent of any other losses of the measurement, such as coupling loss or system loss. In a dual-bus resonator, the insertion loss increases with decreasing coupling and can become significant for extremely low coupling values relative to the loss of the resonator.

The free spectral range (FSR) of the resonator is the span between two resonances, measured in frequency or wavelength. The FSR is independent of the number of buses the resonator has, as well as their coupling values. It is calculated as [2]:

$$FSR = \frac{\lambda^2}{n_g L}$$

The finesse of a cavity, F, a measure of the sharpness of the resonance compared to the density of resonances, is defined by the ratio of the FSR over the FWHM. The Q and finesse of a resonator can be related to each other by:

$$Q = \frac{n_{eff} L}{\lambda} \mathrm{F}$$

Resonators used as filters are also evaluated by their shape factor (SF) and ripple [1][5]. The shape factor is a representation of how quickly the resonance rolls off. The shape factor is defined as the unit-less ratio of the -1dB and the -10dB bandwidths. A shape factor approaching one represents a very rapid roll off from the resonance peak. Ripple is a measure of how flat the passband of the filter is. A filter with no ripple decreases from its maximum value at the peak to its minimum value in the stopband without increasing at any point. A filter with ripple has points where the filter value decreases and increases between the passband and the stopband. Ripple is measured in dB as the maximum increase in the transfer function between the passband and stopband. Fig. 17(c) shows a resonator with non-zero ripple.

3.3 Third-Order Ring Resonators

Serially coupled high-order ring resonators offer much more control of the resonance peak, often referred to as the passband in filters. In particular, "box-like" filter characteristics, which are very desirable for optical filtering, can be realized. In a serially coupled high-order resonator, light must travel through several coupled rings before it reaches the drop port. A third-order ring filter, which is relevant to this dissertation, is presented schematically below.

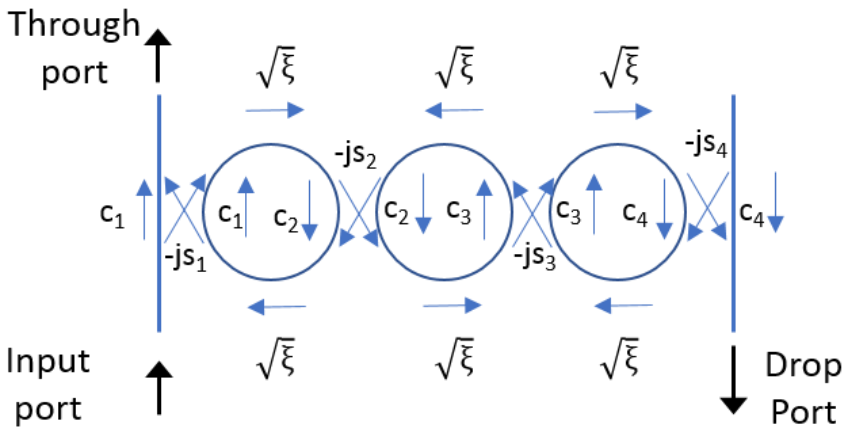

Fig. 16. Schematic of Third-Order Filter.

Using Mason's Rule as before allows for the derivation of the transfer function of the cascaded rings:

$$\frac{Drop\ Port}{Input\ Port} = \frac{s_1 s_2 s_3 s_4 \xi^{3/2}}{1 - c_1 c_2 \xi + c_1 c_3 \xi^2 + c_2 c_4 \xi^2 - c_1 c_4 \xi^3 + c_1 c_2 c_3 c_4 \xi^2}$$

For a given radius and propagation loss, the ratio of κ_1 and κ_2 determine the ripple, IL and ER of the filter. To minimize the filter IL, the bus-to-ring coupling constants are set to $\kappa_1 = \kappa_4$, and ring-to-ring coupling constants $\kappa_2 = \kappa_3$, as described in [1]. High ratio values of κ_2 to κ_1 will produce low ER and high ripple, whereas low values will decrease the shape factor and increase insertion loss. A maximally flat filter shape is derived for the lossless case given in

[2] as $\kappa_1^2 = .125 * \kappa_2^4$. Changing κ_1 and κ_2 from this ideal case allows the ER and IL of the filter to be varied.

Fig. 17(a) shows the calculated drop port transfer function with an ideal coupling ratio, Fig. 17(b) shows the drop port transfer function with a low coupling ratio, and Fig. 17(c) shows the drop port transfer function with a high coupling ratio. In these plots, the frequency dependent filter transmission is relative to a 1550nm center wavelength.

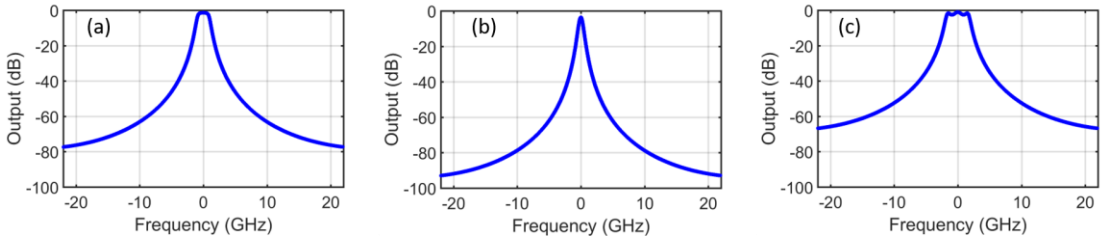

Fig. 17. Calculated drop port functions: (a) shows an ideal coupling ratio filter with κ_2=0.006, yielding SF=0.6, ER=77dB, and IL=1.4dB, (b) shows an under-coupled filter with κ_2=0.001, yielding SF=.26, ER=90, and IL=3.6, (c) shows an over-coupled filter with κ_2=0.01, yielding SF=0.82, ER=67dB, IL=1dB, and ripple =2dB. All filters have a radius of 580µm, κ_1 of 0.15 and loss of 20dB/m.

3.4 Conclusion

In this chapter, the performance of single-bus, dual-bus, and higher-order ring resonators were analyzed. Important figures of merit for ring resonator performance were defined, and their behavior in the different resonator types with varying coupling parameters were explored. Of particular importance to this dissertation, it is notable that the highest Q_l is achieved in single-bus resonators, and the highest power enhancement factor takes place at critical coupling. In addition, higher-order resonators offer much more control of the filter shape, allowing the insertion loss, extinction ratio, and shape factor to be tuned relatively independent of each other, rather than being dependent on a single coupling variable in a first-order resonator.

3.5 References

[1] Chaichuay, Chinda, Preecha P. Yupapin, and Prajak Saeung. “The serially coupled multiple ring resonator filters and Vernier effect.” Opt. Appl 39.1 (2009): 175-194

[2] Rabus, Dominik G. Integrated ring resonators. Springer-Verlag Berlin Heidelberg, 2007.

[3] K. Hiremath and M. Hammer, “Circular Integrated Optical Microresonators: Analytical Methods and Computational Aspects,” in Photonic Microresonator Research and Applications, I. Chremmos, O. Schwelb, and N. Uzunoglu, Eds. New York: Springer, 2010.

[4] B. J. Orr and Y. He, “Rapidly swept continuous-wave cavity-ringdown spectroscopy,” Chem. Phys. Lett., vol. 512, no. 1–3, pp. 1–20, Aug. 2011.

[5] Little, B. E., Chu, S. T., Haus, H. A., Foresi, J., & Laine, J. P. (1997). “Microring resonator channel dropping filters.” Journal of lightwave technology, 15(6), 998-1005.

Chapter 4

High-Extinction Third-Order Resonator Filter

Widely tunable filters with very high extinction ratios, low loss, and flat passbands are important for many applications, including communications, lasers, spectroscopy and nonlinear optics. Examples include separating pump and Stokes signals for Brillouin scattering [1], filtering of idler signals in FWM processes for nonlinear micro-resonators and non-magnetic optical isolation [2], and quantum communications and computing that employ frequency conversion [3]. Traditionally, such filters are made using multi-cavity thin films. However, these filters require over a hundred dielectric layers, a process that is costly and complex and cannot be integrated with other components on a PIC [4]. Additionally, it is difficult to tune these filters over an appreciable range.

Integrated planar waveguide coupled-ring structures can realize filters with reduced cost and fabrication complexity and scaling to larger more complex PIC circuits. To date, multiple-order non-tunable ring filters have been demonstrated with extinction ratios of up to 70dB. Popovíc, Miloš A., et al. [5] and Smith, Henry, et al. [6] demonstrated high-confinement silicon-rich Si_xN_4 third-order ring filters with 50dB and 60dB extinction ratios, respectively, and FSRs up to 2500GHz without the ability to tune. Little presented the largest extinction ratio with integrated ring resonators on an 11^{th}-order filter with asymmetric shape that experimentally demonstrated a symmetric extinction ratio of 50dB and an asymmetric extinction ratio of approximately 70dB [7], including tuning over an unspecified percentage of the FSR.

In this chapter, the design and measurement of third-order ring filters with extinction ratios as high as 80dB, pictured in Fig. 18, are presented. These filters are tunable over 100% of their FSRs using resistive heaters and the thermo-optic effect. Filters using three different ring radii are fabricated with FSRs centered at 50GHz. These different filters are then analytically combined to produce a filter with an FSR of 1250GHz using the Vernier effect.

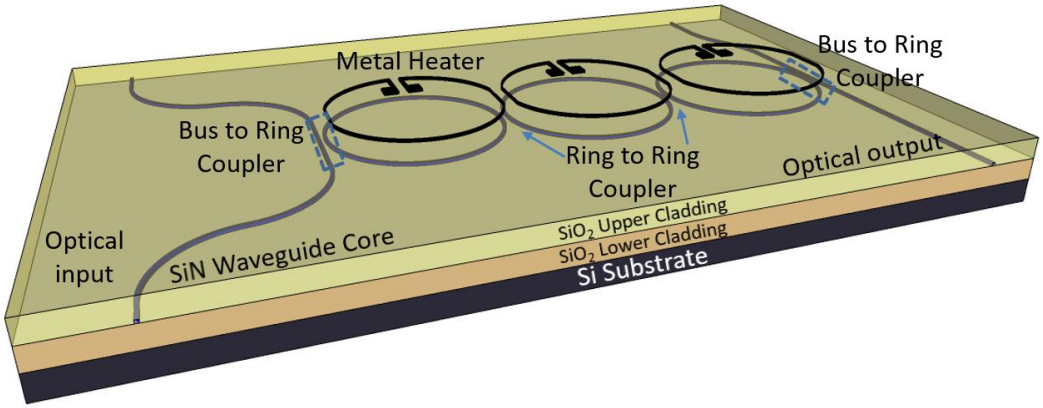

Fig. 18. Depiction of the third-order ring filter with relevant components labeled.

This research was funded by a gift from Keysight Technologies. Doug Baney provided very useful discussions and guidance during the development of these devices. In particular, these discussions gave rise to some of the design goals for the filter, including an extinction ratio exceeding 70dB, an FSR in the 10s of nm, and tunability of 100% of the FSR.

4.1 Design

4.1.1 Waveguide Geometry

For ring resonator filters, the bending limit of the waveguide geometry determines not only the area the filter occupies but also its FSR. Thicker cores allow for tighter bends but also increase the propagation loss (see Section 2.3). Thus, a waveguide was selected that was thick enough to provide a bend limit only as tight as necessary to minimize excess waveguide loss. As a

50GHz FSR is required for an individual ring, a 175nm-thick core was selected, eschewing the traditional ultra-thin nitride cores (see the conclusion of Section 2.5). Radii of 625µm, 580µm, and 530µm were used. The properties of a 625µm resonator are summarized in Fig. 19(a), and a schematic of the waveguide core is shown in Fig. 19(b). Waveguide mode intensity profiles for both the TE and TM modes of the 175nm-thick core design were simulated using FIMMWAVE and the film mode matching technique [8] and are shown in Fig. 20.

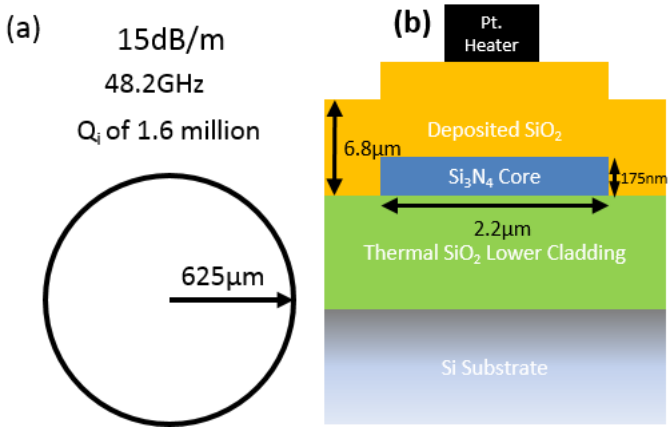

Fig. 19. (a) Typical loss, FSR, and Q for an R=625µm resonator using a 175nm core and (b) schematic of 175nm waveguide.

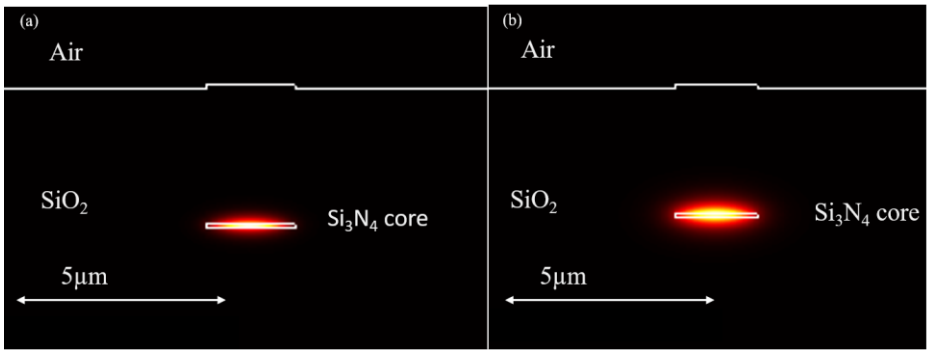

Fig. 20. Simulated mode shapes for both the (a) TE and (b) TM modes for a 175nm-thick and 2.2µm-wide Si_3N_4 waveguide.

A test spiral was fabricated and measured to characterize the chosen waveguide geometry. The propagation loss was measured using a 0.5m spiral test structure and an optical backscatter reflectometer (OBR). For more details on using the OBR for low loss measurements, see Section 2.4. Fig. 21(a) is a TM polarized OBR trace showing reflected power as a function of

propagation distance. Fitting a slope to the trace in Fig. 21(a) yields the waveguide loss, shown in Fig. 21(b) for both TE and TM polarizations. The primary wavelength of interest is 1550nm, with 17 dB/m of loss for the TM mode and 42.5 dB/m of loss for the TE mode. The large difference between the propagation loss for each mode indicates that the interface between core and cladding is rough, causing the TE mode to experience significantly higher scattering losses.

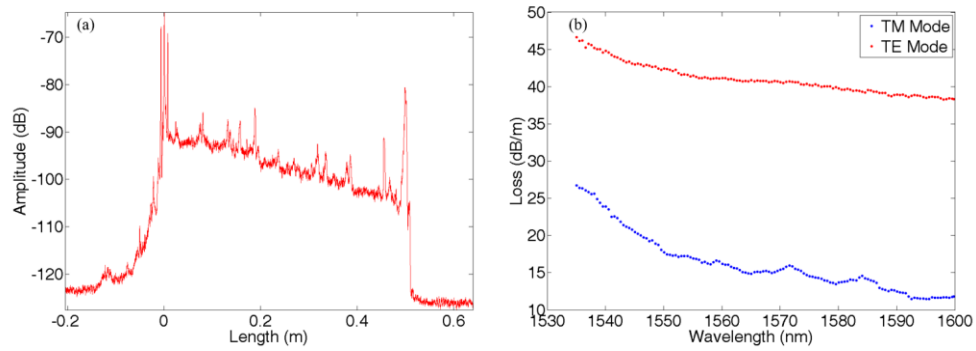

Fig. 21. (a) OBR trace of the 0.5m spiral using 175nm core geometry. (b) The resulting loss fit for both the TE and TM mode. This represents initially high loss for the 175nm core and is improved upon in Fig. 31.

Because the TM mode shows much lower propagation loss, the TM mode was used when designing the rest of the filter, most notably when designing the directional couplers. However, during the development of these devices, the upper cladding deposition technique was changed from a sputter tool to PECVD, and the loss of the TE mode decreased to nearly the same rate as that of the TM mode (see Fig. 31). The filter could be improved using the TE mode, which is discussed in the conclusion.

4.1.2 Coupler Design

Section 3.2 discusses the coupling coefficients of the bus-to-ring and ring-to-ring couplers, κ_1 and κ_2, which have a significant impact on filter performance. The coupling coefficients are determined by the physical parameters of the directional couplers used. In a directional

coupler, two waveguides are brought into proximity such that their modes have a significant overlap, and power can transfer between them. The layout of the directional couplers for both the bus-to-ring couplers and the ring-to-ring couplers are shown in Fig. 22. Rather than depend on simulations of the directional couplers, the accuracy of which is difficult to ensure, test structures were fabricated and measured to determine the relationship between the waveguide gap and the coupling parameter for both ring-to-ring and bus-to-ring couplers.

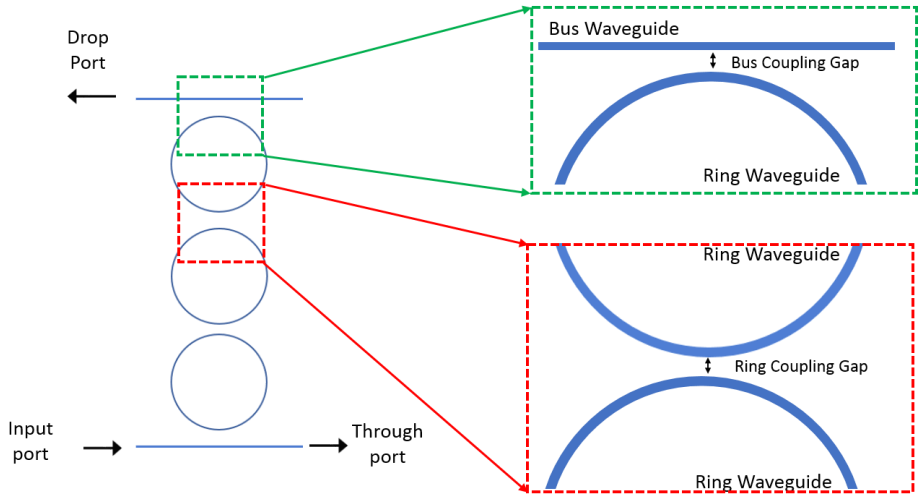

Fig. 22. A depiction of the physical layout of the directional couplers for both the bus-to-bus couplers and the ring-to-ring couplers.

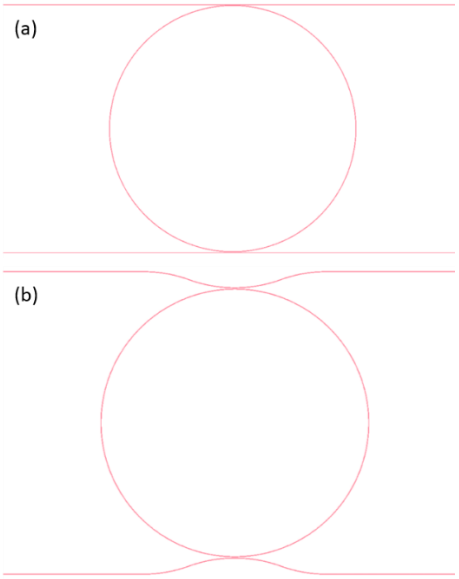

Fig. 23. First-order resonator test structures to measure (a) bus-to-ring coupling and (b) ring-to-ring coupling.

First-order ring filter test structures, shown in Fig. 23, were used to calibrate the coupling coefficients to the physical waveguide gap. The drop port characteristics were measured with a laser wavelength sweep into a photodetector. The resulting filter shape was then fitted to the equation for the drop port transfer function of a first-order ring filter using a least-squares fit, derived in Section 3.1 as per [9], shown in Fig. 24(a). This operation yields the relationship between coupling gap and coupling coefficient, shown in Fig. 24(b) for bus-to-ring coupling and in Fig. 24(c) for ring-to-ring coupling, both for the TM mode.

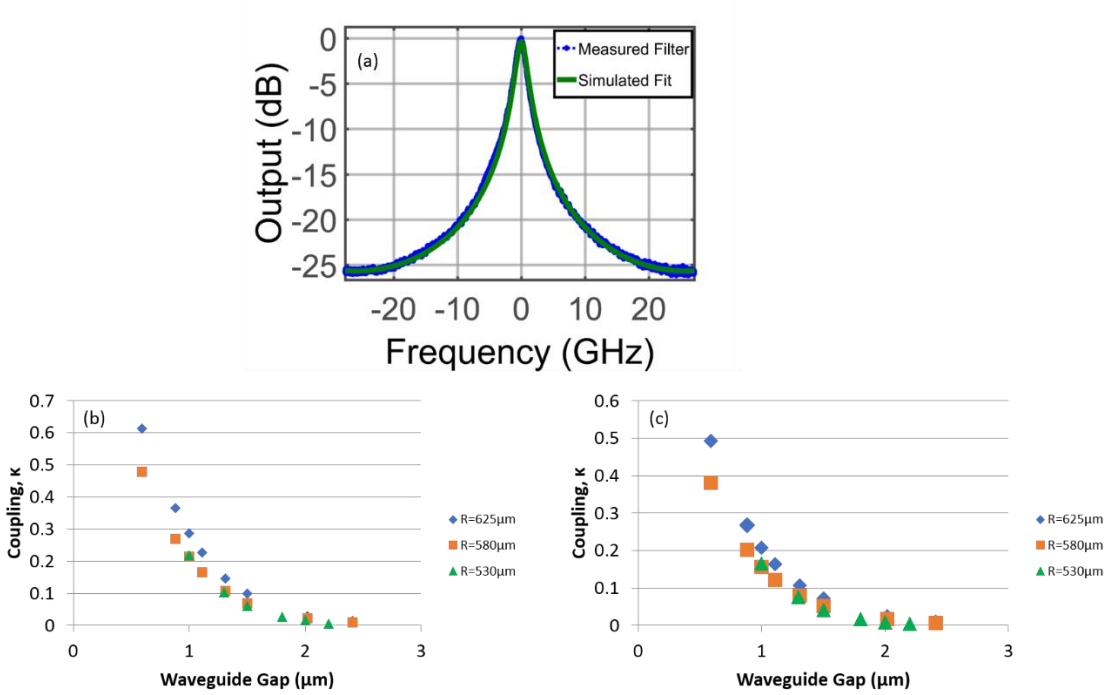

Fig. 24. (a) The analytic fit to a first-order resonator and the measured trend across multiple radii and gaps for the TM mode for (b) bus-to-ring couplers and (c) ring-to-ring couplers.

Because the intensity of light in the guided mode decays exponentially outside of the waveguide core, an exponential dependence between the power coupled and the physical gap between the waveguides can be expected. Additionally, the power coupled is expected to increase with increasing radius, as the waveguides are in close proximity for a longer length. Finally, bus-to-ring couplers should have higher coupling for a given radius and gap, compared to ring-to-ring couplers, as they are also in proximity for a longer length. All three of these trends are observed in the measured data, shown in Fig. 24(b) and (c).

Using Fig. 24(b) and (c), correspondingly, for the bus-to-ring and ring-to-ring coupling values, κ_1 and κ_2, the third-order filter section can be designed using the equation in 3.2. The ratio between κ_1 and κ_2 was chosen for a flat passband. The absolute value was chosen to target an ER of 70dB for the two smaller radii and an ER of 80dB for the largest radii, 625μm. The

physical gap values used on the mask, and the corresponding intended coupling coefficients from Fig. 24(a) and (b), for the third-order rings are summarized in Table 3.

Table 3. Gap values with corresponding predicted kappa values.

Radius (μm)	Bus Gap (μm)	Bus Kappa	Ring Gap (μm)	Ring Kappa
580	1.15	.2	2.4	.01
625	1.39	.13	2.7	.006
530	1.1	.18	2.2	.017

4.1.3 Heater Layer and Upper Cladding Thickness

Si_3N_4 waveguides can be thermally tuned [10] using a resistive metal layer on the upper cladding over the core. Because an absorptive metal layer is being deposited directly over the waveguide, special care must be taken to properly design the thickness of the upper cladding. The upper cladding must be thick enough to prevent the optical mode from overlapping with the metal layer and creating excess loss; however, an excessively thick upper cladding will reduce the power tuning efficiency of the heaters. Using FIMMWAVE, the effect of the upper cladding's thickness on the waveguide loss is simulated, shown in Fig. 25. Modes with upper claddings thicker than 6.5μm will experience negligible loss from the metal layer.

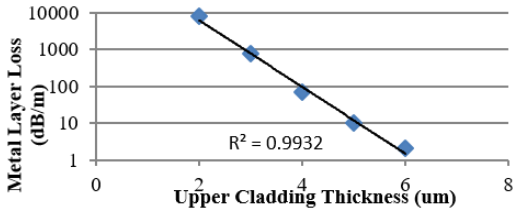

Fig. 25. Metal absorption loss as a function of upper cladding thickness for the TM mode.

4.2 Filter Fabrication

The details of the waveguide fabrication process can be found in Section 2.2; these filters follow this process except as noted here. The upper cladding was initially sputtered; however,

the final device results reported here utilize a PECVD-deposited cladding, using silane as a precursor. In addition, the anneal performed on these devices was limited to 1050°C. Utilizing TEOS as a precursor in the upper cladding deposition and annealing at 1150°C would reduce the waveguide loss further, but these options were not available at the time of fabrication. A simplified schematic of the process flow is pictured in Fig. 26. Specific process values are reported in Table 4.

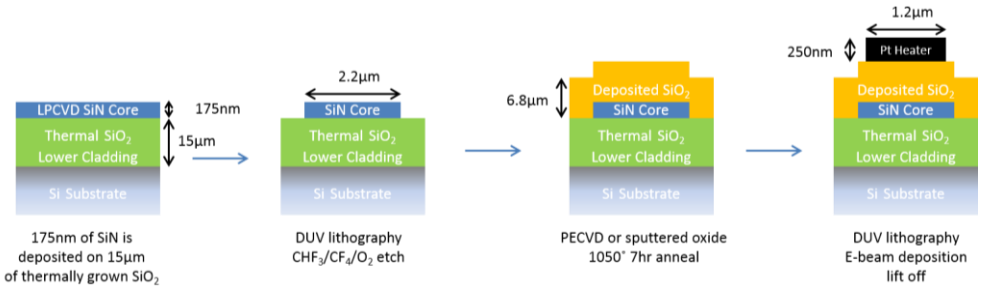

Fig. 26. Cross-section schematic of process flow.

Table 4. Process Parameters.

Parameter	Value
Lower Cladding Thermal SiO_2 Thickness	15µm
Lower Cladding Thermal SiO_2 Index	1.445
SiN Core Thickness	173.9nm
SiN Core Index	1.983
Core Etch Depth	206nm
Upper Cladding PECVD SiO_2 Thickness	6.8µm
Upper Cladding PECVD SiO_2 Index	1.456
Ti Thickness	10nm
Pt Thickness	250nm

The metal heater layer is added using the lift-off technique and the same DUV stepper as the waveguide lithography. It is relevant that a 1mm wafer is used, as a 0.5mm wafer can be rejected from the stepper due to bowing from the thick SiO_2 layer. The metal is deposited using e-beam evaporation. A small 10nm Ti layer is added first for adhesion, and then the 250nm Pt heater itself is added. A waveguide is shown with and without the heater layer in Fig. 27.

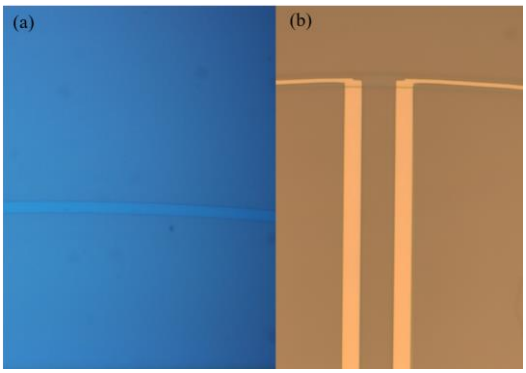

Fig. 27. (a) SiN waveguide with upper cladding deposited. (b) Metal layer deposited over the same waveguide. Approaching the waveguide the metal layer is 5µm wide; over the waveguide it is 1.2µm wide.

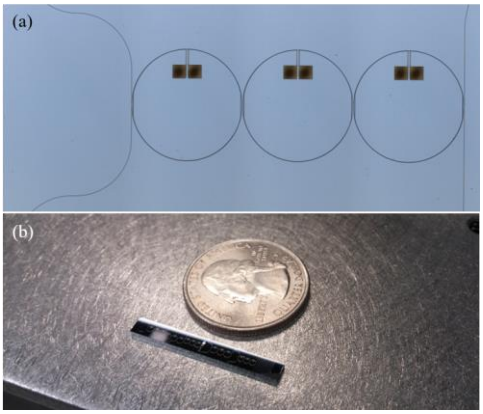

Fig. 28. Images of completed device. (a) shows a micrograph of the third-order filter. (b) shows a bar of 5 third-order filters next to a quarter. The bar is 3.5mm wide.

Fig. 28(b) shows the completed device relative to a quarter. The wafer is diced into 3.5mm-wide columns, each holding five third-order filters. A third-order filter itself is shown in Fig. 28(a). The devices are now complete and can be tested.

4.3 Results

Similar to the first-order rings, the third-order rings are measured by wavelength sweeping a laser through the input port and measuring the drop port. This process is sufficient to measure the passband, as well as to align and tune the rings. However, this technique is not sufficient to measure the stopbands of the ultra-high extinction filters. Because the extinction ratio of

the filters is greater than the extinction ratio of the laser source, the amplified spontaneous emission at the passband wavelength has a higher intensity than the laser in the stopband. This characteristic limits the measurement of the filter to the extinction ratio of the laser.

To enable measurement of the ultra-high extinction ratio, an Agilent 86140B optical spectrum analyzer with a sensitivity of -90 dBm was used to track the laser and reject the ASE light. An erbium-doped fiber amplifier was also used to amplify the signal for optical spectrum analyzer detection. The stage was kept at 20°C using a thermo-electric cooler. A schematic of the measurement is shown in Fig. 29. The physical measurement setup is shown in Fig. 30.

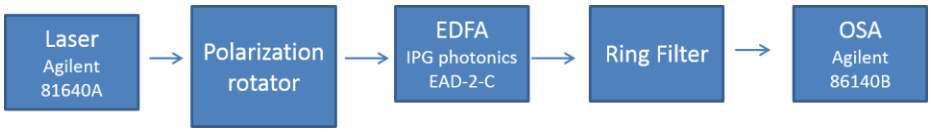

Fig. 29. Schematic representation of measurement setup.

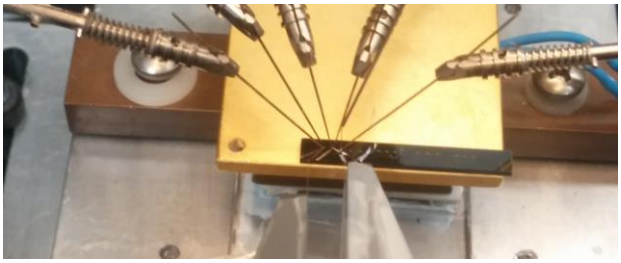

Fig. 30. Photograph of third-order filter being measured.

4.3.1 Waveguide Characterization

A spiral structure, 0.5m in length, was fabricated to measure the propagation losses. Propagation losses were measured using an OBR as described in [11]. Fig. 31(a) is a TM-polarized OBR trace showing reflected power as a function of propagation distance. Fitting a slope to the trace in Fig. 31(a) yields the waveguide loss, shown in Fig. 31(b) for both TE and TM polarizations. The two different modes have nearly the same propagation loss, with a

minimum loss of 9.2dB/m and 10.5dB/m at 1590, and a loss of 15.1dB/m and 17.0dB/m at 1550.

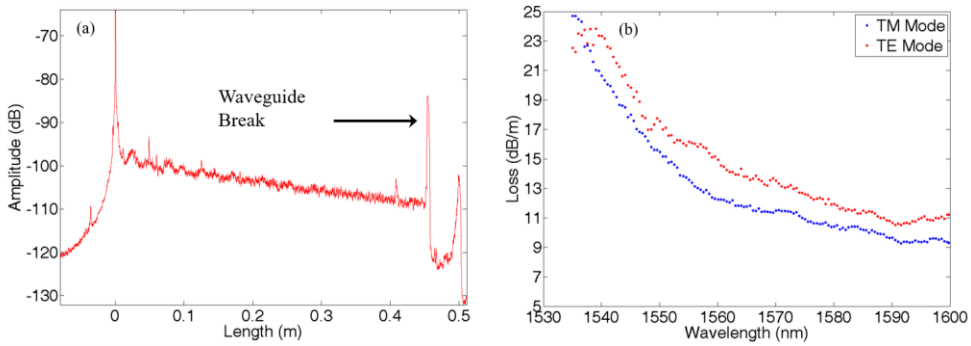

Fig. 31. (a) OBR trace for the TM mode and (b) the resulting loss fit for both modes.

4.3.2 Third-Order Ring Filter Performance

Each ring within the filter is fabricated with an independently controllable platinum heater. Due to small variations in individual rings within the filter, tuning is required to properly align the resonances, as shown in Fig. 32(a), and enables optimization of both the stopband and the passband, as shown in Fig. 32(b). Filter tuning is achieved through small heater changes as the filter transmission is measured, a technique that has been automated for up to fifth-order filters, as reported in [12]. Although the shape factor and ripple can be improved by tuning the rings, the best performance that can be reached is set by the coupling ratio between κ_1 and κ_2, discussed in Section 3.2. Using this aligning technique, device yields greater than 90% across a single wafer were found. Using the heaters to tune the filter over its FSR is described in the following section, 4.3.3.

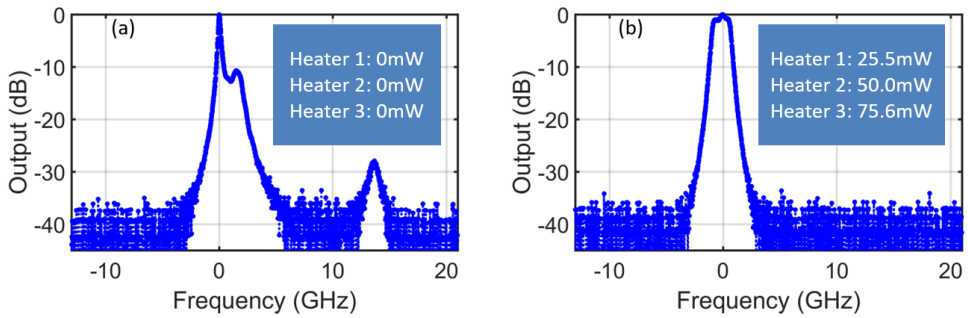

Fig. 32. Wavelength sweeps of third-order filters using the TM mode. The measurement is limited by the photodetector dynamic range. (a) shows a filter initially out of resonance, (b) shows the same filter tuned to resonance.

The measured spectra of the drop port for each radius of the third-order filters are shown in Fig. 33, Fig. 34, and Fig. 35. The spectra are fitted with the analytic transfer function from Section 3.2, and the resulting fit values for the coupling parameters are given in each figure. For the R=625μm filter, the extinction ratio is measured to be 80dB. The fit gives coupling values of κ_1=0.125 and κ_2=0.005, very close to the targeted values of 0.13 and 0.006, respectively. The filter 3dB bandwidth and 20dB bandwidth were measured to be 1.60GHz and 3.12GHz, respectively. The filter input loss was measured using a laser set to the passband of the filter and received by a photodetector. The power loss between the input facet and the detector was first measured, then the average measured coupling loss of 2.4dB per facet was subtracted from that figure. The power measured at the facet was -5.6dBm, and the power at the detector was -11.7dBm. The resulting insertion loss is given in the corresponding figure descriptions.

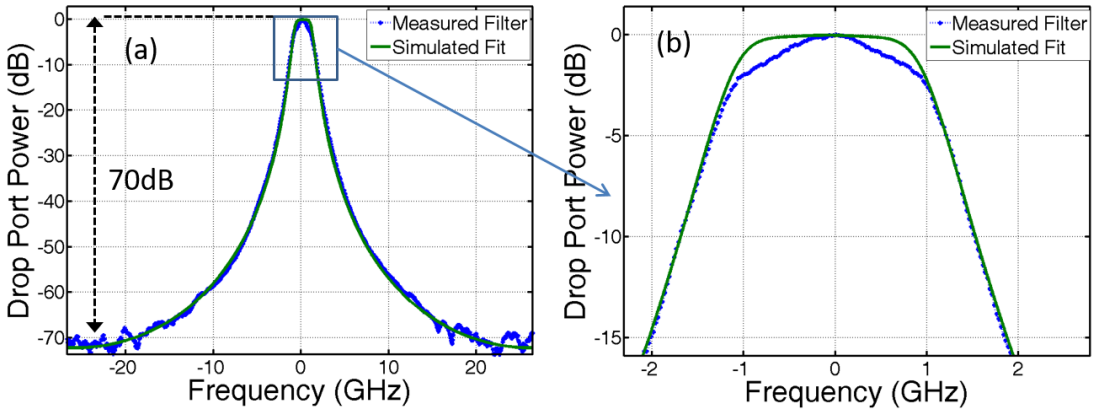

Fig. 33. (a) R=580μm third-order filter function, with an extinction ratio of 70dB and FSR 51.9GHz. The analytical fit yields κ_1 fit=.2, κ_2 fit=.008. (b) R=580μm third-order filter passband with a shape factor of .357, no ripple, and 1.8dB of insertion loss

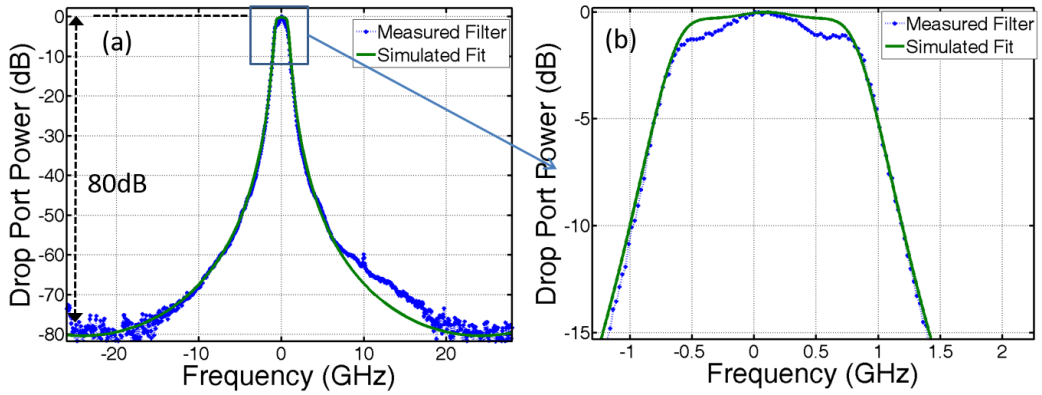

Fig. 34. (a) R=625μm third-order filter function, with an extinction ratio of 80dB and FSR 48.2GHz. The analytical fit yields κ_1 fit=.125, κ_2 fit=.005. (b) R=625μm third-order filter passband with a shape factor of .437, no ripple, and 1.3dB of insertion loss.

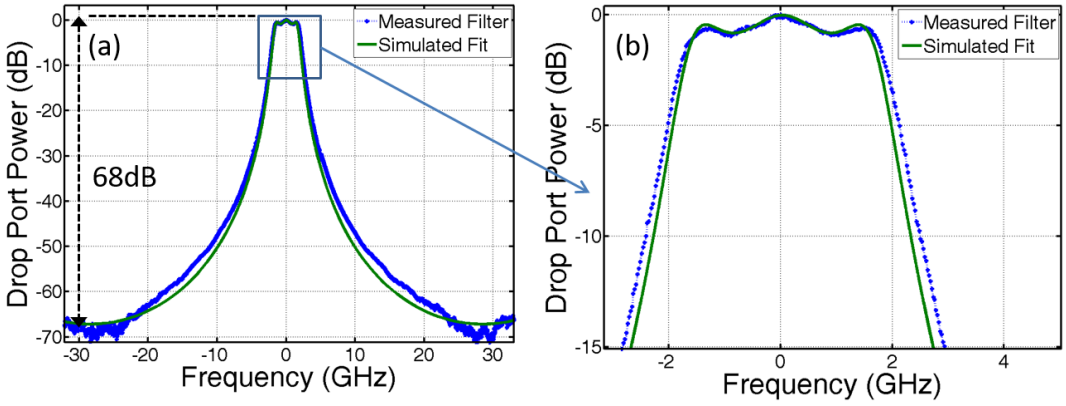

Fig. 35. (a) R=530μm third-order filter function, with an extinction ratio of 68dB and FSR 56.8GHz. The analytical fit yields κ_1 fit=.17, κ_2 fit=.017. (b) R=530μm third-order filter passband with a shape factor of .665, 0.9dB of ripple, and 1.0dB of insertion loss.

The large ripples in the filter function for the smaller radius, R=530μm in Fig. 35(b), indicate that it is over-coupled. The ideal κ_2 value for the filter is 0.006, as opposed to the 0.017 measured value. This value is a result of a mistake in the design of the mask and not of fabrication variation. In Fig. 36, the fitted data is plotted to the ideal coupling case, resulting in a larger extinction ratio and eliminating the ripple entirely.

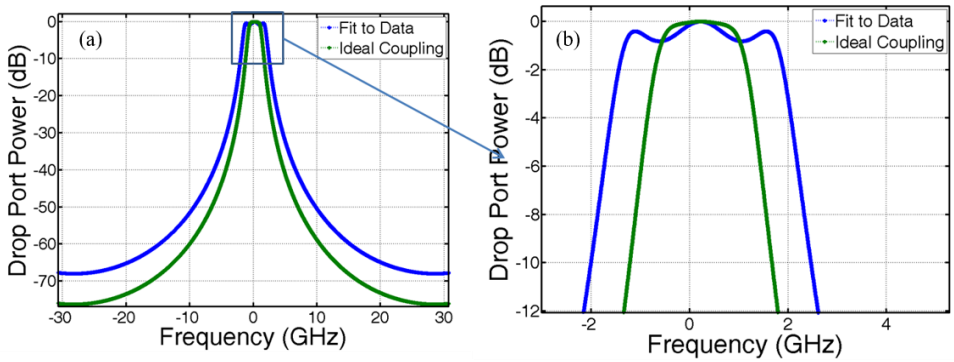

Fig. 36. A comparison between fitted data and ideal coupling data for R=530μm. The ideal coupling yields an extinction ratio of 75dB, shape factor of .584, and 0 ripple. The ideal coupling values are κ 1=.17 and κ 2 =.006. a) reflects the filter shape, while b) reflects the passband.

4.3.3 Filter Tuning and Optical Loss from Metallization

In Section 4.3.2, heaters were used to independently align the rings to realize a third-order filter. If the power dissipated in the heaters is increased uniformly, such that the differences in power between each heater from the alignment are maintained, the filter can be tuned over its full FSR while maintaining the filter shape. Tuning the rings in this manner results in an efficiency of 0.461GHz per mW of power per ring, equivalent to 0.105 W/FSR, shown in Figure 37.

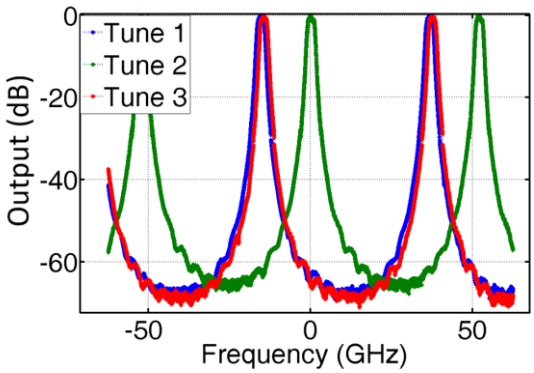

Figure 37. A R=580μm third-order ring filter is tuned over its full FSR. Tune 1 represents no thermal tuning, tune 2 represents 50mW of thermal tuning, and tune 3 represents 110mW of tuning.

The spiral test structure does not include a metal layer, and therefore, the loss measurement does not include any loss incurred by the metal layer. To evaluate losses induced by the metal layer, the losses of two identical first-order rings, one with a metal tuning layer deposited and the other without a metal tuning layer, were compared, as shown in Fig. 38. When the two filter functions are fitted to the theoretical model, the additional loss of the metal layer is found to be 1.7dB/m at 1550nm.

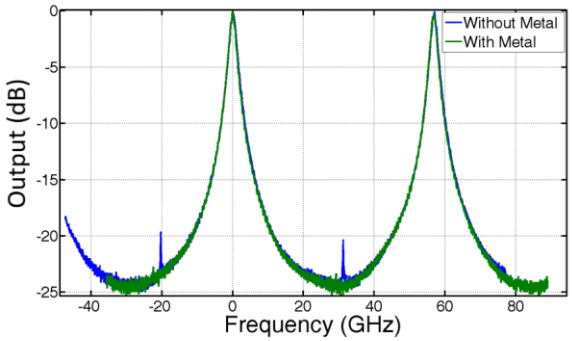

Fig. 38. First-order rings with and without a metal layer are compared. Fitting the two curves to the theoretical model yields an additional loss, due to the metal layer of 1.7dB/m. Other than the unextinguished TE mode resonance present in the curve from the resonator without metal, the plots are essentially indistinguishable to the human eye.

4.3.4 Large FSR Filters

By cascading the output of one triple-ring filter into the input of another with a different radius, the Vernier effect can be utilized to effectively increase the FSR of the drop port. This filter arrangement is shown in Fig. 39. In this figure, drop port 2 represents the Vernier output between the first two filters, and drop port 3 represents the Vernier output between all 3 filters. The radii used were chosen to produce a 10nm resultant FSR. The output of this arrangement can be simulated by summing the outputs (in dB) of each separate filter. This simulation is shown in Fig. 40, for the fitted data to each ring, as well as the ideally coupled case for the smallest ring radius.

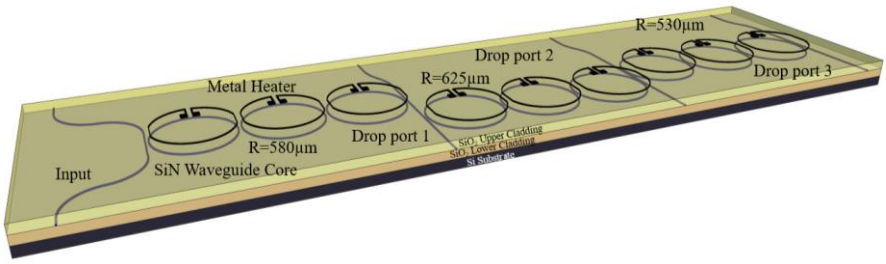

Fig. 39. Cascaded Vernier design for enhanced free spectral range and tuning.

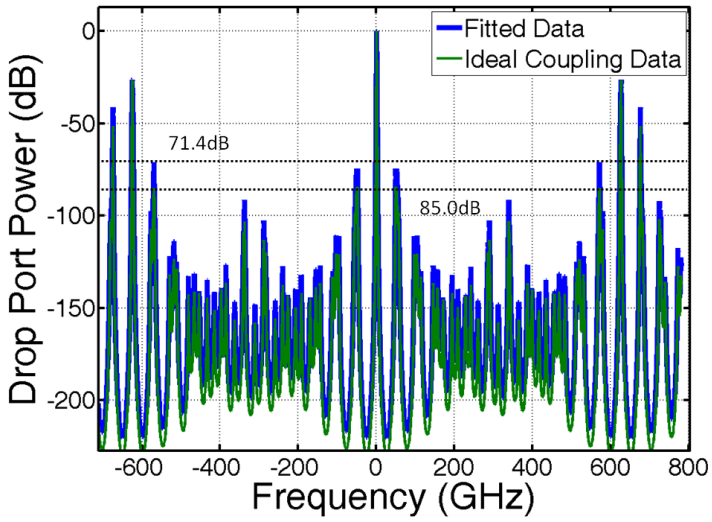

Fig. 40. Calculated Vernier filter function resulting from cascading the third-order filters of all three radii. Both the original fit for the smallest radius and the corrected fit are shown. The filter has an

effective FSR of 1251GHz (10nm). Original Fit: Shape Factor=.525, Extinction Ratio=71.4. Ideal Fit: Shape Factor=.628, Extinction Ratio=85.0.

The resulting Vernier filter function has an effective FSR of 1251GHz. The filter has an extinction ratio greater than 70dB for the over-coupled smallest radius and an extinction ratio of 85 for the ideally coupled case. This filter can be tuned over its entire FSR, but not continuously.

4.4 Conclusion

In this chapter, the design and demonstration of tunable third-order high-extinction ratio filters were presented. The largest measured extinction ratio, 80dB, represents a 20dB improvement over any reported filter of the sixth order or lower. In addition, an extinction ratio was measured in this work greater than the largest reported for a resonator filter, of 70dB using an eleventh-order filter [7].

These filters utilize the TM mode of the Si_3N_4 ULLW platform, due to initial results yielding high TE mode loss. With different fabrication techniques, the TE and TM mode experience comparable loss, and the filter could be improved by utilizing the TE mode. This mode would result in a bend radius of 300μm or less, reducing the area of the filter by a factor of 4 and increasing the FSR by a factor of 2, without affecting performance. In addition, these filters use electrical resistive heaters to tune the resonators, which require substantial power to use over an FSR and cannot be modulated quickly. Future efforts on the ULLW platform should involve developing alternative tuning methods, particularly for faster and lower power tuning. Strain-based index modulation already has some promising initial results that can be readily employed in tuning these third-order filters [13][14] [15]. This process is discussed more thoroughly in Chapter 8.

4.5 References

[1] Kittlaus, Eric A., Heedeuk Shin, and Peter T. Rakich. “Large Brillouin amplification in silicon.” Nature Photonics (2016).

[2] Hua, Shiyue, Jianming Wen, Xiaoshun Jiang, Qian Hua, Liang Jiang, and Min Xiao, “Demonstration of a chip-based optical isolator with parametric amplification,” Nature Communications | 7:13657 | DOI: 10.1038/Ncomms13657.

[3] Silverstone, Joshua W., Bonneau D, Ohira K, Suzuki N, Yoshida H, Iizuka N, Ezaki M, Natarajan CM, Tanner MG, Hadfield RH, Zwiller V. “On-chip quantum interference between silicon photon-pair sources.” Nature Photonics 8.2 (2014): 104-108.

[4] Macleod, H. Angus. Thin-film optical filters. CRC press, 2001.

[5] Popovíc, Miloš A., Tymon Barwicz, Michael R. Watts, Peter T. Rakich, Luciano Socci, Erich P. Ippen, Franz X. Kärtner, and Henry I. Smith. “Multistage high-order microring-resonator add-drop filters.” Optics Letters 31.17 (2006): 2571-2573.

[6] Smith, Henry, Tymon Barwicz, Charles W. Holzwarth, Milos A. Popovic, Michael R. Watts, Peter T. Rakich, Minghao Qi, Raul Barreto, Franz X. Kärtner, and Erich P. Ippen. “Strategies for fabricating strong-confinement microring filters and circuits.” Optical Fiber Communication Conference. Optical Society of America, 2007.

[7] Little, B. E., Chu, S.T., Absil, P.P., Hryniewicz, J.V., Johnson, F.G., Seiferth, F., Gill, D., Van, V., King, O. and Trakalo, M. “Very high-order microring resonator filters for WDM applications.” IEEE Photonics Technology Letters 16.10 (2004): 2263-2265.

[8] Sudbo, A. Sv. “Film mode matching: a versatile numerical method for vector mode field calculations in dielectric waveguides.” Pure and Applied Optics: Journal of the European Optical Society Part A 2.3 (1993): 211

[9] Chaichuay, Chinda, Preecha P. Yupapin, and Prajak Saeung. “The serially coupled multiple ring resonator filters and Vernier effect.” Opt. Appl 39.1 (2009): 175-194

[10] Amatya, Reja, Charles W. Holzwarth, M. A. Popovic, F. Gan, H. I. Smith, F. Kartner, and R. J. Ram. “Low power thermal tuning of second-order microring resonators.” Conference on Lasers and Electro-Optics. Optical Society of America, 2007

[11] Jared F Bauters, Martijn JR Heck, Demis John, Daoxin Dai, Ming-Chun Tien, Jonathon S. Barton, Arne Leinse, René G. Heideman, Daniel J. Blumenthal, and John E. Bowers. “Ultra-low-loss high-aspect-ratio Si 3 N 4 waveguides.” Optics express 19, no. 4 (2011): 3163-3174

[12] Mak, J. C., Sacher, W. D., Xue, T., Mikkelsen, J. C., Yong, Z., & Poon, J. K. (2015). "Automatic resonance alignment of high-order microring filters." IEEE Journal of Quantum Electronics, 51(11), 1-11

[13] Hosseini, Naser, Ronald Dekker, Marcel Hoekman, Matthijn Dekkers, Jan Bos, Arne Leinse, and Rene Heideman. "Stress-optic modulator in TriPleX platform using a piezoelectric lead zirconate titanate (PZT) thin film." Optics express 23, no. 11 (2015): 14018-14026

[14] Jin, W., E. J. Stanton, N. Volet, R. G. Polcawich, D. Baney, P. Morton, and J. E. Bowers. "Piezoelectric tuning of a suspended silicon nitride ring resonator." In *Photonics Conference (IPC), 2017 IEEE*, pp. 117-118. IEEE, 2017.

[15] W. Jin, R. G. Polcawich, P. Morton, and J. Bowers, "A piezoelectrically tuned suspended silicon nitride ring resonator via PZT thin film actuator, Optics Express, 26, p. 3124 (2018).

Chapter 5

High-Q Large Mode Volume Resonator

Low-loss resonators with sharp resonances and high cavity enhancement factors, evaluated by the Q figure of merit, have a wide range of applications, including microwave photonics [1], non-linear optics [2], and sensing [3]. Reaching high Qs on the order of tens of millions requires resonators with very low propagation loss, which is enabled by the Si_3N_4 waveguide system. Thin, weakly guiding cores have the capability to reach losses as low as 0.045dB/m [4] and additionally provide a dilute optical mode that can support very high optical intensities without unintentionally inducing non-linearities [5].

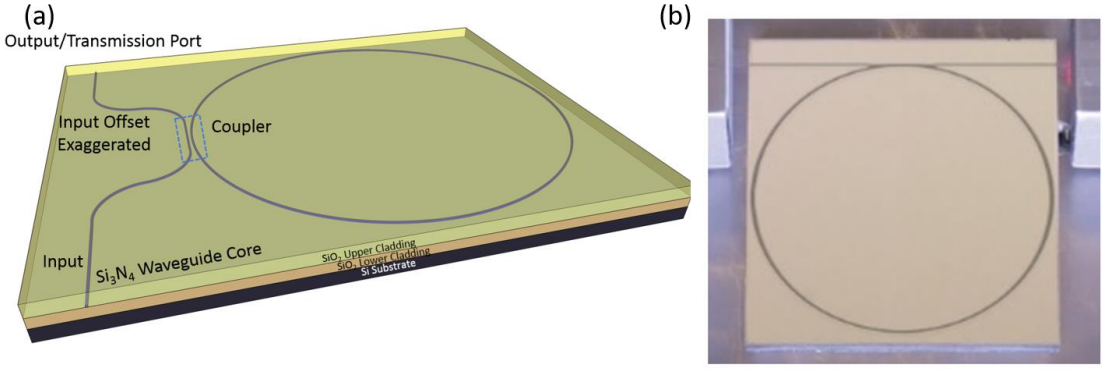

Fig. 41. (a) Depiction of the high-Q large mode volume resonator design. (b) Optical photograph of a fabricated resonator.

Previous high-Q resonators within the Si_3N_4 waveguide system have been demonstrated with loaded Q_l as high as 42 million [6], corresponding to a waveguide loss of 0.32dB/m. These resonators utilized a bonded thermal oxide upper cladding for symmetric, hydrogen-free claddings. However, as with the other devices in this dissertation, this work utilizes a deposited

cladding to allow flexible, complex photonic integration with previously demonstrated components.

In this chapter, the design and measurement of integrated high-Q large mode volume resonators, pictured in Fig. 41(a) and (b), are presented. These resonators have an intrinsic Q_i greater than 60 million and a Q exceeding 28 million, and they utilize a single-bus design to minimize coupling losses. The resonators presented are specifically designed to be used as Brillouin lasers. The considerations in design for Brillouin lasing are included in the present work; however, the measurement and evaluation of the resonators as Brillouin lasers are beyond the scope of this dissertation. More detail, including threshold and efficiency measurements, can be found in [7]. This material is based upon work supported by the Defense Advanced Research Projects Agency (DARPA) and Space and Naval Warfare Systems Center Pacific (SSC Pacific) under Contract No. N66001-16-C-4017.

5.1 Resonator Design for SBS Lasing

A resonator forms a cavity remarkably analogous to a Fabry-Perot (FP) cavity, with the power transmitted from the resonator corresponding to the power escaping from the mirrors in the case of an FP. The design in this work utilizes a single bus to couple into the resonator to increase the loaded Q and power buildup within the resonator. When analyzing the resonator as a lasing medium, the laser gain is based on light-sound interactions resulting from two counter-propagating waves within the resonator [8]. The two waves, the pump and Stokes line, are mediated by a traveling wave acoustic grating. The resulting Brillouin gain is offset from the pump, dependent upon the non-linear material properties of the waveguide. Efficient transfer of energy between the pump and Stokes frequencies requires that longitudinal modes within the resonator align to both the pump and the Brillouin gain offset, depicted in Fig. 42.

The FSR is determined by the optical length of the cavity, and thus requires careful measurement of the group index of the waveguides and choice of resonator path length.

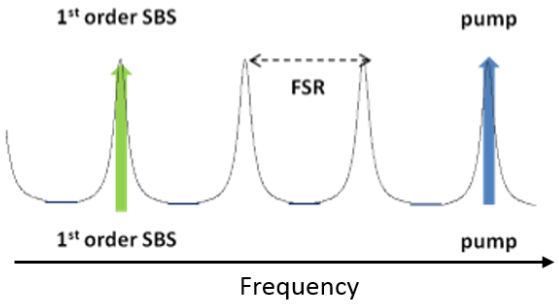

Fig. 42. FSR and gain offset matching required for efficient SBS lasing.

The gain is dependent on the intensity of the pump within the resonator. Because the enhancement of power within the resonator increases with the Q_l of the resonator, low on-chip pumping thresholds for SBS lasing can be achieved by using an ultra-high-Q resonator design, while also reducing the laser phase noise and hence linewidth. It is worth noting, however, that, similar to increasing the reflectivity of the mirrors in a FP laser, increasing the Q can decrease the laser emission intensity and wall-plug efficiency.

5.1.1 Waveguide Geometry

The waveguide geometry determines the propagation loss and bending radius, discussed in detail in Section 2.3, but also governs the group index and Brillouin gain offset, as it determines the mode shape and overlaps with core and cladding materials. The primary consideration when choosing the waveguide geometry is to reach the highest Q_l resonator. The Q_l, from Section 3.1, is described as:

$$Q_l = \omega \frac{T_{rt}}{L}$$

Where ω is the angular frequency of the resonating light, T_{rt} is the round-trip time of the resonator, and L is the fractional power loss of the resonator per round trip. This equation of

the Q of the cavity can describe the loaded Q_l of the cavity by including coupling loss in the variable L, and the intrinsic Q_i by excluding the coupling loss. Thus, choosing the waveguide geometry to minimize loss will yield the highest Qs, which makes the thinner, higher aspect ratio geometries preferable, referring to the conclusions regarding core thickness from Section 2.5. In addition, larger path length resonators increase the round-trip time, yielding higher Qs, and produce a higher total mode volume. These factors make the thinner cores, which have very large bend radii, even more attractive. In this work, a 40nm waveguide core is utilized. Fig. 43(a) summarizes the loss, FSR and Q_i of a typical resonator using a 40nm core, while Fig. 43(b) shows the waveguide schematic. Waveguide mode intensity profiles for the TE mode of the 40nm-thick core design were simulated using FIMMWAVE and the film mode matching technique [8] and are shown in Fig. 44.

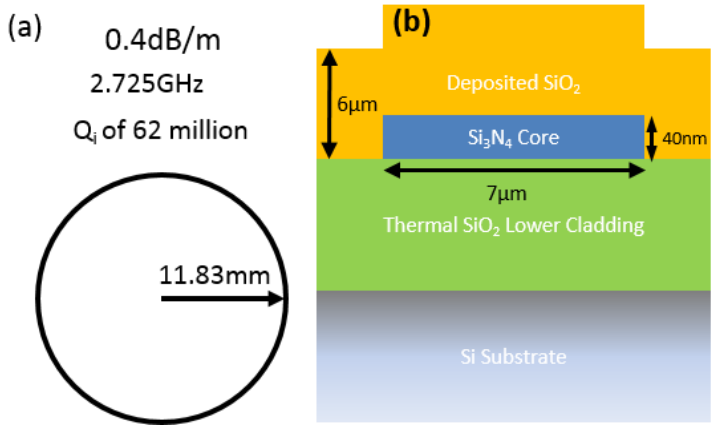

Fig. 43. (a) Typical loss, FSR, and Q for an R=11.83mm resonator using a 40nm core and (b) schematic of 175nm waveguide.

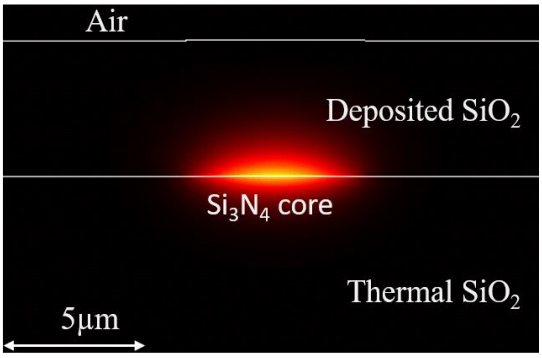

Fig. 44. Simulated TE mode shape for a 40nm x 7µm Si_3N_4 waveguide.

Many aspects of the design of the resonator tie directly into the performance of the selected waveguide geometry. The coupling into the waveguide must be chosen to maximize the buildup of energy within the resonator, known as critical coupling, which is dependent upon the round-trip loss of the resonator (see Section 3.2). In addition, both the pump signal and the Brillouin gain offset must align with the wavelength condition of the resonator, requiring us to match the optical length of the resonator with this gain offset. The optical length of the resonator depends on both the group index of the waveguide geometry, which must be precisely measured, and the physical length of the ring. The Brillouin gain offset in fibers has been studied thoroughly; however, the variety of Si_3N_4 waveguide geometries means there are also a variety of different gain offsets, none of which have been characterized. The mode overlap with the cladding, as well as the deposition technique used in the cladding, can vary this offset. Thus, the Brillouin gain offset of the specific waveguide design must also be accurately measured.

5.1.2 Measuring Loss, Group Index, and Gain Offset

The loss, group index, and gain offset can be directly measured from a sufficiently long waveguide of known length. The loss and group index can be measured using an OBR [9],

whereas the Brillouin gain offset can be measured using the pump/probe technique. To this end, a 5-meter spiral was fabricated. The waveguide mask layer is shown in Fig. 45.

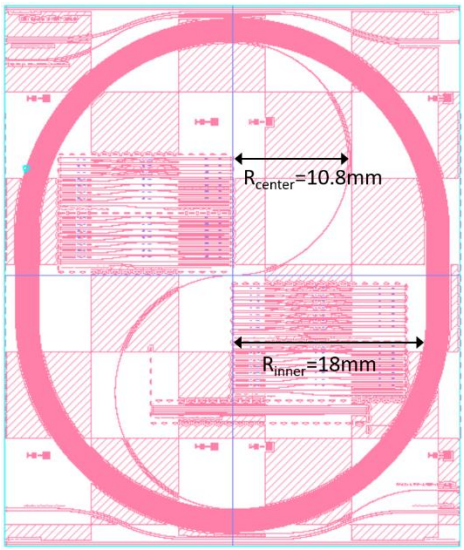

Fig. 45. Waveguide mask layer. The blue lines indicate the division between multiple masks stitched together.

The smallest bend radius in the spiral is at the center, which, in the case of a circular spiral, is half of the radius of the innermost turn of the spiral. The smallest radius in the center of this design must be larger than the critical bend radius of 10mm, and therefore the innermost turn of the spiral must be at least 40mm in diameter, and the outer diameter even larger. The DUV stepper used to make this device has a die size of 21mm x 25mm. In order to fit a spiral with a diameter greater than 40mm, the waveguides across multiple die must be connected using waveguide stitching. This process and its impact on loss is given in detail in Section 6.2.3. The actual values deviate from the circular calculation, due to using an elliptical spiral. The specific radii used in this design are 10.8mm for the center radius and 18mm for the innermost spiral radius.

The waveguide spiral was measured using an OBR. The OBR trace and resulting loss fit are shown in Fig. 46. The wavelength of interest for resonance is 1550nm, giving a loss value

of 0.6dB/m to use for resonator design. In addition, fitting the group index to the measured spiral length gives a value of n_g=1.478. This value is consistent across four measured devices.

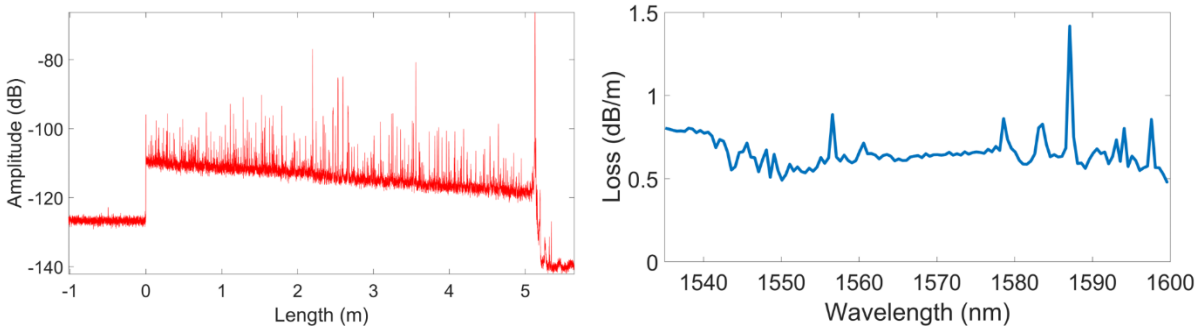

Fig. 46. (a) OBR trace of 5-meter spiral and (b) waveguide loss fit.

The gain profile of the waveguide is measured using the pump/probe technique. A pump laser is input in one facet of the spiral, and a probe is input in the other facet, propagating counter to the pump. This probe is swept across different wavelengths, and the gain provided by the pumped waveguide is measured against wavelength. The measured gain peak is 10.93GHz. More details on this measurement and its result can be found in [7].

5.1.3 Resonator Design

Having measured the loss and group index, a critically coupled resonator with FSR matched to the gain offset can then be targeted. In order for both the pump laser and Brillouin gain offset to resonate, the offset must be an integer multiple of the FSR of the resonator. Given the current project's bend radii limit, the FSR was selected to be one-fourth of the Brillouin shift. Two resonator lengths were chosen to target the center of the gain shift and the gain peak, of 74.3mm and 74.1mm, corresponding to FSRs of 2.728GHz = (10.91GHz)/4 and 2.732GHz = (10.93GHz)/4, respectively. These FSRs were obtained using the relationship given in Section 3.1, using the measured group index value of 1.478.

The resonator was expected to perform best near critical coupling, as that results in the largest buildup of power within the resonator. This value corresponds to just under 0.5% power coupling for the measured loss value of 0.6dB/m and a resonator of 74.1mm in length. Depending on the waveguide loss, there is a different coupling ratio that yields the lowest threshold power. In the present work, two different coupling values were fabricated for the cases in which different loss values were fabricated. Coupling values of 0.5% and 0.25% were targeted, ideal for losses of 0.6dB/m and 0.3dB/m.

The physical gap for the waveguide coupler must be calibrated to reach these coupling targets. In Chapter 3, test structures and a variety of splits were utilized to calibrate the coupler and gap relationship for the work presented in that Chapter. However, because these ring structures are so large, it would require a prohibitive number of wafers and fabrication cycles to perform such an experiment. Instead, therefore, the current project relied on simulation. The coupling gap between the bus and the resonator waveguide of the directional coupler was determined through simulation using PhoeniX Software's Optodesigner. The modes of the bus and resonator were simulated using film mode matching. The coupling was then calculated using coupled mode theory [10]. The couplers' dependence on the gap is plotted in Fig. 47.

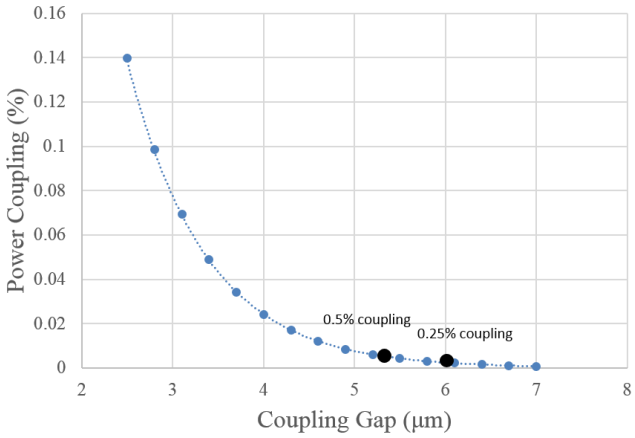

Fig. 47. Resonator coupling and waveguide simulated relationship.

As expected for evanescently coupled waveguides, there is an exponential relationship between the coupling and the waveguide gap. Waveguide gaps of 5.42μm and 6μm were chosen for the target coupling values of 0.5% and 0.25%, respectively.

5.2 Resonator Fabrication

The two types of resonators were fabricated using improved techniques compared to some other devices within this dissertation. Most notably, the upper cladding was deposited using a TEOS-based PECVD, made available by Honeywell. In addition, they allowed use of their furnace, which increased the maximum available anneal temperature to 1150°C. A complete summary of the fabrication process can be found in Section 2.2.

5.3 Resonator Characterization

The resonators were characterized by Catia Pinho, Grant Brodnik, and Sarat Gundavarapu. High-Q resonators require an optical frequency standard to measure accurately [11]; in this case, an unbalanced Mach-Zehnder interferometer (MZI) was used with a 1MHz FSR that is comparable to the FWHM of the resonator under test. The MZI was calibrated using an SSB, or swept-source measurement [12].

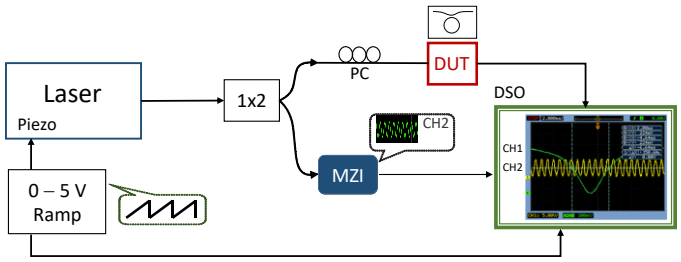

Fig. 48. Calibrated MZI measurement setup to measure high-Q resonators. The swept optical signal is transmitted through both the frequency standard and the resonator simultaneously.

The resonator was measured using a fiber laser with piezo frequency tuning. The laser was transmitted through both the MZI frequency standard and the resonator under test; the

measurement setup is illustrated in Fig. 48. The resulting spectrum, shown in Fig. 49 for a resonator designed for 0.25% coupling, was fitted with a Lorentzian fit to extract the resonator coupling and propagation loss.

$$T = \frac{a^2 - 2racos\phi + r^2}{1 - 2arcos\phi + (ra)^2}$$

Here a is the round-trip loss, r is the transmission coefficient, and ϕ is the round-trip phase change. r can be used to calculate the coupling coefficient by $\kappa^2 = 1 - r^2$ in the absence of significant coupling loss. The loss coefficient a is related to the propagation loss by $\alpha = -log(a^2)L^{-1}$.

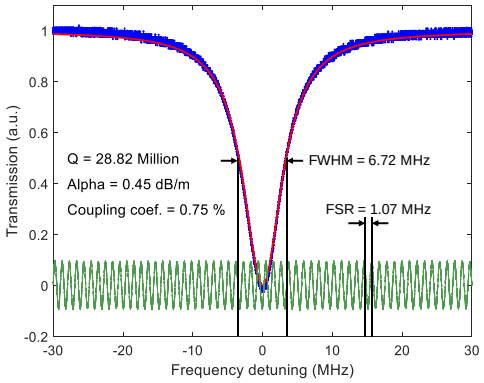

Fig. 49. Resonator measurement with Lorentzian fit.

Additional resonator measurements are summarized below in Table 5. Resonators with couplers simulated for 0.5% are designated "A," while those designed for 0.25% are designated "B."

Table 5. Summary of Q measurements for L=74.1mm (L=11.83mm).

Sample	Q_l (million)	FHWM (MHz)	Loss (dB/m)	Coup. Coef. (%)	Q_i (million)
A1	21.45	9.02	0.59	1.04	44.32
A2	23.55	8.22	0.42	1.14	61.95
B1	28.10	6.89	0.52	0.68	50.38
B2	28.82	6.72	0.45	0.75	57.59

The fitted coupling parameters are substantially higher than the simulated coupling, which is not unexpected as the coupling simulations for dilute modes are rarely accurate. The larger resonators, with a path length of 74.3mm, did not perform as well as lasers but had similar Q_l ranging from 20 to 30 million.

The resonator performs successfully as a Brillouin laser. When pumped with large input powers (>400mW), up to 10 cascading Stokes orders are observed. Details of the measurements and results can be found in [7].

5.4 Conclusion

In this chapter, the design and measurement of a high-Q large mode volume resonator, designed for Brillouin lasing, was presented, with Q_i values exceeding 60 million. This resonator can serve as a precise reference for sensing and metrology, while the laser capacity sets forth a route to compact, high-coherence, low-noise, low-cost lasers. In addition, the waveguide system used has previously demonstrated active and passive components that can be integrated with the resonator for more complex functions.

Integral to the functionality of the resonator as a laser is the careful selection of the resonator radius, based on group index measurements, to match the FSR to the gain offset. Additionally, the bus coupling into the resonator must be balanced with the round-trip loss to allow for high power enhancement within the resonator. Development of this process in a foundry would allow for reproducible control over both of these parameters.

5.5 References

[1] Ilchenko, Vladimir S., and Andrey B. Matsko. "Optical resonators with whispering-gallery modes-part II: applications." *IEEE Journal of selected topics in quantum electronics* 12.1 (2006): 15-32

[2] Xuan, Yi, Yang Liu, Leo T. Varghese, Andrew J. Metcalf, Xiaoxiao Xue, Pei-Hsun Wang, Kyunghun Han et al. "High-Q silicon nitride microresonators exhibiting low-power frequency comb initiation." *Optica* 3, no. 11 (2016): 1171-1180.

[3] Li, Jiang, Myoung-Gyun Suh, and Kerry Vahala. "Microresonator Brillouin gyroscope." *Optica* 4, no. 3 (2017): 346-348.

[4] Bauters, Jared F., Martijn JR Heck, Demis D. John, Jonathon S. Barton, Christiaan M. Bruinink, Arne Leinse, René G. Heideman, Daniel J. Blumenthal, and John E. Bowers. "Planar waveguides with less than 0.1 dB/m propagation loss fabricated with wafer bonding." *Optics Express* 19, no. 24 (2011): 24090-24101.

[5] Tien, M.-C., Bauters, J. F., Heck, M. J. R., Blumenthal, D. J. & Bowers, J. E. "Ultra-low loss Si3N4 waveguides with low nonlinearity and high power handling capability." Opt. Express 18, 23562–23568 (2010).

[6] Spencer, Daryl T., Jared F. Bauters, Martijn JR Heck, and John E. Bowers. "Integrated waveguide coupled Si3N4 resonators in the ultrahigh-Q regime." *Optica* 1, no. 3 (2014): 153-157.

[7] S. Gundavarapu, M. Puckett, T. Huffman, R. Behounin, J. Wu, T. Qiu, G. Brodnik, C. Pinho, D. Bose, P. Rakich, J. Nohava, K. Nelson, M. Salit, D. Blumenthal, "Integrated Waveguide Brillouin Laser", arXiv:1709.04512 [physics.optics].

[8] Qiu, W. et al. "Stimulated Brillouin scattering in nanoscale silicon step-index waveguides: a general framework of selection rules and calculating SBS gain." Opt. Express 21, 31402 (2013).

[9] Jared F Bauters, Martijn JR Heck, Demis John, Daoxin Dai, Ming-Chun Tien, Jonathon S. Barton, Arne Leinse, René G. Heideman, Daniel J. Blumenthal, and John E. Bowers. "Ultra-low-loss high-aspect-ratio Si 3 N 4 waveguides." Optics express 19, no. 4 (2011): 3163-3174.

[10] Stoffer, Remco, Kirankumar R. Hiremath, Manfred Hammer, Ladislav Prkna, and Jiří Čtyroký. "Cylindrical integrated optical microresonators: Modeling by 3-D vectorial coupled mode theory." Optics Communications 256, no. 1 (2005): 46-67.

[11] Li, Jiang, Hansuek Lee, Ki Youl Yang, and Kerry J. Vahala. "Sideband spectroscopy and dispersion measurement in microcavities." Optics express 20, no. 24 (2012): 26337-26344.

[12] Wei, Tao, Jie Huang, Xinwei Lan, Qun Han, and Hai Xiao. “Optical fiber sensor based on a radio frequency Mach–Zehnder interferometer.” Optics letters 37, no. 4 (2012): 647-649.

Chapter 6

Integrated Coils for Optical Gyroscopes

Gyroscopes are useful in a wide range of applications, including conventional navigation, control of autonomous vehicles, and geographical surveying and mapping. Interferometric optical gyroscopes (IOGs), principally fiber optical gyroscopes (FOGs), demonstrate high performance standards beyond the most advanced MEMs (Microelectromechanical systems) gyroscopes. However, their cost, power dissipation, and size are comparatively large. Si_3N_4 waveguides, particularly the high aspect-ratio, low-loss waveguides, have the capacity to not only improve performance and manufacturability but also to decrease the size, power, weight, and cost of interferometric gyroscopes.

To date, waveguide optical gyroscopes (WOGs) have been designed surrounding the use of resonant ring waveguides (RMOGs, resonant micro-optic gyroscopes) to amplify their sensitivities. Because they are a chip-scale device, they surpass FOGs in terms of cost and size. However, they are limited in sensitivity, most noticeably at low rotation rates. For RMOGs that have an active component, this limitation comes from the lock-in effect. Below a certain rotational threshold, feedback between the two counter-propagating signals within an RMOG can lock their phase together. Because the rotational information is measured from the phase difference between the two signals, this eliminates the rotational signal and creates a floor for the RMOG's sensitivity. In passive RMOGs, coherent feedback from scatterers, facets, or even sidewalls reduces the sensitivity [1]. This sensitivity reduction can be

eliminated by using sources with more spectral width, such as ASE (amplified spontaneous emission) or even a swept laser source [2][3]; however, these methods are not compatible with a resonator, as they naturally select narrow portions of the source.

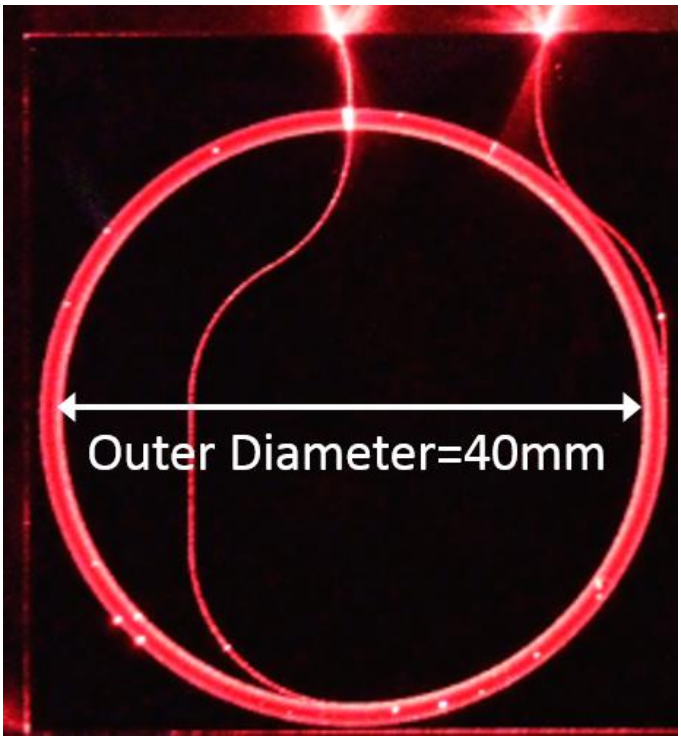

Fig. 50. Fabricated 3-meter gyroscope coil illuminated with two red lasers (λ=650nm).

In this chapter, the modeling, design, testing, and evaluation of large-area delay-based waveguide gyroscopes, shown in Fig. 50, are presented. This design leverages the cost and size benefits of a chip-scale device without any inherent limitation in sensitivity. The large-area coil utilizes low-loss waveguide stitching to reach an outer diameter of 40mm in order to leverage lower-loss waveguide geometries. A fully integrated WOG requires a passive low-loss Si_3N_4 waveguide coil and an active section including optical sources, detectors, and modulators. These active and passive components can be integrated within a single chip. However, this dissertation is only concerned with the passive waveguide coil, which is

fabricated to be compatible with the active integration techniques. Details of the active integration techniques can be found in [4][5].

Table 6. Gyroscope sensitivity categories based on ARW and bias drift (after [6]).

Parameter	Rate Grade	Tactical Grade	Inertial Grade
Angle Random Walk	>0.5°/√hr	0.5-0.05°/√hr	<0.001°/√hr
Bias Drift	10-1000°/hr	0.1-10°/hr	<0.01°/hr

This work was supported by DARPA MTO under iWOG contract No: HR0011-14-C-0111.

The sensitivity of the gyroscope was evaluated according to its angle random walk (AWR). Table 6 summarizes gyroscope categories of sensitivity, following [6].

6.1 Theory

In delay-based interferometric gyroscopes, the Sagnac effect is utilized to sense rotation [7]. The Sagnac effect describes the change in phase that two counter-propagating waves experience when traveling a cyclical path on a rotating platform. Fig. 51 depicts a simple schematic for a waveguide gyroscope coil.

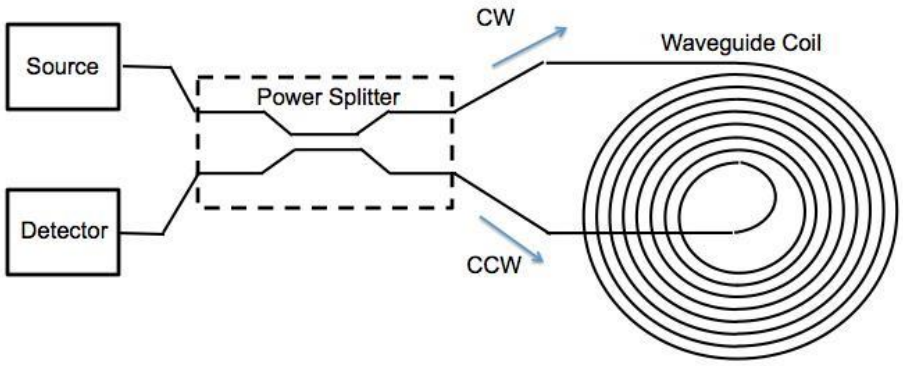

Fig. 51. Schematic of a waveguide gyroscope coil.

The source is typically an ASE source to avoid backscatter reflection noise. The light is split into two counter-propagating waves, which experience the same losses counter-propagating within the waveguide coil but experience different phase changes in the presence of rotation due to the Sagnac effect. These two signals are combined and measured at the detector. In this simplified scheme, the signals would destructively interfere in the absence of rotation, and a larger signal would be measured proportional to the rate of rotation. The phase difference between the two signals can be expressed as [1]:

$$\Delta\theta = \frac{8\pi NA}{\lambda_0 c}\Omega$$

Here N is the number of turns in the coil, A is the area enclosed by the coil, λ_0 is the wavelength of light, and c is the speed of light. To evaluate the effectiveness of a waveguide coil, all additional sources of phase change must be found to generate an equivalent noise rotation rate that will correspond to the minimum detection of the optical gyroscope, which is expressed as:

$$\Omega_{noise} = \frac{\phi_{noise}}{\Delta\theta/_{\Omega}}$$

The same sources of noise are considered in this dissertation as in [8]: shot noise, source RIN, thermo-refractive noise, and thermal noise of the preamplifier. The noise from each can simply be summed to attain the total noise. Each individual noise source is defined below, given in rad/√Hz:

$$\Delta\phi_{shot} = \sqrt{\frac{2hfB}{P_0\eta}}$$

Here, h is Planck's constant, f is the operating frequency, B is the measurement bandwidth, η is the quantum efficiency of the detector, and P_0 is the equivalent power detected.

$$\Delta\phi_{rin} = \sqrt{10^{\frac{RIN}{10}}}$$

Here, RIN is given in dBc/Hz.

$$\Delta\phi_{thermo-refractive} = 4.3 * 10^{-7}\sqrt{\frac{L}{40}}$$

Here, L is the length of the coil in meters. The thermo-refractive noise is given by:

$$\Delta\phi_{thermal} = \frac{10^{-9}}{P_0\eta\sqrt{R}}$$

Here, R is the termination resistance of the detector, taken to be 1 kΩ.

For all sensitivity simulations found within the dissertation, the following values were used: RIN = -128 dBc/Hz, B = 1Hz, η = 0.9, and P_0 = 100mw. Fig. 52 shows the results of this model using typical loss values for a 90nm core and a 40nm core, assuming an equal starting radius for the coil.

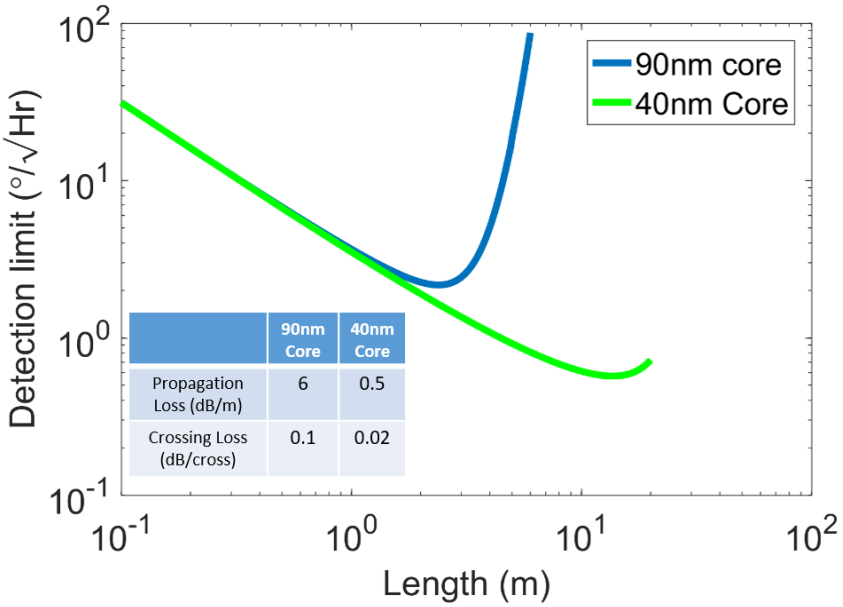

Fig. 52. Simulated gyro sensitivity vs length with a starting radius of 20mm, for typical loss values of a 40nm and 90nm waveguide core. The 40nm core has a propagation loss of 0.5dB/m and crossing loss of 0.02dB/cross, whereas the 90nm core has, correspondingly, 6dB/m and 0.02dB/cross. Simulation based on [8].

There is demonstrably an optimum length of sensitivity for a given coil performance. This optimum length increases as the loss performance of the coil is improved. If the length of the coil is held constant, decreasing the waveguide propagation loss has a negligible impact on the coil sensitivity. Additionally, if a coil has an optimized length for a specific waveguide loss and the fabricated waveguide, for whatever reason, has significantly higher waveguide loss, the sensitivity of the coil is drastically reduced.

6.2 Design

6.2.1 Waveguide Geometry

The conclusions offered in Section 2.5 were utilized to determine the appropriate waveguide design. To optimize the coil sensitivity, the lowest-loss waveguide structure with considerable length was implemented. Additionally, sensitivity may be purchased at the cost of the area of the coil, primarily determined by the starting radius of the coil. All these factors encourage the use of a thin-core waveguide, as the large bend radius is now a necessity for sensitivity. The typical waveguide properties and schematic for a 40nm core are summarized in Fig. 53.

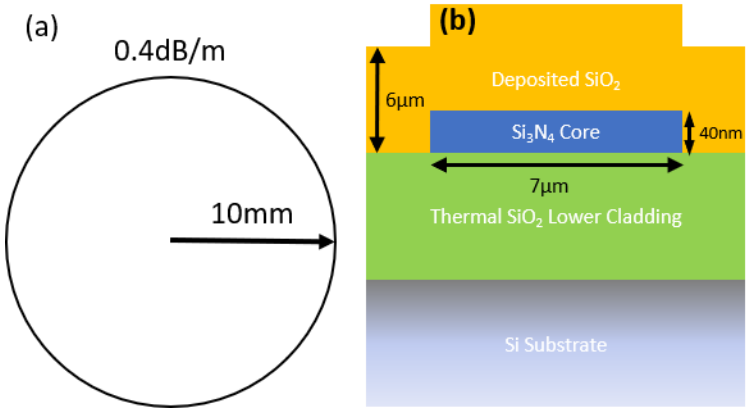

Fig. 53. (a) Typical propagation loss and minimum bend radius for a 40nm x 7µm waveguide and (b) schematic of the same waveguide.

6.2.2 Crossing Losses

IOGs require two inputs to the same coil to create two counter-propagating signals to yield useful rotational information. Outside of gyroscopes, a spiral that requires two inputs is usually drawn as an Archimedean spiral, shown in Fig. 53(a). However, the central s-bend changes the direction of the spiral. If such a spiral is used as a gyroscope, the rotational signals from the inward and outward spiraling directions will cancel one another out, and the gyroscope will not function. Instead, the center of the spiral must cross outwards to form the second input, shown in Fig. 53(b).

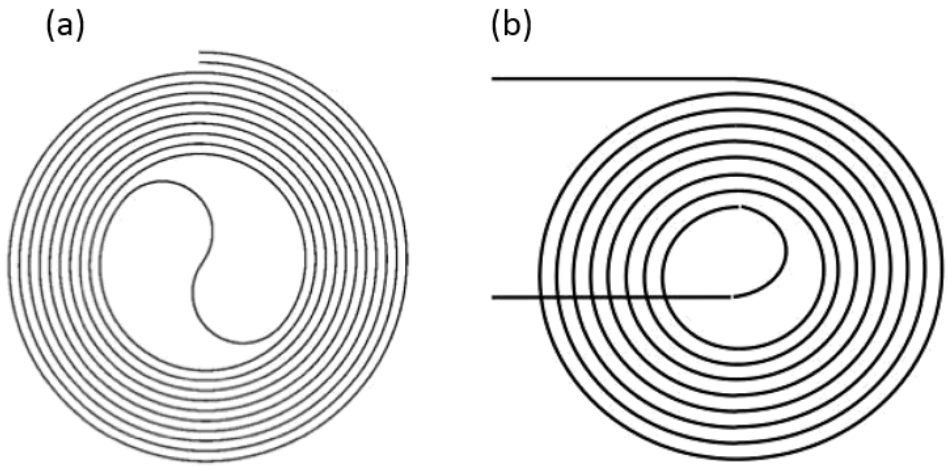

Fig. 54. (a) An Archimedean spiral with central s-bend. (b) IWOG-altered Archimedean spiral with secondary input crossing the spiral.

Although the waveguide coil has a curved waveguide, the crossings can be evaluated as straight-straight crossings, as the radius is large enough that it introduces a perturbation to the mode on the order of 10^{-6} change in the effective index. Simulating these crossings in Lumerical FDTD yields a crossing loss of 0.02dB/crossing.

6.2.3 Waveguide Stitching

The DUV stepper used to fabricate these waveguides has a maximum die size of 21mm x 25mm. The bend limit of 10mm in this project, due to the geometry of the waveguide core, prohibits complex structures with such an area restriction. To bypass this limitation, waveguide stitching was employed, thereby placing a continuous waveguide between two die and creating the complete structure with multiple exposures of the stepper system. However, the alignment of such a waveguide is not perfect. There can be a lateral offset between the waveguides at the interface of the two die. Tests of the lithographic alignment system yield a stitching offset of 50nm. A scanning electron micrograph of such a stitch is shown in Fig. 55.

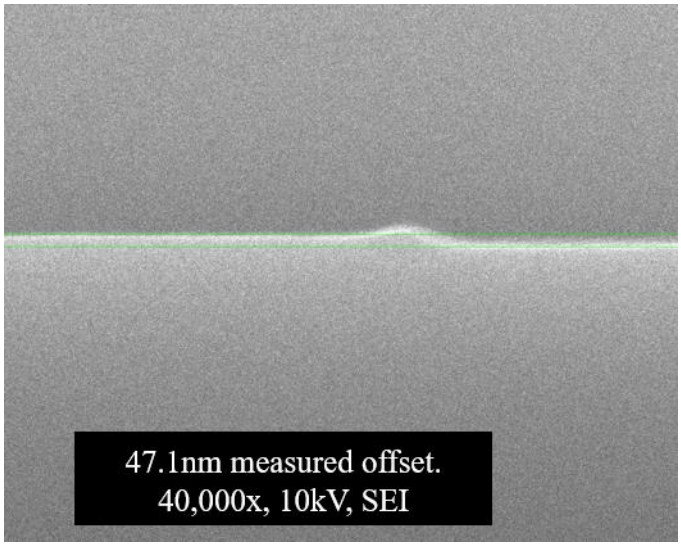

Fig. 55. A scanning electron micrograph of a 47.1nm stitching error between two waveguides.

This offset is consistent with the alignment accuracy reported for the DUV stepper, which represents a much smaller perturbation than a waveguide crossing; thus, the loss and reflection of a stitch are expected to be substantially smaller. Stitches with a 50, 100, and 150nm offset were simulated in Lumerical FDTD. The simulations yielded, respectively,

0.006, 0.011, and 0.016dB of loss per stitch, indicating a linear relationship between stitching offset and stitching loss for stitching offset much less than the waveguide width.

6.2.4 Coil Layout

Because the optimal length of the coil is sensitive to waveguide loss, coils of three meters and ten meters were fabricated, in case the stitching loss caused significantly higher losses than anticipated. The shorter coil consists of a 3-meter spiral, starting at a 20mm radius and ending at an 18.75mm radius, with a waveguide spacing of 50μm, turning 25 times. The waveguide then exits the coil with straight crossings, as shown in Fig. 56. As there are 25 turns, the coil has 25 crossings spiraling in and then 25 more crossing out, for a total of 50. Additionally, this large-scale device is separated into four lithography masks, generating 100 stitches throughout the total spiral propagation distance. The mask divisions are shown in blue in the figure below.

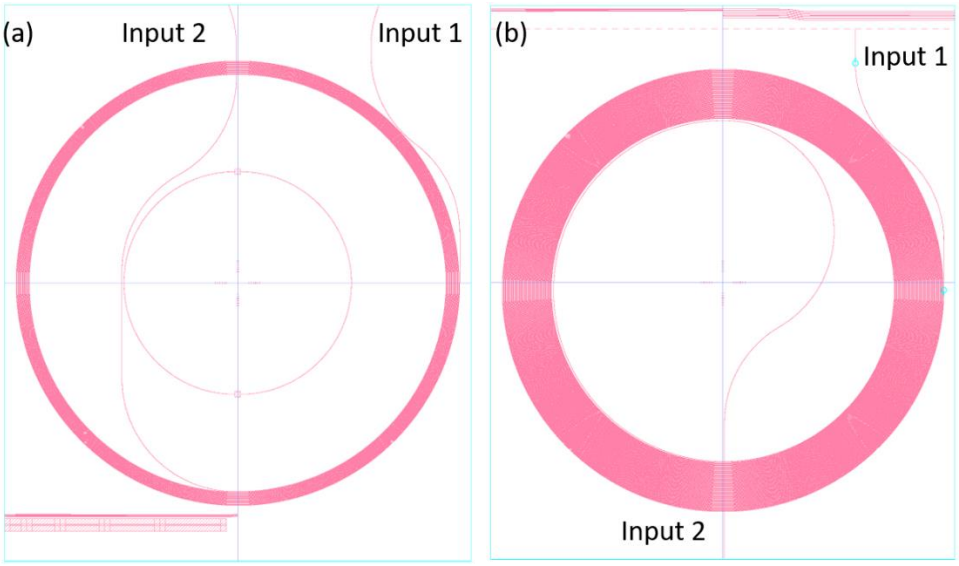

Fig. 56. (a) 3-meter gyro coil. The ring in the center is a stitching test structure and does not interact with the coil waveguide. Like-wise structures at the bottom are crossing cutback test structures. (b) 10-meter gyro coil. The structures at the top are for coupling loss measurements.

The 10-meter coil follows the same design, starting at the same initial radius and spiraling in to a radius of 15.4mm. It has a total of 90 turns, yielding 180 crossings and 360 stitches. The input and output are placed on opposite sides to make packaging easier.

6.3 Coil Fabrication

The coils were fabricated at separate times and made use of different upper claddings and anneals. The 3-meter coil used silane as a precursor for Si in its deposited upper cladding and was only annealed up to 1050°C. The exposed waveguide core crossings during fabrication are shown in Fig. 57(a). The completed coil is shown in Fig. 57(b), illuminated with two red lasers.

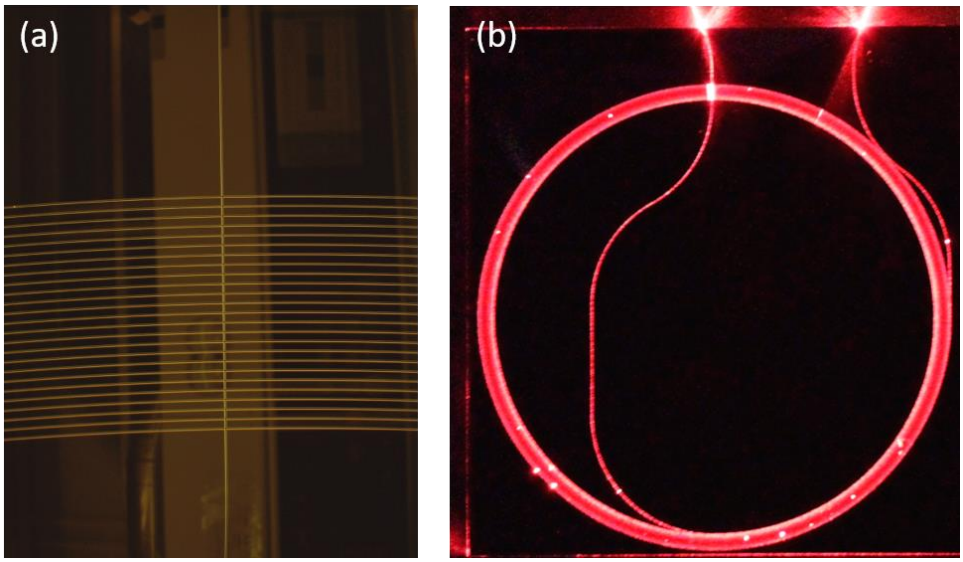

Fig. 57. (a) The 3-meter coil illuminated with two red lasers. Bright dots within the spiral indicate scattering points due to impurities. (b) A darkfield optical image of the exposed waveguide crossings. A reflection of the clean room equipment is present in the image.

The 10-meter coil utilized a TEOS-based upper cladding and had an additional anneal at 1150°C for two hours. The full fabrication process is given in Section 2.2. The conclusions from that section suggest that the 10-meter coil would have improved waveguide loss characteristics.

6.4 Results

The coil loss is measured using the OBR technique described in Section 2.4. Fig. 58(a) and Fig. 59(a) are the OBR traces of each coil. Although there are scattering points that resemble the reflections from the crossings, which ones belong to the crossings can be deduced by their regularity and spacing on the mask. These are identified on the 3-meter trace. The TM light experiences much higher bend losses and is essentially eliminated tens of centimeters into the coil, with the remaining noise floor comprising the TE light that was not eliminated by the polarization rotator. There is a 25dB extinction between the two modes after less than 50cm of propagation, which is one of the primary advantages of the waveguide optical gyroscope over the fiber optical gyroscope, as the fiber version can be limited by polarization noise [1].

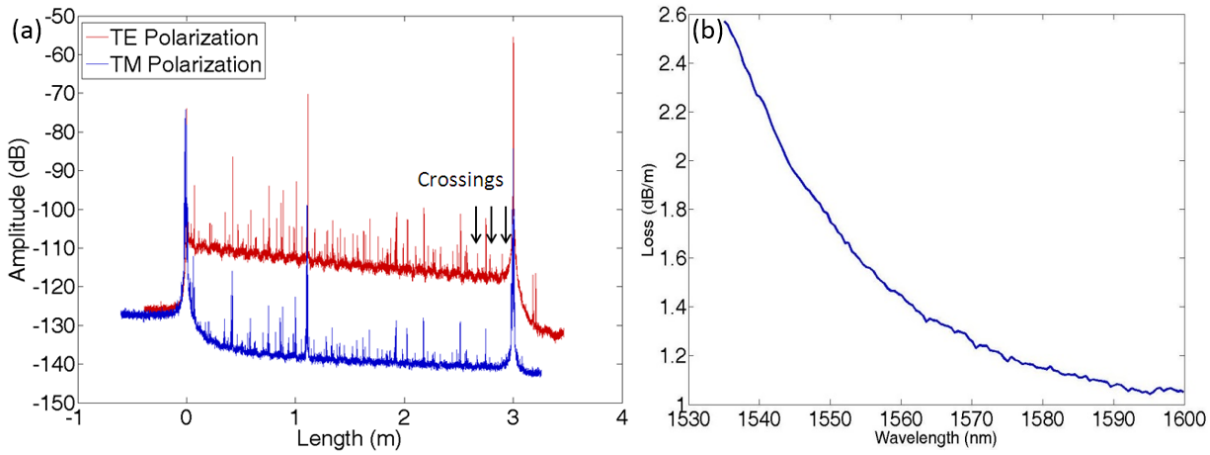

Fig. 58. (a) OBR trace of 3-meter spiral. (b) Resulting loss fit for TE mode. Loss includes crossing and stitching loss.

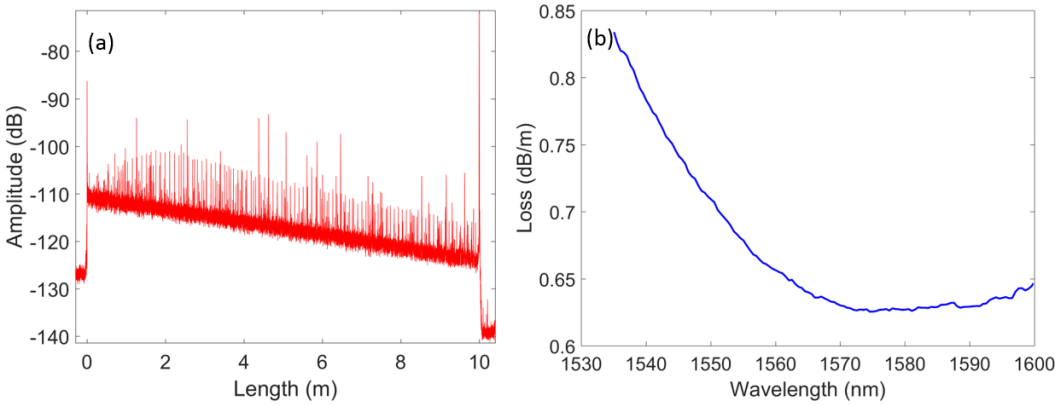

Fig. 59. (a) OBR trace of 10-meter spiral. (b) Resulting loss fit for TE mode. Loss includes crossing and stitching loss.

Fitting a line to the slope of the OBR traces yields the wavelength-dependent loss, shown in Fig. 58(b) and Fig. 59(b). These loss values include the stitching and crossing losses within the coils. The improved performance of the 10-meter coil is a result of using TEOS as a Si precursor in the PECVD deposition, as well the additional 1150ºC anneal.

The waveguide crossing loss was measured on a separate set of test structures located on the same processed wafers as the waveguide coils. The test structures consist of adjacent straight waveguides with varying numbers of waveguide crossings to simulate the cutback method of measurement. A linear fit is then performed to extract the loss per crossing, shown in Fig. 60.

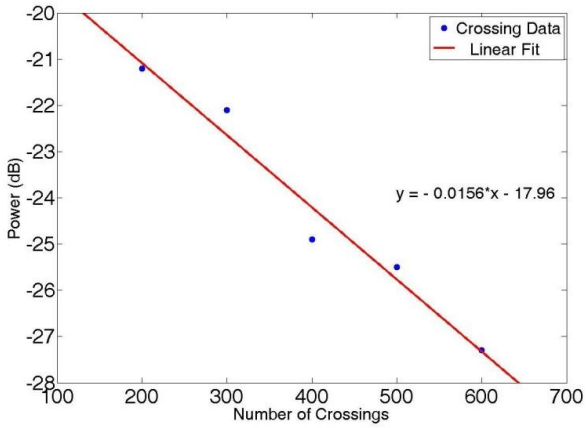

Fig. 60. Crossing test structure data on 3-meter wafer. The R^2 of the fit is 0.97.

The test yields a crossing loss of 0.0156dB/crossing, close to the simulated value of 0.02dB/crossing. The total penalty generated from crossings found within each coil can be calculated. The 3-meter coil has 50 crossings corresponding to 0.78dB of crossing loss, while the 10-meter coil has 180 crossings corresponding to 2.8dB of crossing loss. These losses are essentially agnostic to wavelength over the range of 1500nm to 1600nm. This loss contribution can be subtracted from the propagation loss measured by the OBR to yield the waveguide and stitching loss in the absence of crossings. The area required to create stitching cutback test structures is prohibitive due to the large bend radius of the waveguide, and thus, the present work is limited to using the simulated value of 0.006dB/stitch. Extracting the crossing and stitching loss at all wavelengths reduces the propagation loss by 0.26dB/m for the 3-meter coil and by 0.28dB/m for the 10-meter coil. This places their minimum propagation loss at 0.78dB/m and 0.37dB/m. The various coil parameters are summarized in Table 7.

Table 7. Summarized Coil Characteristics.

Characteristic	3-Meter Coil Value	10-Meter Coil Value
Outer Diameter	**40mm**	**40mm**
Inner Diameter	**37.5**	**30.8mm**
Crossing Loss	**.0156dB/cross**	**.0156dB/cross**
Stitching Loss (simulated)	**0.006dB/stitch**	**0.006dB/stitch**
Waveguide Loss	**0.78dB/m**	**0.37dB/m**

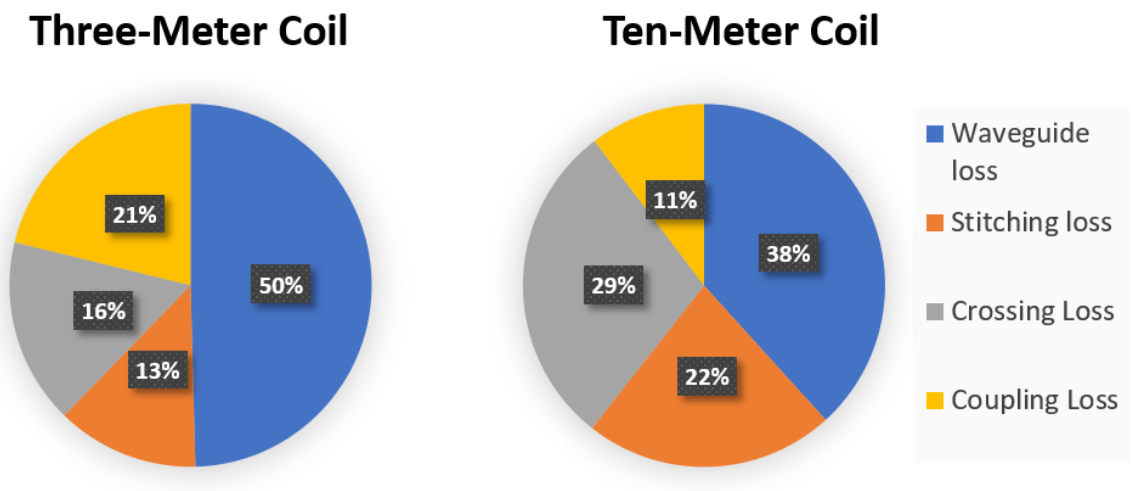

Fig. 61. Contributions from different loss sources in the 3-meter and 10-meter coils.

A visual comparison of different loss contributions in both coils is shown in Fig. 61. The reduction of waveguide loss between the two coils causes the stitching and crossing losses to nearly double in their proportional losses. The stitching loss will be reduced as the alignment system in steppers improves over time. The crossing loss, on the other hand, is more difficult to reduce. Multi-mode interference crossings have been demonstrated to significantly reduce loss [9], but they are limited by the beat length of the multi-mode waveguide, which would require crossings to be spaced approximately every 200μm (rather than the current figure of 50μm) for a 40nm core, significantly reducing the spiral area and reducing sensitivity. An effective solution to this issue is to utilize two separate vertical layers for each coil, eliminating the need for crossings, reducing the overall coil loss significantly and allowing the coil to remain at a larger radius for a larger percent of its length. This solution is explored more fully in the next chapter of this dissertation.

6.5 Simulated Performance

The coils were evaluated by simulating their performance as rotational sensors using the theory presented in Section 6.1, from [8]. An ASE source with 100mW of optical power with a RIN of -128dBc/Hz was assumed for these simulations. The results of the simulation are shown in Fig. 62. The 3-meter and 10-meter coil have respective sensitivities of 1.37°/√Hr and 0.58°/√Hr. Their optimal lengths for their waveguide performance would be 13.5m and 18m with sensitivities of 0.5712°/√Hr and 0.5°/√Hr.

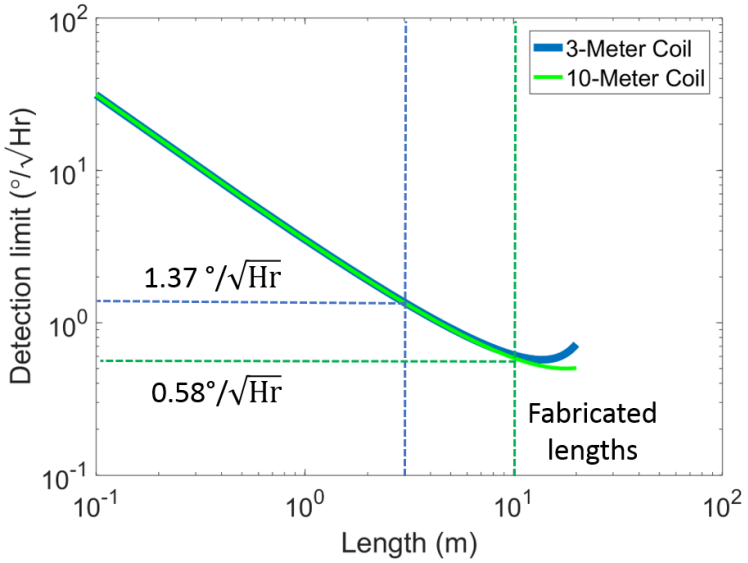

Fig. 62. Simulated sensitivity for 3-meter and 10-meter coil. Simulation based on [8].

6.6 Conclusion

In this chapter, a model was examined for simulating the theoretical detection limits of delay-based waveguide coils. Included in the model are four different noise sources: shot noise, RIN, thermo-refractive, and thermal noise. Using this model as a basis, two different waveguide coils, one three meters long and the other ten meters, were designed and fabricated. In order to leverage the lowest-loss waveguide possible while still utilizing the advantages of DUV

lithography, a waveguide stitching technique with simulated losses of 0.06dB/stitch or lower was employed. These coils had measured propagation losses of 1.1dB/m and 0.63dB/m, which includes the contributions of crossing and stitching loss. The waveguide crossing loss was measured by a cut-back-type measurement yielding a 0.0156dB/crossing. The normalized waveguide loss, in the absence of crossings or stitches, is calculated to be 0.78dB/m and 0.37dB/m, respectively. The longer 10-meter coil's performance was superior because it utilized a TEOS-based upper cladding and underwent an additional higher-temperature anneal of 1150°C.

The coils were evaluated as rotational sensors according to the model presented, with respective sensitivities of 1.37°/√Hr and 0.58°/√Hr. The 10-meter coil therefore has sufficient sensitivity to be classified as a tactical-grade gyroscope. More generous assumptions within the model, particularly with the laser RIN, can improve this figure substantially.

In future efforts, the waveguide loss can, presumably, be driven even lower. However, as this model suggests and these coils demonstrate, decreasing the propagation loss of the gyroscope coil will only lead to higher sensitivities if the length of the coil is increased simultaneously. This fact means that the coil will surrender its radius as it spirals inward, thereby reducing its sensitivity, and finally reaching a maximum value where the length cannot be increased without changing the initial radius and thus sacrificing the footprint of the device. This characteristic serves as powerful motivation to explore vertically stacking waveguide spirals. Vertically stacked coils allow higher lengths within the same chip area. The area used by this chip could allow for 45m of coil using two layers. In addition, the crossing loss of two layers that are vertically offset is negligible and eliminates the crossing loss of the coil, which

accounted for 29% of the loss penalty in the 10-meter coil. Such vertically stacked coils are explored in the next section of this dissertation.

6.7 References

[1] Lefevre, Herve C. *The fiber-optic gyroscope*. Artech house, 2014.

[2] Tin Komljenovic, et al., "Frequency Modulated Lasers for Interferometric Optical Gyroscopes", Optics Letters, Vol. 41, Issue 8, pp, 1773-1776, 2016.

[3] Gundavarapu, S., Komljenovic, T., Tran, M. A., Belt, M., Bowers, J. E., & Blumenthal, D. J. (2017, March). "Effect of direct PRBS modulation on laser driven fiber optic gyroscope." In *Inertial Sensors and Systems (INERTIAL), 2017 IEEE International Symposium on* (pp. 1-3). IEEE.

[4] Davenport, Michael L., and John E. Bowers. "Efficient and broad band coupling between silicon and ultra-low-loss silicon nitride waveguides." *Photonics Conference (IPC), 2016 IEEE*. IEEE, 2016.

[5] Piels, Molly, et al. "Low-loss silicon nitride AWG demultiplexer heterogeneously integrated with hybrid III–V/silicon photodetectors." *Journal of Lightwave Technology* 32.4 (2014): 817-823.

[6] Angus Andrew, "How Good is Your Gyro?," in IEEE Control Systems Magazine, February 2010.

[7] G. Sagnac, "L'éther lumineux démontré par l'effet du vent relatif d'éther dans un interféromètre en rotation uniforme," Compte-renduz à l'Académie des Sciences, vol. 95, 1913, pp. 708-10.

[8] Sudharsanan Srinivasan, Renan Moreira, Daniel Blumenthal, and John E. Bowers, "Design of integrated hybrid silicon waveguide optical gyroscope," Opt. Express 22, 24988-24993 (2014).

[9] Renan Moreira, "Integrated Optical Delay Line Circuits on a Ultra-low Loss Planar Waveguide Platform," Ph.D. dissertation, ECE Dept., UCSB, Santa Barbara, CA, 2013.

Chapter 7

Multi-Layer Waveguide Spiral Delay Line

The Si_3N_4/SiO_2 waveguide platform has produced record-low losses using foundry-compatible fabrication techniques, allowing new applications to be accessed using integrated optical waveguides, many of them presented or referenced within this dissertation. It has been previously proposed, within this platform, to integrate multiple waveguide layers to increase the complexity and length of devices while maintaining the same area footprint [1]. Moreover, multiple layers enable multiple waveguide core thicknesses to be used, allowing for a combination of waveguide properties to be utilized simultaneously.

In particular, delay-based waveguide optical gyroscopes (WOGs) stand to benefit from multi-layer spirals. Previous demonstrations of WOGs utilized crossings to preserve the rotational information while still maintaining two inputs for counter-propagating signals [2]. However, these crossings add significant loss and create reflection points that are problematic for high-sensitivity gyroscopes [3]. Utilizing a multi-layer spiral design eliminates these crossing points, as the different layers offer improved routing capabilities.

Vertically coupled waveguides have been used in ring resonators [4][5], aiming to improve fabrication tolerance in the coupling region by controlling the coupling gap with precise control of layer thicknesses rather than lithographic accuracy. However, these vertical waveguides do not represent significant spiral or delay lengths and their loss characteristics have not yet been evaluated.

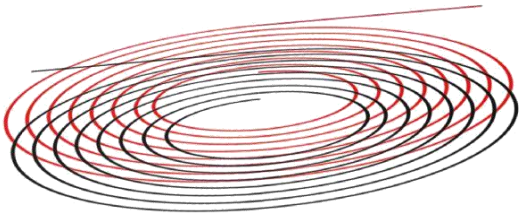

Fig. 63. Schematic of a two-layer waveguide spiral. Intermediate coupling layer is not shown.

In this chapter, the modeling, design, fabrication, and measurement of a multi-layer 10-meter spiral, with 5-meter spiral sections on two separate layers, shown in Fig. 63, are presented. These two spiral layers are optically isolated from each other by controlling the effective index of each waveguide mode, as well as a large physical separation. Power can be coupled between the layers at high efficiency using tapered vertical couplers and an intermediate coupling layer that sits halfway between the two spirals. These couplers are based on vertical couplers previously demonstrated on this platform [6].

This work was supported by DARPA MTO under iWOG contract No: HR0011-14-C-0111. This multi-layer coil was designed as a proof of concept for a multi-layer gyroscope coil.

7.1 Optical Interactions between Vertical Layers

The process and design of single-layer ULLW spirals are well developed. When extending these techniques to multiple vertically stacked layers, there are two additional challenges: designing efficient and broadband vertical couplers between layers and optically isolating the layers within overlaps in the spirals. Previous vertical couplers on this platform utilized two 90nm waveguide cores separated by 2μm of cladding [6]. However, these waveguides experience considerable coupling during waveguide overlaps outside of the intended coupling regions, which can be modeled by considering two vertically separated waveguides running parallel to each other as a directional coupler, shown in Fig. 64.

This model considers the cross-talk case on a "worst scenario" basis, as spiraling waveguides will cross numerous times at shallow angles but will not run parallel indefinitely. However, if cross-talk can be reduced to acceptable levels within this model, the actual multi-layer spiral will perform even better. Coupled mode theory [7] was utilized in this dissertation to determine the power coupled to each port considering an excitation from the input port, $a_1(0)$. The amount of power coupled between the two waveguides, as a function of the propagation length z, is given by:

$$a_2^2 = \frac{\kappa^2}{s^2}\sin^2(sz)$$

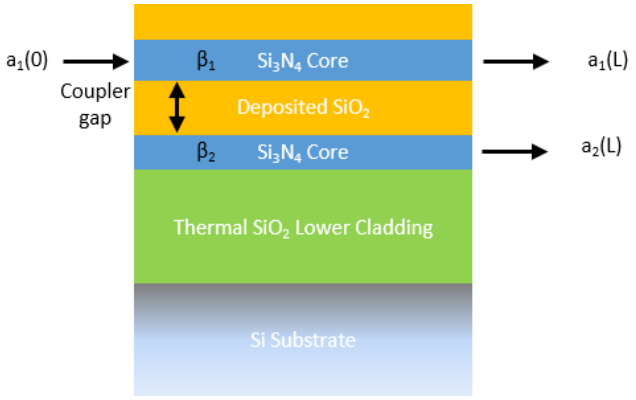

Fig. 64. Multi-layer coupling interaction depicted as a vertical coupler. a_n denote input and output ports of the vertical coupler, and β_n denote the different propagation constant in each waveguide layer.

Here κ is the coupling coefficient determined by an overlap integral of the two waveguide modes, and s is defined as:

$$s = \sqrt{\left(\frac{\beta_1 - \beta_2}{2}\right)^2 + \kappa^2}$$

Where β_1 and β_2 are the propagation constants for each waveguide. If β1 = β2, meaning the waveguides have the same geometry (and materials), full power can be transferred between each waveguide when z = π/2s. This case is simulated for two identical waveguide geometries, 90nm x 2.8μm, separated by 6μm using Fimmprop, shown in Fig. 65.

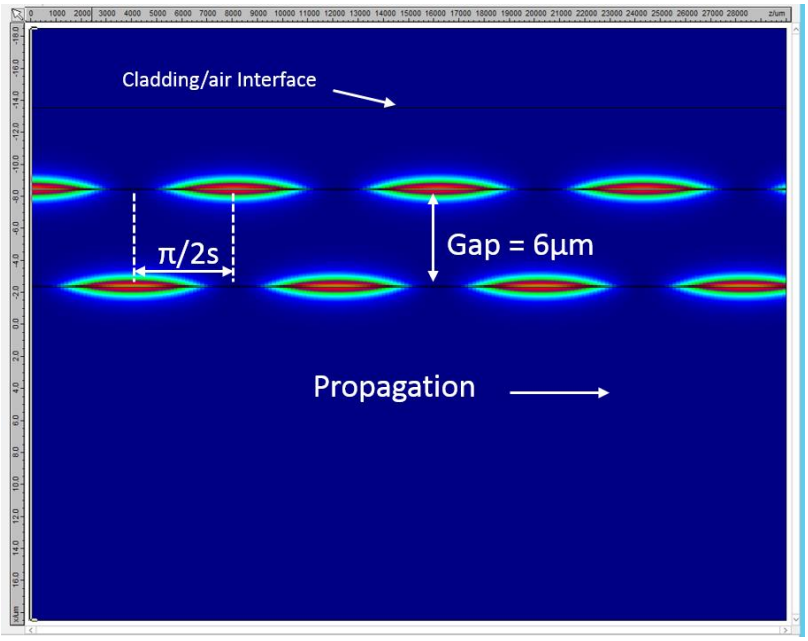

Fig. 65. Vertical coupling between two 90nm x 2.8µm waveguides separated by 6µm.

Further increasing the separation of the waveguides decreases the waveguide coupling, κ, but still allows 100% of the power to be transferred. Therefore, to decrease the power coupled between the waveguides, the waveguides must be designed to have distinct propagation constants, β_1 and β_2. Specifically:

$$\beta_1 - \beta_2 \gg 2\kappa$$

The coupling coefficient can be decreased by increasing the waveguide gap to ease the requirement on the β mismatch between layers.

The propagation constant β is related to the effective index of the mode by:

$$2\pi n_{eff} = \lambda_0 \beta$$

The various effective indices that can be fabricated can be simulated by changing the width and thickness of the waveguide cores using Fimmwave, shown in Fig. 66. Thicknesses between 60nm and 90nm were considered, as lower thicknesses would require waveguide stitching and additional masks, which is an unnecessary complication and expense for this

experiment. In addition, thicker waveguides were not explored, as propagation loss should be kept low to measure the considerable spiral lengths on each layer.

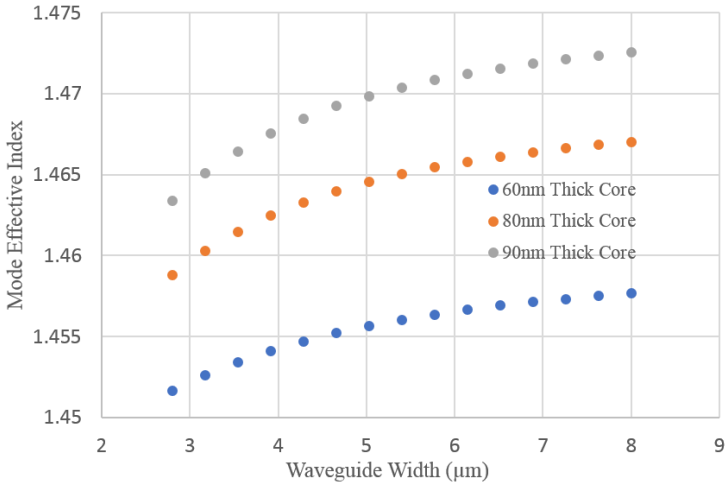

Fig. 66. Effective index for various core thickness and widths.

Fig. 66 shows that changing the waveguide thickness has a much larger impact on the effective index than changing the width. This difference in impact makes changing the thickness of the core more effective in isolating the layers. In addition, if the same core thickness were used between two layers, and large changes were implemented in the width to induce a large Δn_{eff}, multi-mode waveguides would be present on one of the layers. Although multi-mode waveguides can be used by exciting only the fundamental mode [8], the perturbations involved in crossing vertically separated waveguides can excite the higher order modes, which is unacceptable in many applications, particularly gyroscopes.

The vertical directional coupler model of crosstalk and different coupling gaps and Δn_{eff}, will be explored next. As shown in Table 8, for the waveguide thicknesses and widths explored, there is no Δn_{eff} that can isolate the layers without the possibility of significant power coupling during overlaps for a 3-µm gap. If the gap is increased to 6µm, "worst case" coupling values of 0.1% or even less than 0.01%, the floor of the simulation, can be attained.

Table 8. "Worst case" power coupling between two vertically separated waveguide layers with various coupling gaps and Δn_{eff}.

Δn_{eff}	Power Coupled	Coupling Gap (μm)
0	100%	3
0	100%	6
0.01	22%	3
0.01	0.1%	6
0.025	9%	3
0.025	<.01%	6

The lowest cross-talk case has a Δn_{eff} of 0.025, which corresponds to using 60nm x 4.8μm and 90nm x 2.8μm cores. Both widths are below the multimode limit of their respective core thicknesses. Their simulated coupling, over 100mm—which is far greater than any overlap would involve—is shown in Fig. 67.

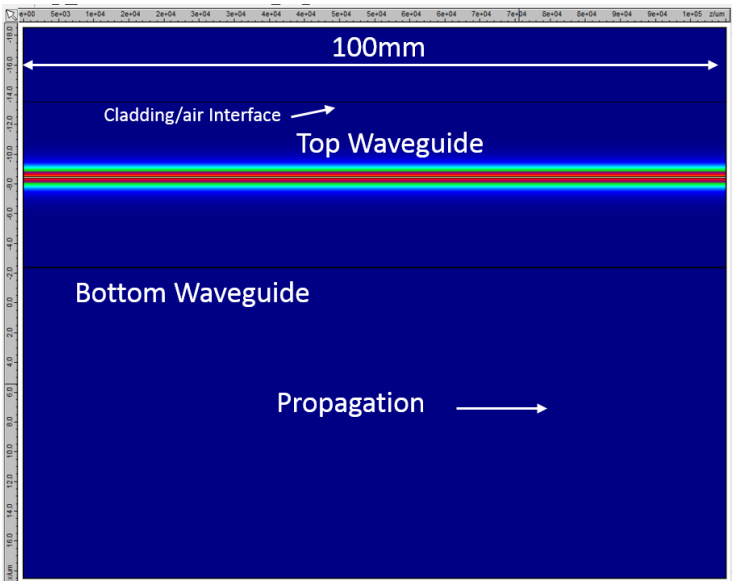

Fig. 67. Vertical coupling between 60nm x 4.8μm bottom waveguide and 90nm x 2.8μm bottom waveguide separated by 6μm over a 100mm overlap.

In this case, there is clearly no significant coupling between the two layers with an excessive overlap length. These are the waveguide geometries ultimately used in this project. However, first the ability to couple light intentionally between the layers must be ensured.

This is accomplished by tapering the waveguide widths when the layers are directly overlapping. Tapering the waveguide widths simultaneously reduces confinement to allow for higher modal overlap between the two layers and ensures that the two layers match effective indices at some point within the taper [9]. A taper tip of 500nm is easily achievable with DUV lithography.

Various coupling gaps and taper widths are simulated for the 90nm and 60nm waveguide core case, as shown in Table 9.

Table 9. Power coupled across a vertical coupler between 60nm and 90nm thick cores with various taper lengths and layer gaps.

Taper Length (mm)	Gap (µm)	Power Coupled
1	6	9.3%
3	6	25%
6	6	45%
3	3	99.2%

Using a 6µm gap prohibits efficient power coupling between layers without a taper of excessive length. However, reducing the coupler can allow for efficient operation with a 3mm taper across a 3µm gap, with only 0.03dB of loss. Under the parameters explored in this project, there is no solution for two layers to be optically isolated during overlaps and have efficient tapered couplers.

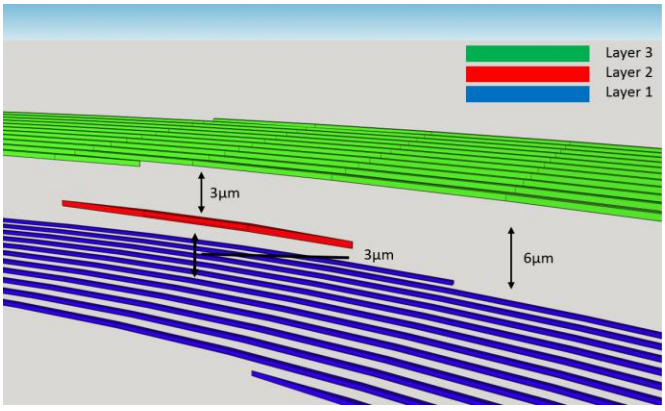

Fig. 68. Coupling region of a multi-layer spiral, involving a third intermediary coupling layer. There are two couplers, each crossing a 3µm gap, with a simulated loss of 0.03dB per gap transition. The spiral layers themselves are separated by 6µm.

However, if an intermediate coupling layer is utilized between the two spiral layers, two vertical couplers can be utilized, each across a 3μm gap, while the spiral layers themselves are separated by 6μm. The coupling region of such a three-layer coupler is shown in Fig. 68. Using this three-layer design can produce high-efficiency couplers across the 3μm gaps between layers while maintaining 6μm gaps between the overlapping spiral layers.

7.2 Design

The entire device is spread over three vertical layers, each separated by 3μm on SiO2. The first layer (called the bottom layer) and the third layer (called the top layer) are each 5-meter spirals with separate inputs. The second layer (called the intermediate or coupling layer) is two 3mm-long tapered couplers joined by a 10mm waveguide. It does not overlap with the other layers outside of the tapered coupling regions. The mask layers are depicted in Fig. 69(a)(b) and (c). The schematic of the layers of the device is shown in Fig. 69(d)

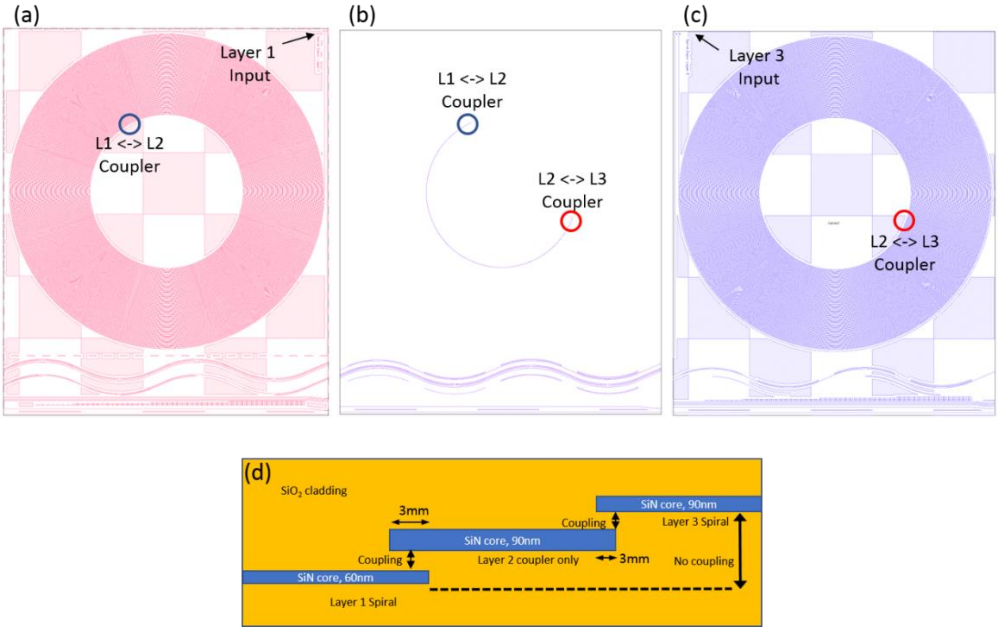

Fig. 69. (a) First (bottom) waveguide layer, (b) second (coupler) waveguide layer, (c) third (top) waveguide layer, and (d) schematic of all device layers. The bottom portion of the masks are test structures for measuring the vertical couplers.

The spirals have an outer radius of 10mm and an inner radius of 4.9mm. The entire device, including test structures, takes up 21 x 25mm, while the 10m multi-layer spiral itself is 21 x 21mm.

The bottom layer is a 60nm x 4.8µm waveguide, while the intermediate and top layers are each 90nm x 2.8µm waveguides. The waveguide schematic and typical properties are shown in Fig. 70.

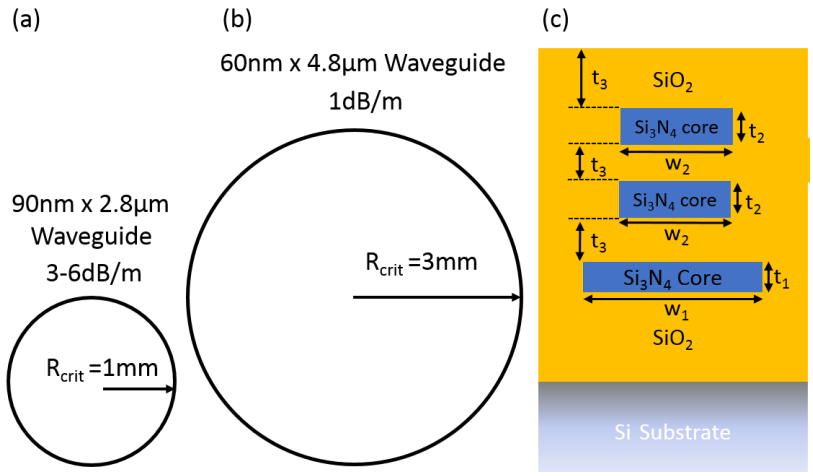

Fig. 70. (a) Properties of top layer 90nm waveguide. (b) Properties of the bottom layer 60nm waveguide. The visual representations of the critical bend radii are not to scale. (c) A schematic of the entire waveguide layer stack, where t_1=60nm, t_2=90nm, t_3=3µm, w_1=4.8µm, and w_2=2.8µm.

Published results with the 90nm (and very similar 100nm) cores have losses ranging from 3-6dB/m [10][11]. There do not appear to be any published results for the 60nm core, although results within the Blumenthal group range from 1-3dB/m.

7.3 Fabrication

The multi-layer fabrication process is similar to executing the single-layer process, detailed in Section 2.2, multiple times, with a few additional steps and considerations. The multi-layer process is schematically summarized in Fig. 71.

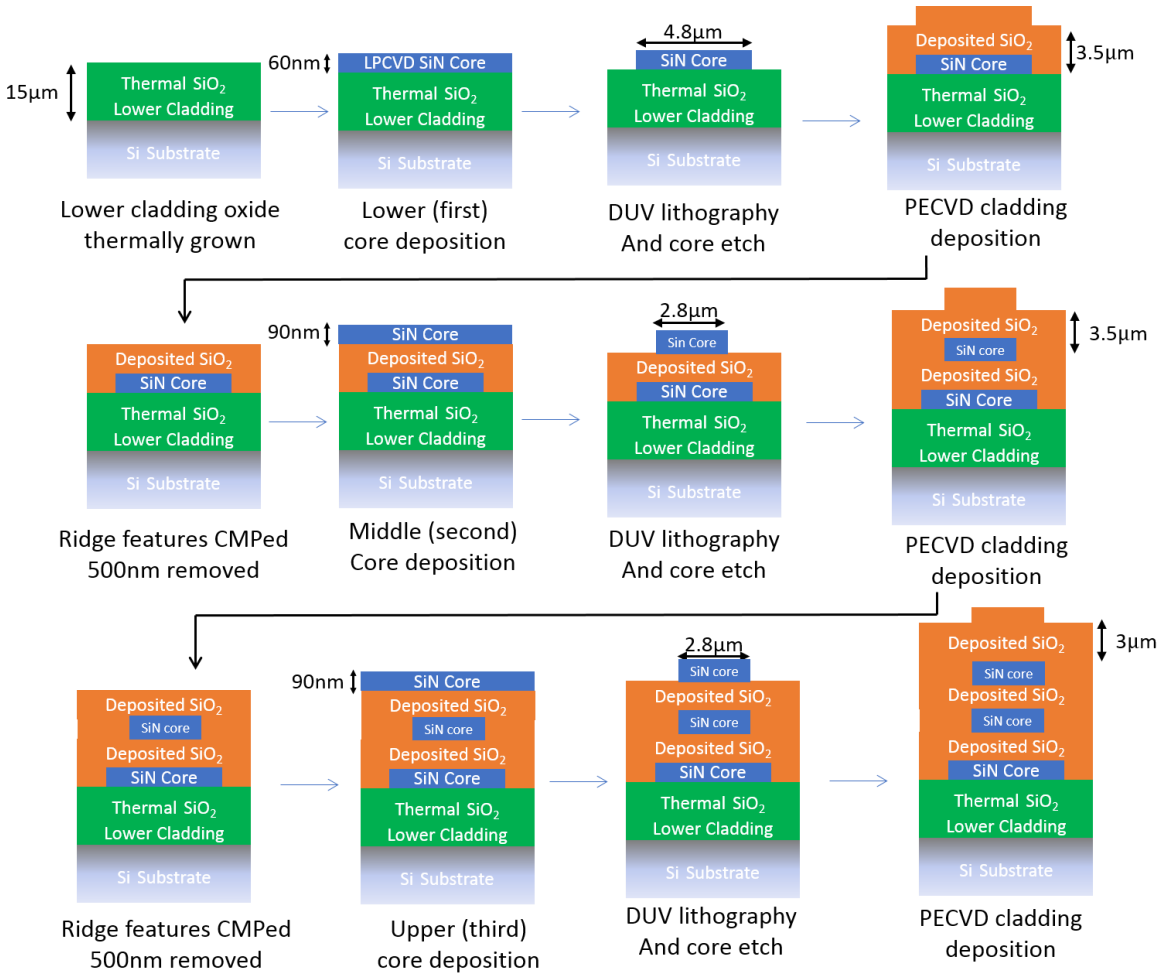

Fig. 71. Cross-section schematic of the multi-layer process flow.

The materials used for the core and cladding are consistent with the single-layer process. The two primary differences are the starting wafer thickness and the inclusion of a CMP (chemical mechanical polishing) step before each new core is deposited. A 1mm-thick, 100m-diameter wafer must be used. This thicker wafer is used to ensure that the stress of multiple layers does not create significant bow in the wafer and impede further processing. A thicker wafer is not necessary if other bow-reduction techniques are included, such as back-side compensation for the thick annealed SiO_2 layers.

The CMP step is added before each Si_3N_4 deposition (other than the first) to remove the ridge feature created by the previous Si_3N_4 layer. The oxide layers are deposited with an

additional 500nm thickness so that the excess can be removed during CMP. Without this CMP step, waveguide crossings and overlaps would involve a 90nm vertical step and would drastically increase in loss [9]. In addition, this CMP step has strict requirements regarding the surface roughness of the polished material. Because the core layer is deposited directly onto the polished SiO_2 surface, any significant roughness has a devastating impact on the propagation loss. The theory behind the surface roughness and loss relationship is presented in Section 2.3.1. RMS roughness on the order of 0.5nm is required for low-loss propagation.

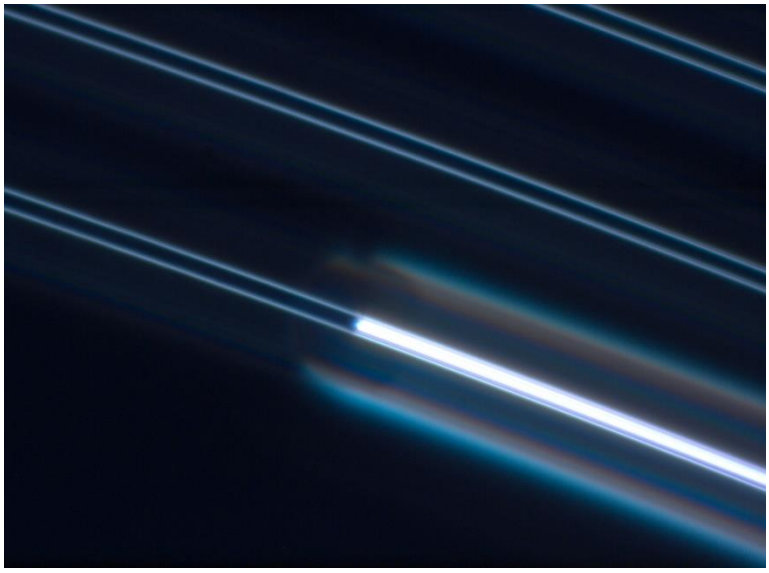

Fig. 72. A microscope image of the photoresist of the second layer taper overlapping the bottom layer nitride that is buried under 3µm of oxide. The microscope is focused on the bottom layer.

Each layer is aligned to the first waveguide layer within 50nm. Because the taper tips are on the order of 500nm, this alignment is quite sufficient. Fig. 72 shows the photoresist of the second layer over the already processed bottom layer.

7.4 Results

The spirals were evaluated using the OBR. Details regarding OBR measurements for group index and loss can be found in Section 2.4 or in [10]. To accurately correlate the physical

lengths of the waveguide to the time data of the OBR, the group index of the top and bottom spiral layers must be separately measured, which is accomplished using straight waveguides of known length and fitting the group index appropriately. This process results in n_{gbot} = 1.51 and n_{gtop} = 1.54, which are typical values for those waveguide geometries.

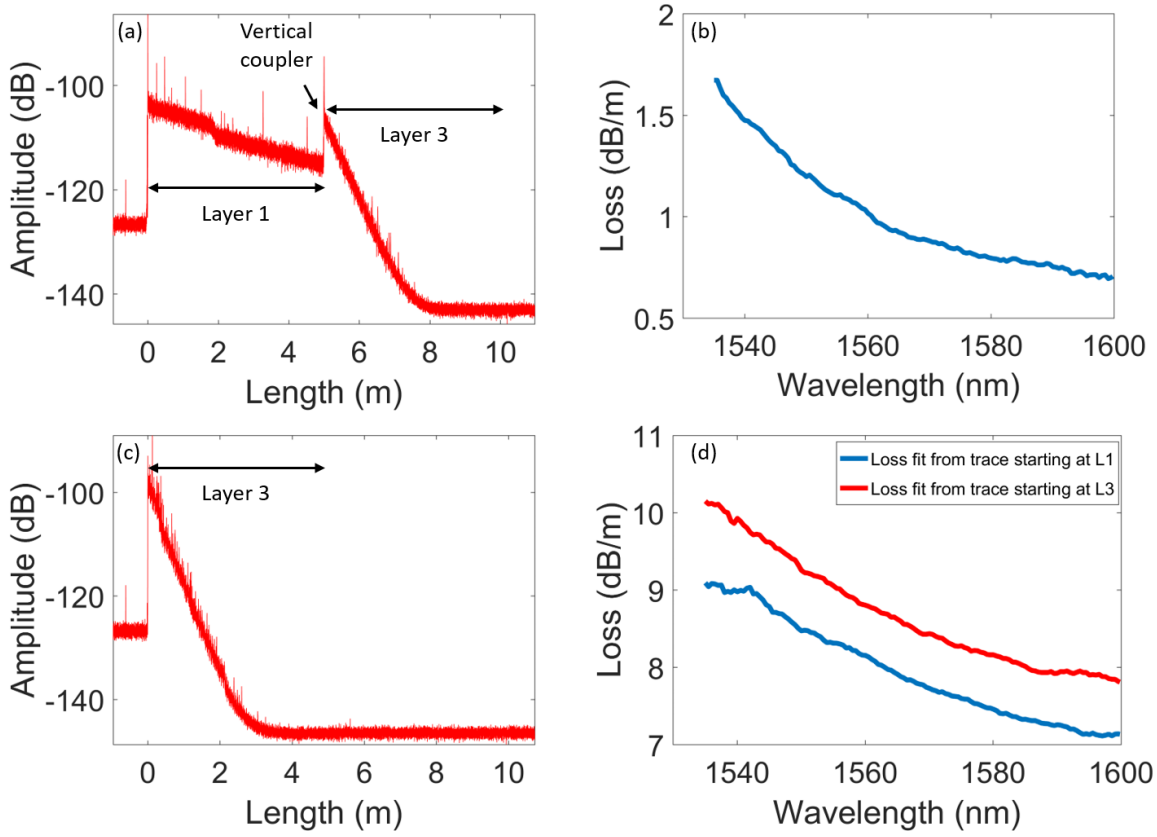

Fig. 73. (a) and (c) are OBR traces from the bottom and top layer, respectively. (b) and (d) are the resulting loss fit for the bottom and top layer, respectively. (d) includes a loss fit from both (a) and (c).

Measurements are made from inputs starting on each layer. Fig. 73(a) and (c) show the OBR traces of the bottom and top layer, respectively. Fig. 73(b) shows the resulting loss fit to the upper layer in Fig. 73 (a), and Fig. 73(d) shows the resulting loss fit to the lower layer in both Fig. 73 (a) and (c). The loss of the upper layer is 1.21dB/m at 1550nm, and the minimum measured loss is 0.70dB/m at 1600nm. The loss of the lower layer, averaged between the two fits, is 8.83dB/m at 1550nm, and the minimum measured loss is 7.47 dB/m at 1600nm. The

difference between the loss fit for the third layer measured from each separate input is consistent across many devices.

The vertical transition point is clearly visible in Fig. 73(a) at the 5-meter point of the spiral. The sharp separation between layers and the clear, distinct slopes indicate that the two layers are optically isolated from each other. If the coils had significant cross talk between them, the traces would have a curved aspect to them, as power transfers between layers with different losses, thereby changing the slope. This effect has been observed in previous multi-layer spirals.

The increase in slope and amplitude after the transition between layers indicates that the third layer has increased scattering loss, similar to the initial transition from fiber to chip. This loss is consistent with the loss values from a statistical fit. The transition between layers cannot be seen from the top input due to the higher loss of that layer.

It is useful to compare the stacked waveguide performance to similar single-layer waveguide performance to see how the stacking process alters the performance of these waveguides. A direct comparison is available for the 90nm top layer in [10], which reports a waveguide loss of 4.2dB/m at 1550nm, while [11] uses a similar 100nm x 2.8μm core and reports losses of 8 to 6dB/m over 1535 to 1600nm. Compared to these results, the top-layer waveguide here, with 8.8dB/m of loss at 1550nm, is reasonable and consistent but on the higher end of the spectrum. As shown in Fig. 74, a sample was cleaved and the top waveguide core was examined in a cross-sectional SEM.

The core has a 71.4° sidewall as opposed to the target value of 90°. This discrepancy is most likely caused by the focus offset of the DUV exposure for that layer, which did not take into account the additional vertical offset of the layer stack. Waveguides with such a sidewall

angle allow energy to couple between the TE and TM modes of the waveguide [12]. Because the present waveguide design has very high bend losses for TM light, this modal conversion is, essentially, a new loss source. Vertical sidewalls on the upper layer should reduce the propagation loss and make it competitive with the best published results for this waveguide geometry.

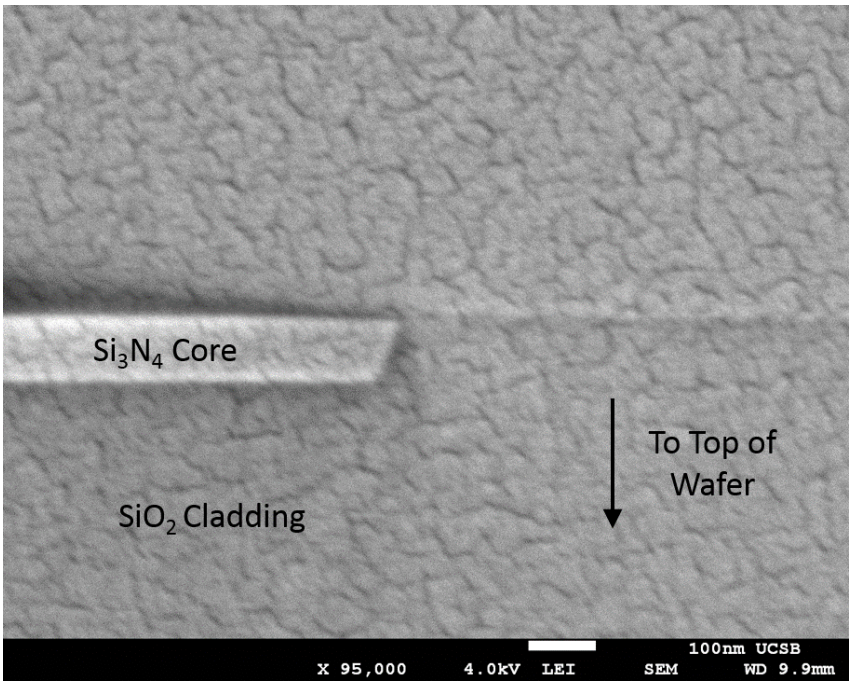

Fig. 74. Facet SEM of top waveguide core. The image is top/bottom reversed.

The 60nm bottom waveguide layer does not have a similar comparison to a published result. However, unpublished results within the Blumenthal group had typical loss values between 1-2dB/m. That makes this result, of 0.7dB/m loss at 1600nm, the best-performing 60nm waveguide fabricated in this work. From this result, it is apparent that the bottom waveguide is not impeded by the inclusion of additional waveguide layers.

Test structures to measure the coupling loss between each layer were included in the mask design. However, these structures are flawed because of the unrestricted tiling from the bottom and top layers. When the second layer propagates in an area that has tiling from the other

adjacent layers, it experiences unpredictable loss, and thus, the loss from each layer transition cannot be measured. The similarity between these couplers and [6] suggests they should be fairly efficient. In addition, the total through penalty from the OBR losses was calculated and compared with excellent agreement to the penalty measured from direct input to output through both layers, indicating that the couplers do not have a large excess loss.

7.5 Conclusion

In this chapter, the design, fabrication, and measurement of vertically stacked waveguide spirals on the Si_3N_4 waveguide platform were presented. This constitutes the first demonstration of two low-loss spirals vertically integrated together. The layers were designed to be optically isolated by using a vertical directional coupler model and assuming the worst case of 100% waveguide overlap. Even under these circumstances, the model indicates that less than 0.01% of power would be coupled between the two layers by controlling the Δn_{eff} and coupling gap between the layers. The multi-layer spiral utilizes an intermediate coupling layer to ensure high coupling efficiency between the two spiral layers. These waveguides demonstrated comparable performance to similar single-layer waveguides. It is possible to use this technique to increase the length of delays and complexity of chips within a limited area, as well as to utilize the different bend loss and propagation properties of different core thicknesses simultaneously.

7.6 References

[1] John, Demis D., et al. "Multilayer platform for ultra-low-loss waveguide applications." *IEEE Photonics Technology Letters* 24.9 (2012): 876.

[2] Huffman, Taran, et al. "Ultra-low loss large area waveguide coils for integrated optical gyroscopes." *IEEE Photonics Technology Letters* 29.2 (2016): 185-188.

[3] Lefevre, Herve C. *The fiber-optic gyroscope*. Artech house, 2014.

[4] Little, B. E., et al. "Vertically coupled glass microring resonator channel dropping filters." *IEEE Photonics Technology Letters* 11.2 (1999): 215-217.

[5] Kokubun, Yasuo, et al. "Fabrication technologies for vertically coupled microring resonator with multilevel crossing busline and ultracompact-ring radius." *IEEE Journal of selected topics in quantum electronics* 11.1 (2005): 4-10.

[6] Moreira, Renan, et al. "Optical Interconnect for 3D integration of ultra-low loss planar lightwave circuits." *Integrated Photonics Research, Silicon and Nanophotonics*. Optical Society of America, 2013.

[7] Coldren, Larry A., Scott W. Corzine, and Milan L. Mashanovitch. Diode lasers and photonic integrated circuits. Vol. 218. Wiley.com, 2012.

[8] Bauters, Jared F., Martijn JR Heck, Demis D. John, Jonathon S. Barton, Christiaan M. Bruinink, Arne Leinse, René G. Heideman, Daniel J. Blumenthal, and John E. Bowers. "Planar waveguides with less than 0.1 dB/m propagation loss fabricated with wafer bonding." Optics Express 19, no. 24 (2011): 24090-24101.

[9] Renan Moreira, "Integrated Optical Delay Line Circuits on a Ultra-low Loss Planar Waveguide Platform," Ph.D. dissertation, ECE Dept., UCSB, Santa Barbara, CA, 2013.

[10] Bauters, Jared F., et al. "Ultra-low-loss high-aspect-ratio Si 3 N 4 waveguides." *Optics express* 19.4 (2011): 3163-3174.

[11] Moreira, Renan, Sarat Gundavarapu, and Daniel J. Blumenthal. "Programmable eye-opener lattice filter for multi-channel dispersion compensation using an integrated compact low-loss silicon nitride platform." *Optics express* 24.15 (2016): 16732-16742.

[12] Wang, Zhechao, and Daoxin Dai. "Ultrasmall Si-nanowire-based polarization rotator." *JOSA B* 25.5 (2008): 747-753.

Chapter 8

Summary & Conclusions

In this dissertation, the ultra-low-loss Si_3N_4 waveguide platform and the varying waveguide properties made possible by manipulating the waveguide design, primarily the Si_3N_4 core thickness, were examined. These varying waveguide properties were used to design and fabricate a number of devices. The devices, as well as the waveguides they used and their properties, are summarized in Fig. 75.

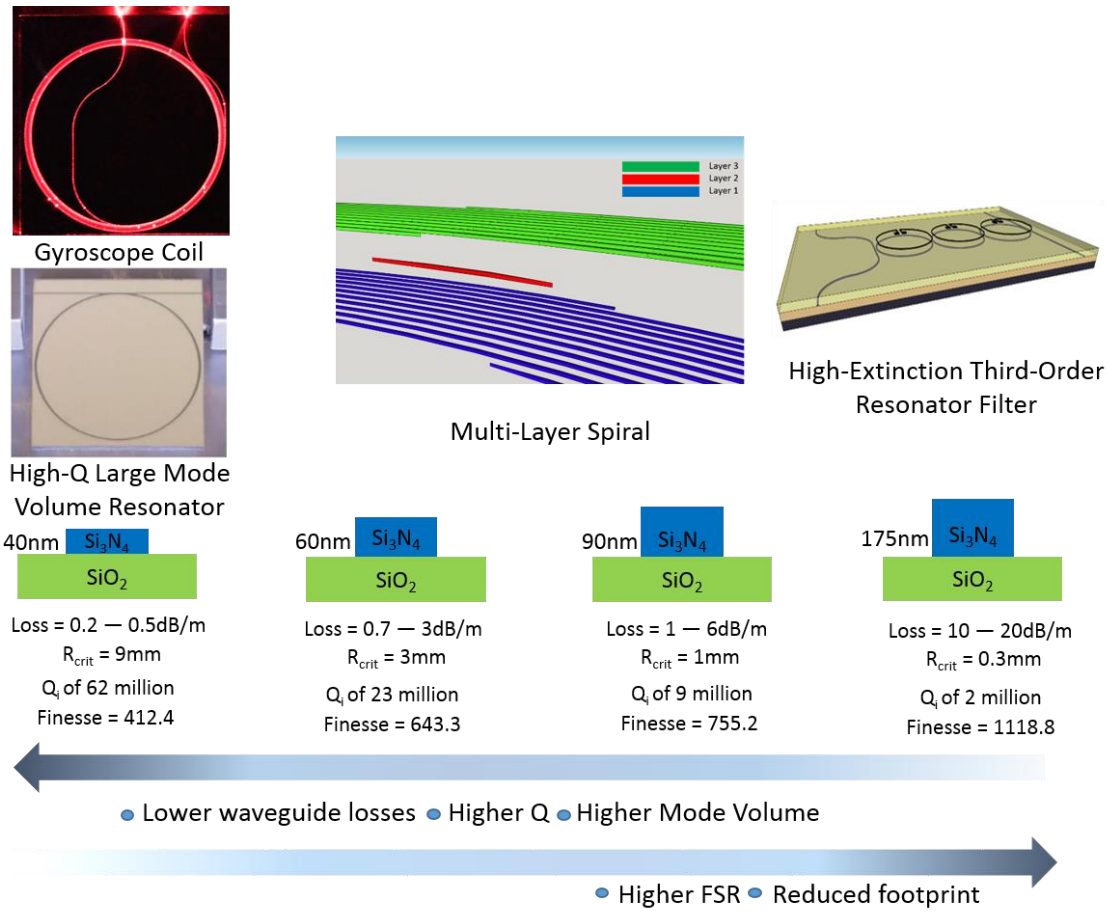

Fig. 75. A summary of waveguide properties based on waveguide thickness and a review of the devices made with each thickness.

Using the thin, weakly guiding cores, the ultra-low propagation losses and large bend radii were leveraged to create a 62 million Qi resonator that achieved Brillouin lasing, as well as the first delay-based waveguide gyroscope coil with a simulated sensitivity of 0.58°/√Hr, thereby classifying it as a tactical-grade gyroscope. Using thicker, more confined cores, a tunable 50GHz free spectral range wavelength filter was created with a record measured ultra-high extinction ratio of 80dB, using a third-order resonator design. Finally, a multi-layer coil was presented that used a large Δn_{eff} and gap to optically isolate two layers while using an intermediate layer to couple efficiently between them, demonstrating, for the first time, ultra-low loss propagation on two independent waveguide layers. This approach to multi-layer devices can utilize multiple waveguide thicknesses, and therefore properties, to create more complex devices. Finally, future work within this waveguide platform that will have significant impacts on future device integration are discussed.

8.1 Future Directions

8.1.1 Waveguide Phase Tuning

Being able to tune the optical path length of a waveguide enables many different types of components, most notably, switches and modulators. Currently, the Si_3N_4 waveguide platform utilizes resistive thermal heaters to perform this function, as demonstrated with the high-extinction tunable filter. However, these heaters are grossly inefficient, requiring hundreds of mW to induce a Pi phase shift, and act very slowly, allowing for only KHz operation. There is room for optimization, particularly for the efficiency, but there is no path to GHz or even MHz operation using thermal tuning. Any proposed waveguide tuning mechanism to improve upon speed or efficiency must also avoid generating any significant amount of loss. Some loss

penalty for switches using a Mach-Zehnder format are acceptable; however, if the phase tuner induces a significant amount of loss, it cannot be used in conjunction with ring resonators, as the filter functions and Qs are hampered by additional loss.

Stress-optic phase modulators have been demonstrated on the Si_3N_4 platform [1]. These modulators are highly energy efficient and operate on the MHz timescale with little to no impact on waveguide propagation. However, because of the relatively weak stress-optic effect, these modulators require 8-10mm lengths to be able to reach Pi phase shifts, compared to 1mm lengths for resistive heaters. This requirement makes them ineffective in most resonators. The tuning capacity has been successfully enhanced by undercutting the waveguide structure and creating a suspended ring, as in [2]. However, these structures greatly reduce the performance of the resonators compared to unsuspended versions.

The first demonstration of an efficient, fast, and low-loss waveguide phase tuner will enable many future devices. Such a phase tuner, combined with an erbium-doped active layer [3], will allow fully integrated modulated lasers.

8.1.2 Asymmetric Multi-Layer Device Demonstration

The multi-layer techniques developed within this dissertation allow for waveguide layers with varying properties to be combined to realize more complex integrated structures. In the multi-layer spiral demonstrated, different waveguide properties were used as a tool to optically isolate each layer, without leveraging advantages from diverse waveguide properties. As future work, there should be a demonstration of a device that requires both strongly and weakly guiding waveguides vertically integrated on the same chip.

Such a device stands out as a combination of devices from this dissertation. The high-Q large mode volume resonator in Chapter 5, when operating as a laser, has a strong pump output

on both the reflected and through signals, alongside the laser output. To make full use of the laser output, the pump needs to be filtered with a high roll-off and high-extinction wavelength filter. The high-extinction resonator filter demonstrated in Chapter 4 has more than sufficient performance to achieve this filtering. The resonator filter would have to be adapted to the TE mode for this device. In such a device, the bottom layer could be the 40nm weakly guiding core, while the top layer is the stronger guiding 175nm core. This structuring would allow the 40nm core to take advantage of the thick, high-quality thermal oxide, while the 175nm core can be near the cladding/air interface for thermal heaters.

8.1.3 Low Bend Radius Structures

Compared to many waveguide platforms, the Si_3N_4 waveguides, particularly the weakly guiding thin core waveguides, have large bend radii. This feature makes complex routing and smaller footprint devices difficult to lay out. Many types of RF filters, for example, require significant delay lengths, requiring the Si_3N_4 low-loss waveguides, but suffer from bloated routing and switching layouts. There are a number of techniques that could be employed to greatly reduce the bend radius for certain parts of the photonic circuits. In this case, a small or even moderate loss penalty could be acceptable. Within the Blumenthal group, Michael Belt developed a deep SiO_2 trench etch. When a trench is etched on the outside of a Si_3N_4 waveguide, shown in Fig. 76, the bending radius can be greatly decreased. There is, of course, a trade-off with higher scattering loss at this newly etched interface.

Alternatively, one could use the multi-layer techniques presented in this dissertation to separate the routing and delay components into two separate layers. The routing layer could achieve a much tighter bend radius, while the delay layer could be optimized to attain the lower waveguide losses. In addition, having two layers allows for simple routing and layouts, as the

layers can cross over each other without interaction. There is a very small loss penalty associated with the layer transition, but there is a significant increase in cost and complexity from moving from a single layer to multiple layers.

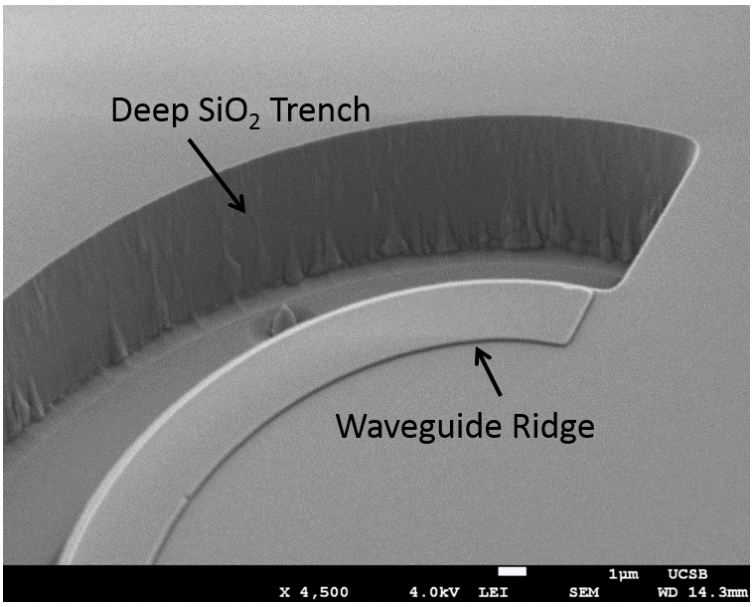

Fig. 76. Deep SiO_2 trench etched on the outside of a waveguide.

8.2 References

[1] Hosseini, N., Dekker, R., Hoekman, M., Dekkers, M., Bos, J., Leinse, A., & Heideman, R. (2015). "Stress-optic modulator in TriPleX platform using a piezoelectric lead zirconate titanate (PZT) thin film." *Optics express*, *23*(11), 14018-14026.

[2] W. Jin, R. G. Polcawich, P. Morton, and J. Bowers, "A piezoelectrically tuned suspended silicon nitride ring resonator via PZT thin film actuator, Optics Express, 26, p. 3124 (2018).

[3] Michael, and Daniel J. Blumenthal. "Erbium-doped waveguide DBR and DFB laser arrays integrated within an ultra-low-loss Si 3 N 4 platform." Optics express 22.9 (2014): 10655-10660.